Fall 2019

Quantification of Material Degradation for Material State Awareness of Composite Materials.

Vahid Tavaf

QUANTIFICATION OF MATERIAL DEGRADATION FOR MATERIAL STATE AWARENESS OF COMPOSITE MATERIALS

by

Vahid Tavaf

Bachelor of Science
Islamic Azad University of Ahvaz, 2007

Master of Science
Shahid Chamran University, 2011

Submitted in Partial Fulfillment of the Requirements

For the Degree of Doctor of Philosophy in

Mechanical Engineering

College of Engineering and Computing

University of South Carolina

2019

Accepted by:

Sourav Banerjee, Major Professor

Victor Giurgiutiu, Committee Member

Xiaomin Deng, Committee Member

Paul Ziehl, Committee Member

Cheryl L. Addy, Vice Provost and Dean of the Graduate School

DEDICATION

This thesis work is dedicated to my dear wife, Minoo, who has been a constant source of support and encouragement during the challenges of graduate school and life. I am truly thankful for having you in my life. This work is also dedicated to my child, Milan. You have made me stronger, better and more fulfilled than I could have ever imagined. I love you to the moon and back.

This work is also dedicated to my parents, Parvin and Mohammad, who have always loved me unconditionally and whose good examples have taught me to work hard for the things that I aspire to achieve.

I also dedicate this work to my beloved brother and sisters, Saeed, Neda, and Nastaran. They always gave me their love and support.

ACKNOWLEDGEMENTS

Firstly, I would like to express my sincere gratitude to my advisor Dr. Sourav Banerjee for the continuous support of my Ph.D study and related research, for his patience, motivation, and immense knowledge. His guidance helped me in all the time...

I would like to thank my committee member for their precise feedbacks.

At last but not least, I would like to thank my dear wife Minoo Atabi for her patience and support. I would like to thank my parents for their support as well.

ABSTRACT

The objectives of this research are to develop a comprehensive method to quantify the material degradation of composite materials in the presence of distributed damages and predict the failure in the defected composites using the updated effective material properties. Defects can grow in composites at the macro scale caused by the microscale voids, matrix cracks, fiber breakages starting from manufacturing processes to the high and low cycle fatigue loads, high temperature, and high humidity during operation. Hence, to predict a more realistic failure model, it is necessary to consider the repercussions of degraded materials. The proposed research work is divided into two major parts

Effect of distributed defects on effective material properties of the composites is required for the progressive failure models. Although the degradation of the effective material properties due to the presence of the lower scale damages is well investigated, how each material coefficients should be degraded in a progressive failure model is still a dilemma. The percentage of defects, the shape of the defects, and their stochastic distribution may affect the individual material coefficients in a unique way and may not be uniform across the constitutive matrix. Therefore, to find how the individual material coefficient in a constitutive matrix changes due to the presence of the voids and fiber breakage, all material coefficients in a constitutive matrix were studied. The representative volume element of a fiber-matrix composite was studied with appropriate boundary conditions and respective material coefficients were calculated. It was found that the local

gradients of the degradation curve obtained for each material coefficient are not linear with the increasing percentage of degradation and not uniform for all material coefficients. The different shapes and locations of the defects with constant percentage of defect were found to have an effect on the material coefficients.

The objective of this study was to investigate the effect of multiple hole orientations on the strength of composite materials and the interaction of crack paths as well. Generally, holes may be created in the composite structures due to the assembling or the joining of parts. A high stress gradient may occur at the vicinity of their edge as a result of holes. The stress gradient around a hole is not only dependent on material constants, but also fiber direction and hole orientations. This complex gradient stress may affect strength of structures and damage propagations. Hence, to fulfill the requirements, peridynamic method was employed to predict strain energy, crack paths, and tensile strength of the composite materials in the presence of multiple holes orientations with different fiber directions.

.

TABLE OF CONTENTS

LIST OF TABLES

LIST OF FIGURES

CHAPTER 1

INTRODUCTION

1.1 Problem statement

Composite materials have been extensively used in a wide range of industries such as aerospace [1-4], automotive [5-7], civil infrastructure [8-10], etc. For example, 50 percent of the Boeing 787 is made of composite materials [11]. Figure 1.1 shows the applications of composite materials. Composite structures may fail due to existing or created precursor damage.

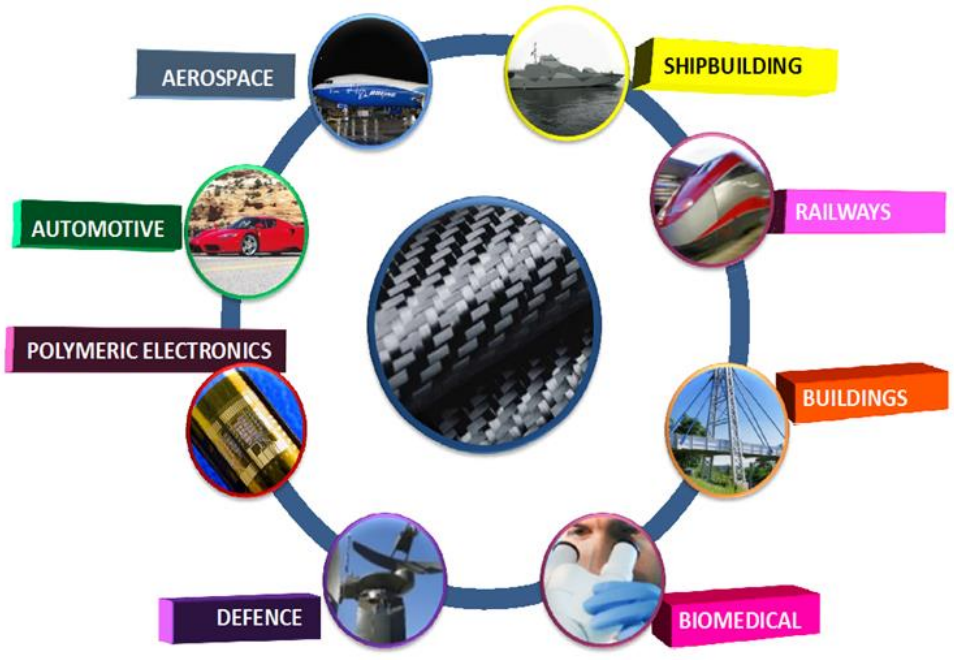

Figure 1.1: Application of composite materials [12]

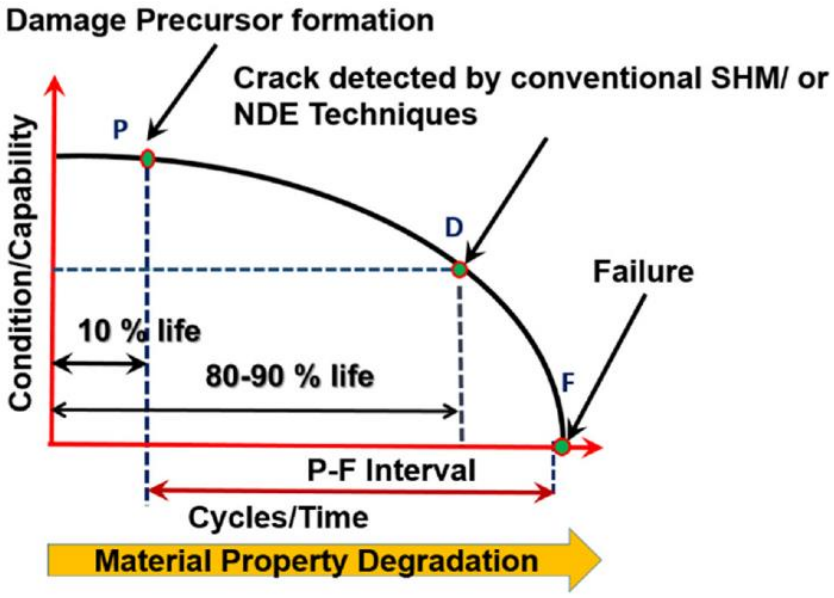

Figure 1.2: Material properties degradation cycle [13, 14]

Precursor damage is defined as the progression of structural material property degradation or morphology that can evolve into damage [15, 16]. This description implies that precursor damage in this context is some microstructural changes that happen "before" damage and can "develop" into damage [16]. As depicted in Figure 1.2, precursor damage occurs in composite materials at the very early stage. Precursor damage can be evolved to common damage modes in composite materials such as developing micro cracks in matrix, debonding between fiber and matrix, and delamination. The precursor damage may occur in the composite materials due to manufacturing defects, environmental effects, fatigue loading, etc.

Figure 1.3 shows the problem statement flowchart. The two precursor damages in composite materials that occur most frequently are voids in the matrix and fiber breakage. Fiber breakage might occur during the manufacturing process due to high impact loads and high fatigue load cycles. Voids might also be present due to manufacturing deficiency.

Voids and fiber breakage at the very early stage can cause significant degradation of the material properties. The degraded material properties should be included for the damage modeling, progressive failure analysis, and computational nondestructive evaluations (CNDE). However, the percentage of material degradation in composite materials in presence of void and fiber breakage is still a dilemma.

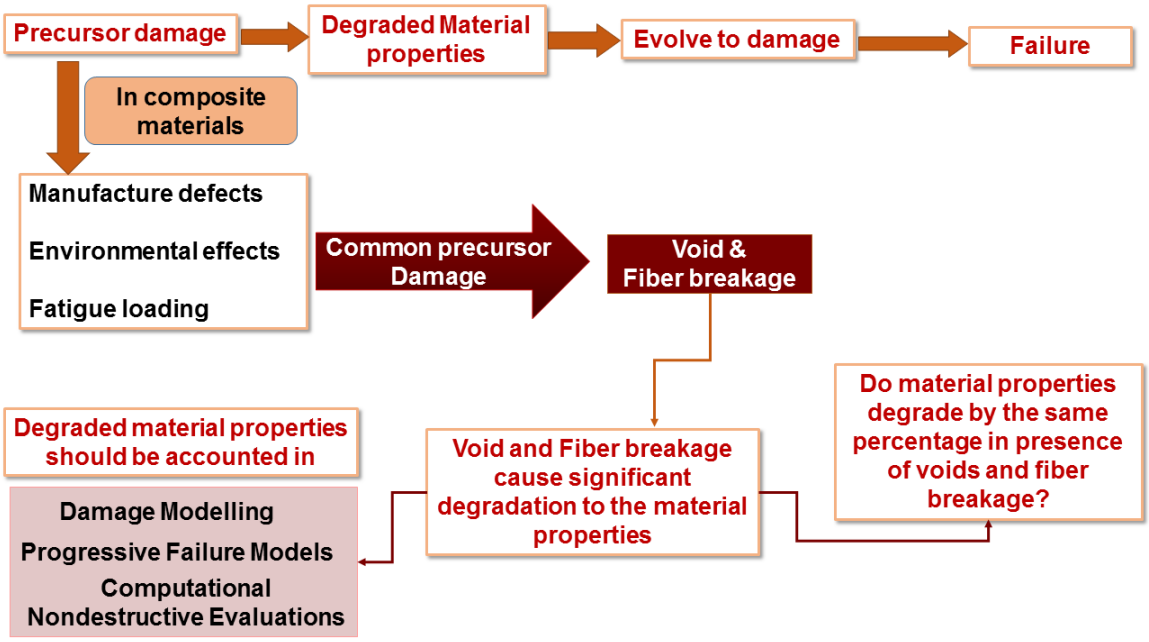

Figure 1.3: Schematic of problem statement

1.2 Motivations

The most recent method to predict the strength of composite structures with holes is progressive failure analysis.

Figure 1.4 shows the application of material degradation in progressive failure analysis. In this method, composite structures with holes are considered at pristine state. However, the composite structures do not remain pristine at the vicinity of the holes. Making holes in the composite structures may create micro-voids and fiber breakage around the holes.

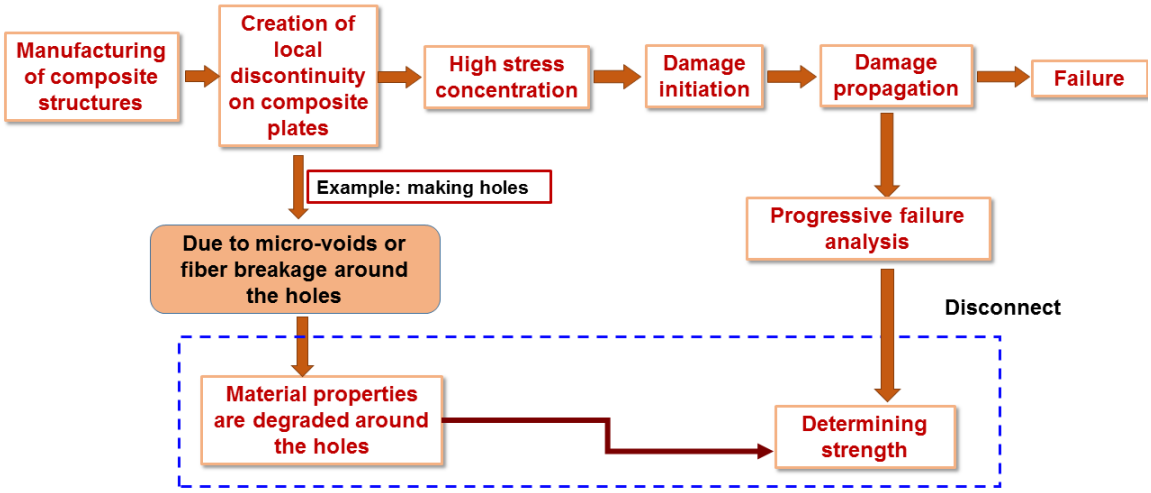

Figure 1.4: Application of material degradation in progressive failure analysis

Material properties of composite structures may degrade locally due to these defects. As the effective material property changes due to the defects, it is known that the strength of the defected composite will not be the same as a flawless composite. Hence, to accurately simulate the progressive failure of composite structures with holes, finding degraded material properties due to different defects is crucial. To predict the strength of composite structures with holes accurately, degraded material properties are needed and should be considered around the holes.

Moreover, degraded material properties are necessary for nondestructive evaluation (NDE). Figure 1.5 shows the application of material degradation in NDE and computational NDE (CNDE). The NDE can be carried out experimentally and numerically. To perform an NDE experiment for structures or materials, the pristine material properties are considered. Next, the NDE experiment is designed by knowing the dispersion behavior. Once NDE experiment was carried out, the NDE data will be generated. By analyzing NDE data, the damage geometry will be found. However, the material property of surrounding

damage area is not the same as at the vicinity of the damage. Thus, the degraded material properties are required to revise the finite element model. Furthermore, to design a CNDE experiment, the CAD model of structure should be modeled.

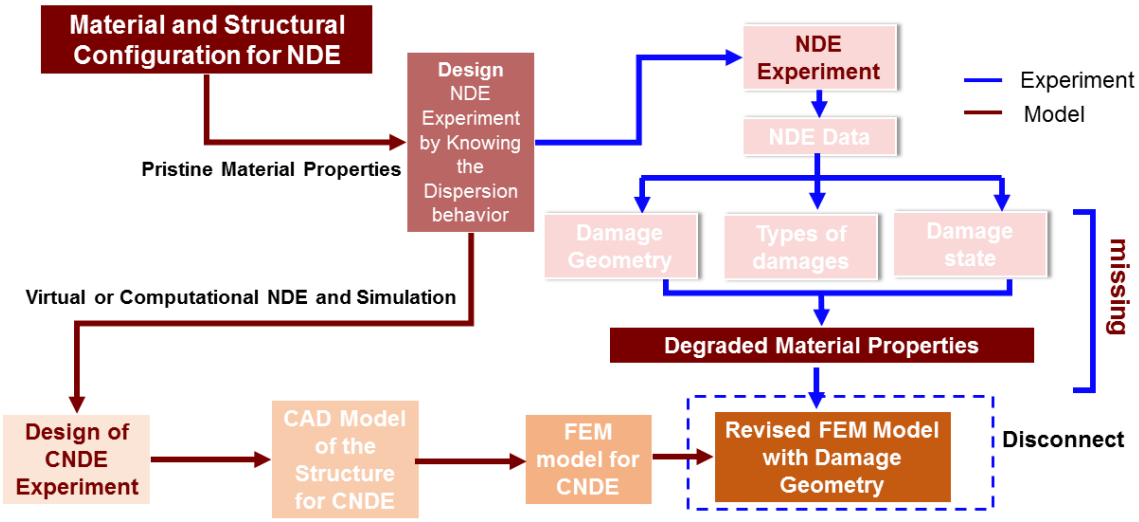

Figure 1.5: Application of material degradation in NDE and CNDE

The FEM model for CNDE can be generated based on a CAD model. Next, to obtain accurate results, we need to revise the FEM model to include damage geometry. To fulfil this requirement, the degraded material properties should be considered

1.3 Approach

To accurately quantify the degraded material properties of composite materials due to the precursor damage, a generalized representative volume element (RVE) model is proposed. This model calculates all necessary degraded constitutive coefficients and material engineering constants in the presence of the precursor damage. Voids and fiber breakage are two common precursor damages which are considered in this dissertation. The voids are modeled in the RVEs with different shapes, sizes, and locations. The voids

are randomly distributed into the RVEs. The degraded material properties are calculated using micromechanics, homogenization techniques, and implementation of periodic boundary conditions. The effects of different void parameters on the change of the effective material properties are studied. Furthermore, the RVEs with fiber breakage are modeled as well. Two different angles of fiber breakage are considered to understand the effect of fiber breakage angle on the effective material properties.

The degraded engineering constants in the presence of precursor damage are used to predict the strength of defected composite structures with holes precisely. One of the effective nonlocal methods which can simulate the progressive damage is the peridynamic method. The peridynamic method can accurately predict the strength of composite structures with one hole [17, 18]. However, the strength of composite structures with holes is not only dependent on material properties but also fiber direction and hole orientation [19]. To accurately calculate the strength of composite plates, in this research, peridynamic method is employed to study the effect of fiber directions, hole orientations, and degraded material properties on the strength of composite structures with holes. To conduct this study, unidirectional composite structures with three different fiber directions and 4 different hole orientations are considered. The strength of the unidirectional composite structures is determined with degraded engineering constants and pristine ones.

1.4 Outline

This dissertation is arranged in the following way. In Chapter 2, the literature review about the quantification of effective material properties in composite materials and the damage propagation in composite materials using the peridynamic method are addressed.

The quantification of effective material properties and engineering constants in the presence of precursor distributed damages, such as different void shapes and locations and fiber breakage, are discussed in Chapter 3. In Chapter 4, the peridynamic simulations are applied to predict damage propagations and determine the strength of different configurations of open hole composite plates with different fiber directions. Next, the effects of degraded material properties on the strength of open hole composite plates are studied using the updated engineering constants. Summary and conclusions are also discussed in Chapter 5. In Chapter 6, guided waves in corrugated structures are studied. In this chapter, generalized dispersion equations for Rayleigh-Lamb and shear horizontal waves are investigated for corrugated waveguides.

CHAPTER 2

LITERATURE REVIEW

2.1 Quantification of effective material properties in composite materials

Due to their high strength and lower weight compared to metals, composite materials have been extensively utilized in various industries, specifically in aviation, aerospace, vehicle manufacturing, infrastructures projects, etc [20]. In addition, composite materials with piezoelectric fibers can be utilized in sensors actuators industry. They may be employed to harvest energy in smart structures such as metamaterials [21-25]. Composite materials are categorized based on their constitutive coefficients. Isotropic, orthotropic, monoclinic, and anisotropic are common categories of composite materials [26]. Quantifying the material properties of composite materials is a substantial component in various fields of science, such as wave field modeling, damage modeling, and vibration analysis [27-30].

Wave propagation analysis in composite materials has been a topic of interest in the field of solid mechanics for the last couple of decades [31-34]. Understanding the wave propagation behavior in composite materials has become important for computational NDE and Structural Health Monitoring (SHM) due to various uses of those materials. The most recent methods are Finite Element Method (FEM) [35-37], Boundary Element Method

(BEM) [38], Indirect Boundary Integral Equation (IBIE) [39], Multiple Multi-Pole Method (MMP) [40], Spectral Element Method (SEM) [41], Local Interaction Simulation Approach (LISA) [42], Distributed Point Source Method (DPSM) [43], and Gaussian Distributed Point Source Method (G-DPSM) [44]. Determining material properties of composite materials becomes more challenging once precursor damages are created.

Precursor damages and internal flaws in composite materials, at the very early stage, cause material degradation under service load. Degraded material property is not comprehensively considered in the progressive failure models as well. Degradation of material properties at the macroscale is initiated due to microscale damages like matrix cracks, voids, and fiber breakage. These damages may present in the pristine material due to manufacturing processes. They may also initiate during operation due to high temperature, thermal fatigue, high humidity, high or low fatigue load cycles, etc.

Two precursor damages that may occur frequently in the composites are matrix voids and fiber breakage. These are considered in this dissertation. Fiber breakage during operation might occur due to high fatigue load cycles and/or high impact. Voids might also be present due to manufacturing deficiencies. When the effective material property changes due to the defects, it is expected that the behavior of the defected composite during the progressive failure will not be the same as a pristine composite. Thus, to accurately simulate the progressive failure behavior of the defected or fatigued composites, it is crucial to quantify the individual effective material property in the matrix of constitute coefficients.

For the last two decades, researchers have calculated the effective material properties of the composite materials with different methods [25]. Suquet [45], Bakhvalov and Panasenko [46] presented an analytical method to obtain the effective material properties using representative volume element (RVE) and homogenization technique for handling the different load cases. Sun and Vaidya [47] proposed an RVE with two different configurations of fiber, a square and hexagonal array, to assess the constitutive coefficients. They applied symmetric and periodic boundary conditions to calculate the effective material properties. Michel et al. [48] presented two methods based on finite element method and Fast Fourier Transform (FFT) which used linear or nonlinear constituents. FFT method did not converge when the model encountered a discontinuity. Li et al. [49] developed a unit cell using square and hexagonally configurations and derived symmetric boundary conditions for the unit cells. They also showed that irregular fibers and fiber imperfection can be accommodated in a unit cell.

Lenglet et al. [50] Berger et al. [51-56], Moreno and et al. [57-59] and Qin et al. [60] conducted a comprehensive study and obtained a full matrix with individual material coefficients of effective material properties for piezoelectric reinforced composite using an RVE with the single fiber. They used a three-dimensional model with hexagonal and square fiber configurations and applied periodic boundary conditions. The constitutive coefficients were calculated for different fiber volume fractions and were compared to asymptotic homogenization methods (AHM). Recently, researchers have studied

a) effective material properties of RVEs with 2 layers and simulating matrix interfacial decohesion,
b) new algorithm to generate general RVE with random distributed fibers or particles

c) Obtaining material properties of 3D woven composite [61-66].

Swaminathan et al. [67] studied two-dimensional RVE models with nonuniform dispersion of inclusions for a unidirectional composite to calculate the effective material properties. They found that the number of fibers should be 50 if the fiber volume fraction at the pristine state ranges between 31%-33%.

Researchers have conducted extensive studies on the fatigue life, strength, and material properties of different materials in presence of the voids and the fiber breakage. Lambert et al. [68] considered a large individual void in a laminated matrix. They reported that the void had a significant effect on fatigue life. Furthermore, when they investigated the local ply-level, they found that the compromised fatigue life was caused by the crack propagation at the laminate interfaces.

Studies were also conducted to understand the effect of micro-voids on effective material properties [69-71]. De Almeida et al. [72] introduced an experimental method to show the effect of void content on the static strength and fatigue life of the composite laminates subjected to flexural loading. The results showed that the fatigue life of the composite is compromised by the presence of voids. Lee et al. [73] presented a model which can predict the effect of fiber breakage on the creep and on the rupture life of a metal composite. They investigated the longitudinal creep behavior of the SCS-6/Ti composite as well. Anlas et al. [74] developed a 2D model to predict the effect of fiber fracture which is randomly distributed and found the effective elastic modulus of a short-fiber/aluminum matrix composite. Kumar et al. [75] characterized the degradation of an IM7/997 carbon fiber-reinforced epoxy which was under ultraviolet radiation and/or condensation. The

transverse tensile strength of the matrix was decreased by 29% after 1000 hours of cyclic exposure to UV radiation and condensation.

Swaminathan et al. [76] proposed a suitable size of RVEs for unidirectional composites undergoing the initiation and propagation of damage in the form of interfacial debonding. They found that the size of the RVE with 32% fiber volume fraction was 63 μm. Li el al. [77] investigated the effective material properties using 2-D square RVE with 17%, 29% and 39% of porosity. Srinivasulu et al. [78] generated an algorithm to simulate a high fiber volume fraction in a discontinuous fiber-reinforced composite with randomly oriented fibers. They investigated the effect of void content on the modulus of elasticity and Poisson's ratio using finite element method and micromechanics modeling.

Dong [79] introduced a two-dimensional model of RVEs to understand the effect of void content on the tensile strength and transverse modulus. In some cases, the transverse modulus was decreased due to the void content. But, the tensile strength of the laminate was increased. However, in 2D models, only the transverse elastic modulus and one Poisson's ratio could be obtained. Material properties along the fiber direction, two shear coefficients, and another Poisson's ratio could not be found. Some works have been conducted to study the effect of fiber breakage in metal composites [73, 74]. Evaluating the effect of fiber breakage on fiber reinforced composites is necessary due to their heavy demands in many industrial, space and military applications.

Although research has been quite comprehensive in all the above cases, only a few constitutive coefficients were calculated [51-60]. Therefore, it is necessary to find all the effective material coefficients in the effective material property matrix to understand the

effect of microscale damage on progressive failure models, to perform the CNDE, and to predict wave signals due to degraded material properties. In current practice, it is not appropriate to express the degradation of material properties of anisotropic materials using the degradation of elastic moduli and Poisson's ratio only by a fixed percentage because each coefficient in the constitutive matrix degrades uniquely and may not be captured correctly by degrading just the elastic moduli and the Poisson's ratio.

Hence, this work is presented to obtain a complete constitutive matrix with all the material coefficients in the presence of defects like voids with the different shapes, distribution, and fiber breakage in composite materials using multi-fibers and multilayer RVEs.

2.2 Progressive failure analysis

One of the most common methods to manufacture or assemble composite structures is to fasten two composite structural parts [80]. Fastening composite structures can be performed by pin joints, bolt-filled holes, thread joints, clamped joints, etc [81]. Similarly, joining the composite structures with riveted joint or bolted joints is carried out if the composite structures need to be disassembled or inspected. In fastening the composite structural parts to allow for damage inspection, or installation of electric device, or piping installation, it is always necessary to make holes on the composite structures [82, 83].

Making a hole in the composite structures creates a high-stress concentration zone at the vicinity of the hole's edge [84, 85]. Consequently, it reduces the strength of composite structures. In addition, damage will nucleate due to high-stress concentration around the holes. The damage starts propagating due to the fiber breakage, matrix cracking, fiber-

matrix splitting, and shear-out failure when the composite structures are subjected to loads [86, 87]. The ultimate strength and the final failure of isotropic materials are only dependent on material properties. However, damage nucleation, damage propagation, and strength of composite structures with multiple holes are not only dependent on material properties but also fiber orientation, hole locations, hole orientations, etc [88, 89]. Thus, progressive failure analysis of open-hole composite has been a topic of interest for decades.

The researchers have attempted to predict the final failure and strength of open-hole composite structures with stress concentrations for decades. The point/average stress model is one of the primary methods for obtaining strength of an anisotropic plate [90]. In this method, failure is predicted to occur once the stress at a certain distance or average stress over a certain distance from the notch tip reaches the strength of the plate without a notch. Another method uses by linear elastic fracture mechanics. In this method, failure is predicted to occur if the notch which is introduced by an equivalent crack attains the critical size [91]. These methods are able to predict the strength of composite structures reasonably. However, to determine the parameters in the models, extensive experiments need to be carried out.

Progressive damage may cause stress redistribution [92]. To consider stress redistribution, progressive failure analysis of composite structures has been introduced to predict the strength of composite structures with a hole. The material degradation method (MDM) and continuum damage mechanics (CDM) approach are used to model in-plane damage modes such as fiber failure and matrix cracking [93]. Hufner and Accorsi [94] applied the progressive failure approach to woven composites with one hole. The results were validated by a digital image correlation (DIC) method. They employed the stiffness

reduction technique after failure. This approach was implemented in the ABAQUS software using a user material subroutine. CDM and in particular MDM suffered from a lack of a strong physical basis to quantify the percentage of material degradation accurately. Researchers have used the discrete ply model approach to predict the final failure of open-hole composite materials [95-97]. However, this method is computationally intensive.

Cohesive zone model (CZM) is another method that can be used for the progressive damage model. Ridha et al. [98] modeled the progressive failure in notched composite laminates with different stacking sequences. The maximum stress and Tsai-Wu failure criterion were used to model in-plane damages. The CZM was employed to model the interfacial behavior. The CZM used to employ for composite failure analysis using standard finite element method and fall into two categories: the continuum model [99] and cohesive interface element [100, 101]. The continuum model is independent of mesh generation. However, this is not suitable for the propagation of dominant crack. The cohesive interface element can model matrix crack and delamination interface. But, cohesive elements should be aligned with the finite element which may cause difficulty in meshing for complex geometry.

To overcome this limitation in the standard finite element method, extended finite element method (XFEM) was introduced [102, 103]. Higuchi et al [104] predicted the progressive failure damage and resultant failure of carbon fiber plastic laminates using a proposed mesoscale simulation methodology. The evolution of delamination and matrix cracking was conducted through the CZM. The CZM for analyzing the delamination growth was performed using interface element and XFEM was employed for modeling

matrix cracking. To overcome the limitation of continuum damage model features, Dongen et al. [105] introduced a method for progressive damage analysis of composite structures with one open-hole. The proposed methodology combined the continuum damage model and the cohesive zone model. Matrix crack and delamination criteria are used to simulate progressive damage using XFEM in ABAQUS software. However, using XFEM in ABAQUS software has some limitations including capturing one crack per side, per ply.

2.3 Peridynmic method

In the discussed method, partial differential equations (PDEs) are used to define damage in continuous body. It is hard to capture damage propagation using these methods due to the intrinsic limitation. The limitation is that the spatial derivatives are not defined at the crack tips by the definition. Thus, these methods have similar trouble once the crack nucleates in a body which are already discussed. To overcome the limitation, a nonlocal theory is introduced by Silling [106] such that the spatial derivatives are not required for defining the fracture. This method is called bond-based peridynamic (PD) theory.

Silling et al. [107] generalized bond-based PD theory by considering the interaction of the number of material points located in a certain distance from each other. In comparison to classical continuum mechanics, Silling employed the integral form of the equations of motion to introduce PD theory. By using the integral form of the equations of motion, crack initiation and propagation are captured at multiple sites without resorting to special crack-growth criteria.

Researchers have employed PD theory on a different problem for isotropic materials successfully. Warren [108] implemented the PD method to predict the fracture

of the notched and un-notched bar under a velocity gradient. Also, Agwai [109] studied the crack propagation in isotropic plates with edge crack and a plate with cylindrical glass inclusion with initial crack. The obtained results showed that the PD results and experimental results had good agreement compared to each other.

Researchers have used PD method to analyze impact damage and delamination growth in composite materials. Damage may occur in a composite panel due to low-velocity impact. Xu et al. [110] analyzed impact damage in composite materials. They predicted the delamination and matrix damage process in the composite thoroughly. Sun and Huang [111] analyzed the influences of impacting velocity on the damage pattern and the damaged area of the composite laminate. The results revealed that impacting damage in composite laminate was caused by the stretching strain. When the impacting velocity was increasing gradually, the damage firstly occurred at the fixed edges, subsequently on the bottom surface and finally on the top surface of the composite laminate. Hu et al. [112] defined new criteria for interlayer bond stretch using critical energy release rate values.

Roy et al. [113] advanced a PD damage model to study delamination of composite structures. Using critical energy rating, they modeled interfacial cohesive damage by degradation function. They were be able to successfully predict the failure of composite structures. Kilic [114] employed the PD theory to predict the damage of the center-cracked composite laminates with different fiber orientations, and the results agreed with the experimental observations in the literature.

Researchers have conducted crack propagation on a unidirectional lamina with a center notch and the laminated composite with large-notch under the tensile load have been

conducted [115, 116]. Tastan et al [117] studied the crack propagation in the thin orthotropic flat plates under the bending loads. They reported that the results are consistent with those obtained with classical computational methods. In addition, they modeled the crack patterns in the orthotropic plates accurately.

Yu and Wang studied the progressive damage in the laminated composite plate with a notch and open hole. [118]. In this study, the damage propagation and failure modes were found under a tensile load. Colavito et al. [119] analyzed the residual strength of composite laminates with a hole. The results showed that the PD results are in a good agreement with experimental results. Hu and Madenci introduced a new bond-based PD modeling for composite laminates [120]. The proposed method did not have any restrictions on fiber orientation and material properties. Later, Hu and Madenci studied damage initiation and growth in a laminated composite with one hole [121]. The results were validated with the Air Force Research Laboratory (AFRL) for 3 different layups under fatigue loading for strength and failure progression.

According to the established literature, there are several methods to predict the strength of composite structures with an open-hole such as material degradation method [93, 94], cohesive zone model [99], extended finite element method [102-105], and experimental study [122-124]. Nevertheless, these methods have their own shortcoming which were already discussed. To avoid the inherent limitation of the approaches, researchers have used PD method to analyze the progressive damage and predict the strength of composite structures with an open-hole [118-121]. However, in some composite structures which are used in aircraft, multiple holes may exist. Thus, it is required to study the effect of multiple

holes and their configurations on the strength of composite structures which have not been considered in the literature.

In this study, the PD method is employed to simulate the damage propagations in unidirectional composite plates with multiple holes under rate of change of displacement. The different hole orientations and fiber direction are considered to understand how damage propagates in the composite plates. For further study, the strength of the unidirectional composite plates with multiple holes and different orientations are studied. Making holes in composite plates may cause material degradation around the holes. Therefore, the effect of degraded material properties around the holes on the strength of unidirectional composite are investigated.

CHAPTER 3

QUANTIFY EFFECTIVE MATERIAL PROPERTIES IN PRESENCE OF DISTRIBUTED DAMAGES

3.1 Material Scanning and Observations

In this study, the elastic properties of a unidirectional carbon/carbon composite material which are assumed to be a transversely isotropic [125] were measured using universal mechanical test system (MTS). The material properties of the unidirectional carbon/carbon composite are listed in Table 3.1.

Table 3.1: Material properties of fiber and matrix

T 300 Carbon fiber				Epoxy	
E_{fl} (GPa)	E_{fv} (GPa)	ν_{fl}	ν_{fv}	E (GPa)	ν
230	15	0.25	0.07	5	0.16

In the experimental design, 10 composite samples were planned for the tensile test and 10 samples were planned for the compression test. Mean values are reported to represent the equivalent elastic modulus. The specimens are prepared for the tests based on ASTM C1275-95, ASTM C1359-96 and ISO/DIS 15490 which are 4mm (thickness)×75mm (length)×8mm (width). Before running any of the mechanical tests, the porosities of all samples were calculated using an image processing tool that analyzes the composite images from scanning acoustic microscope (SAM) [126]. All SAM images were taken at room

temperature and utilizing a 100 MHz acoustic transducer with lower and higher frequency range of ~25 MHz to ~500 MHz, with a peak near ~100 MHz. Similar samples were also imaged using Kyene Optical microscope. Images obtained from SAM and the optical microscope. Figure 3.1 illustrates the void content in the unidirectional composite. Here, void shapes are not fully spherical. Therefore, the void shapes in forms of spherical or ellipsoid were assumed to be used in the numerical models. All the specimens were scanned, and the void sizes and fiber breakage distances were measured using the image processing tool. The observations showed that the diameters of voids are in the range of 1.3 µm to 2.8 µm and the fiber breakage length is ~5 µm in average. After running all the compression and tensile tests for all 20 samples, the young's modulus of the composite material is reported as 98Gpa and 107Gpa, respectively under compression and tensile tests.

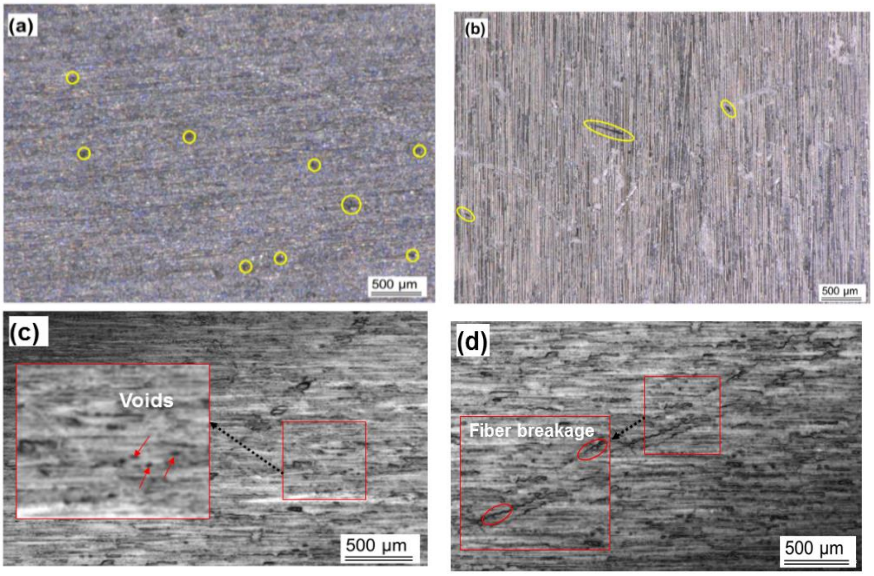

Figure 3.1: a) & c) Void identification from optical microscope and SAM, respectively; b) & d) Fiber breakage identification in composite specimens using optical microscope and SAM, respectively.

3.2 Modeling and simulations

RVE is the smallest component of a microscopic composites which can represent an element containing their microscopic constituent [52]. Figure 3.2 shows the periodicity of the composite and RVE configuration.

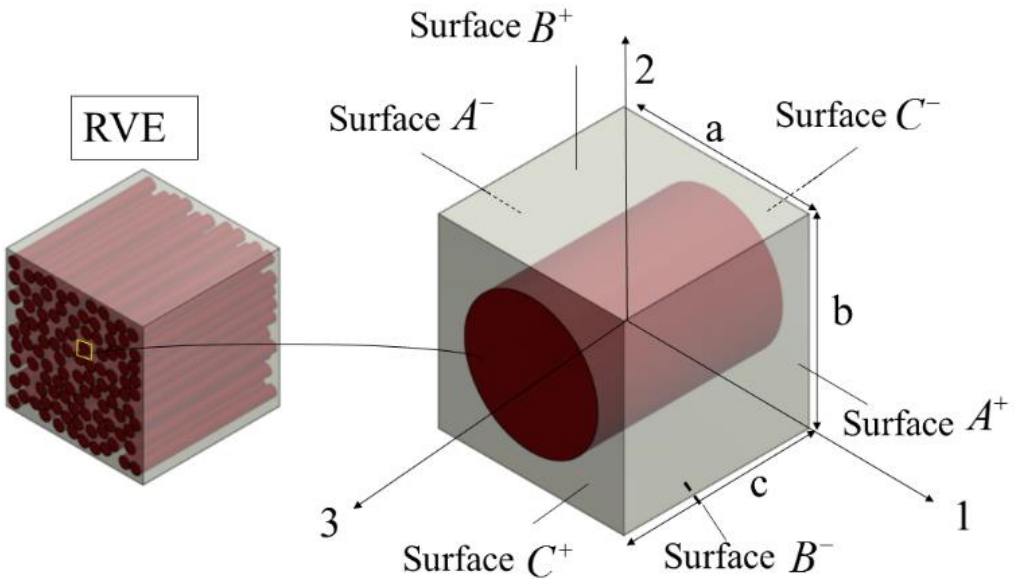

Figure 3.2: Periodicity of composite material and RVE configuration

Since the unidirectional composite can be considered as a periodical structure, periodic boundary conditions must be applied to the RVE to find the effective material properties using the RVE concept. In other words, RVEs which are located next to each other have the same mode deformation and they do not have any separation or overlap between each other. The periodic boundary conditions are shown in Eq. (3-1)[52].

$$u_i = \bar{S}_{ij}\, x_j + v_i \quad i, j = 1,2,3 \tag{3-1}$$

Where $\bar{S}_{ij}$ are average strains, v_i is the periodic part of displacement on the boundary conditions which is unknown, and they are related to the global load. To specify the periodic boundary conditions for the RVE which is depicted in Figure 3.2, Eq. (3-1) must be written for two opposite surfaces.

$$u_i^{K+} = \bar{S}_{ij}\, x_j^{K+} + v_i^{K+} \tag{3-2}$$

$$u_i^{K-} = \bar{S}_{ij}\, x_j^{K-} + v_i^{K-} \tag{3-3}$$

Where K^+ and K^- are A^+, B^+, C^+ and A^-, B^-, C^+ as they were demonstrated in Figure 3.2. The periodic terms v_i^{K+} and v_i^{K-} are identical at the opposite surfaces because of the periodicity. If Eq. (3-2) is subtracted from Eq. (3-3) macroscopic strain conditions can be expressed as follows:

$$u_i^{K+} - u_i^{K-} = \bar{S}_{ij}\left(x_j^{K+} - x_j^{K-}\right) \tag{3-4}$$

After implementing the periodic boundary conditions, the average strains and the average stresses and effective material properties are calculated. The average strain and average stress can be evaluated by [52].

$$\bar{\varepsilon}_{ij} = \frac{1}{V}\int_V \varepsilon_{ij}\, dV \tag{3-5}$$

$$\bar{T}_{ij} = \frac{1}{V}\int_V T_{ij}\, dV \tag{3-6}$$

Where V is the volume of the periodic RVE. It is substantial to emphasize that $\bar{S}_{ij}$ in Eq. (3-4) is an arbitrary value. $\bar{S}_{ij}$ is considered as 1 in this article.

3.2.1 Implementation of periodic boundary conditions

The periodic boundary conditions are applied based on the concept presented in the earlier literatures [53, 54, 56]. The finite element meshes need to be identical on the opposite surfaces to apply the periodic boundary conditions [51-54, 56]. Figure 3.3 shows the process of identical mesh generation over the unit cell surfaces. To fulfill this requirement, pre-mesh is generated on the master surfaces of the unit cell using dummy 2D linear elements. Next the meshes are copied over to the opposite surfaces. The mesh generation is performed using ANSYS built-in free surface mesh. The meshing of the matrix and the fibers are performed based on the surface meshes with tetrahedral linear

elements. The dummy 2D linear elements are deleted after the meshing was performed over the volume.

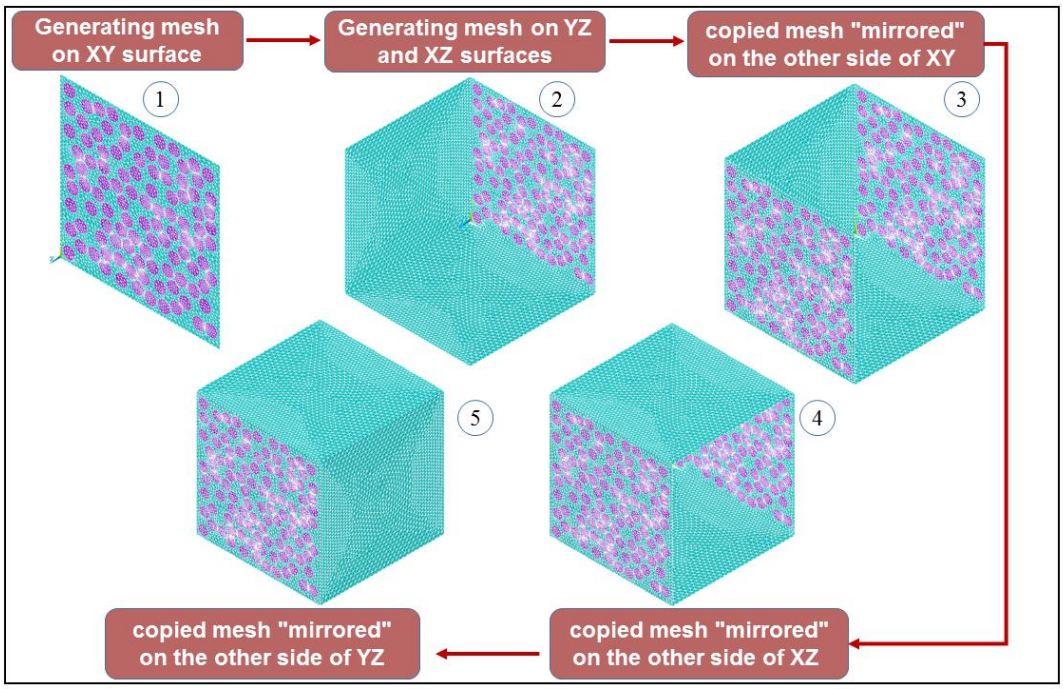

Figure 3.3: process of identical mesh generation on unit cell

To avoid over constrain conditions, periodic boundary conditions should be assigned to each pair of nodes only once. To satisfy this requirement, all pair of nodes are designated as the masters and the slave nodes at the corners. The master and slave lines were defined without the corner nodes, and the master and the slave surfaces were defined without the corner nodes and the lines. The categorization process was performed using a MATLAB code. Figure 3.4 depicts the category of contributed pair of nodes with periodic boundary conditions at the corners, on the opposite lines, and over the opposite surfaces. The master and slave nodes at the corners, on the lines, and over the surfaces are in blue and red color, respectively.

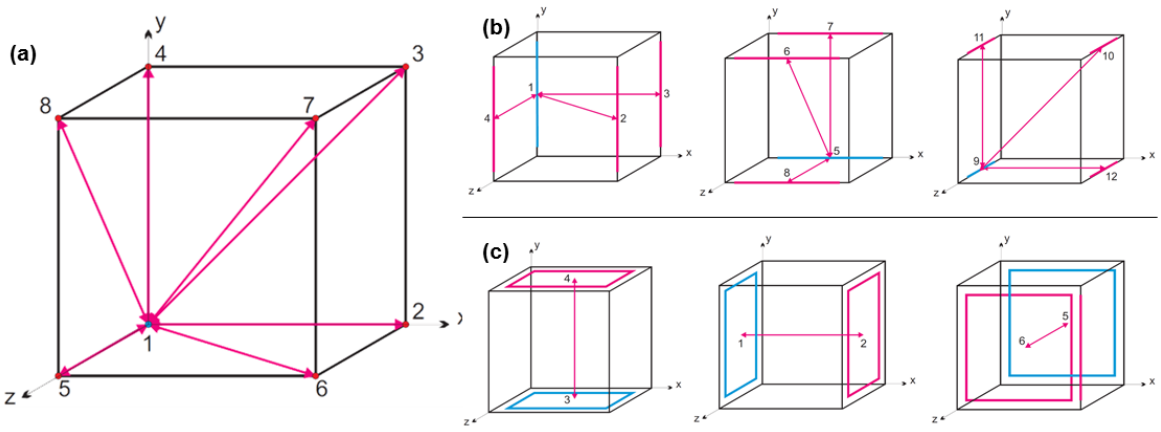

Figure 3.4: categorized nodes, lines, and surface selection for applying periodic boundary conditions

Required periodic boundary conditions are listed in Table 3.2 to calculate each constitutive coefficient [52]. To avoid the rigid body motion, u_x, u_y and u_z are imposed to be zero where x, y, and z are minimum. Figure 3.5 presents a detail depiction of loading conditions to visualize how periodic boundary conditions are applied.

Table 3.2: Implementing periodic boundary conditions for 3D RVE

Constitutive Coefficients	Surfaces X_{max}/ X_{min}			Surfaces Y_{max}/ Y_{min}			Surfaces Z_{max}/ Z_{min}		
C_{11}, C_{21}, C_{31}	$\Delta u_x=a$	$\Delta u_y=0$	$\Delta u_z=0$	$\Delta u_x=0$	$\Delta u_y=0$	$\Delta u_z=0$	$\Delta u_x=0$	$\Delta u_y=0$	$\Delta u_z=0$
C_{12}, C_{22}, C_{32}	$\Delta u_x=0$	$\Delta u_y=0$	$\Delta u_z=0$	$\Delta u_x=0$	$\Delta u_y=b$	$\Delta u_z=0$	$\Delta u_x=0$	$\Delta u_y=0$	$\Delta u_z=0$
C_{13}, C_{23}, C_{33}	$\Delta u_x=0$	$\Delta u_y=0$	$\Delta u_z=0$	$\Delta u_x=0$	$\Delta u_y=0$	$\Delta u_z=0$	$\Delta u_x=0$	$\Delta u_y=0$	$\Delta u_z=c$
C_{44}	$\Delta u_x=0$	$\Delta u_y=0$	$\Delta u_z=0$	$\Delta u_x=0$	$\Delta u_y=0$	$\Delta u_z=0$	$\Delta u_x=0$	$\Delta u_y=c$	$\Delta u_z=0$
C_{55}	$\Delta u_x=0$	$\Delta u_y=0$	$\Delta u_z=0$	$\Delta u_x=0$	$\Delta u_y=0$	$\Delta u_z=0$	$\Delta u_x=c$	$\Delta u_y=0$	$\Delta u_z=0$
C_{66}	$\Delta u_x=0$	$\Delta u_y=0$	$\Delta u_z=0$	$\Delta u_x=b$	$\Delta u_y=0$	$\Delta u_z=0$	$\Delta u_x=0$	$\Delta u_y=0$	$\Delta u_z=0$

The periodic boundary conditions are generated using MATLAB code in form of ANSYS interface language for desired constitutive coefficients.

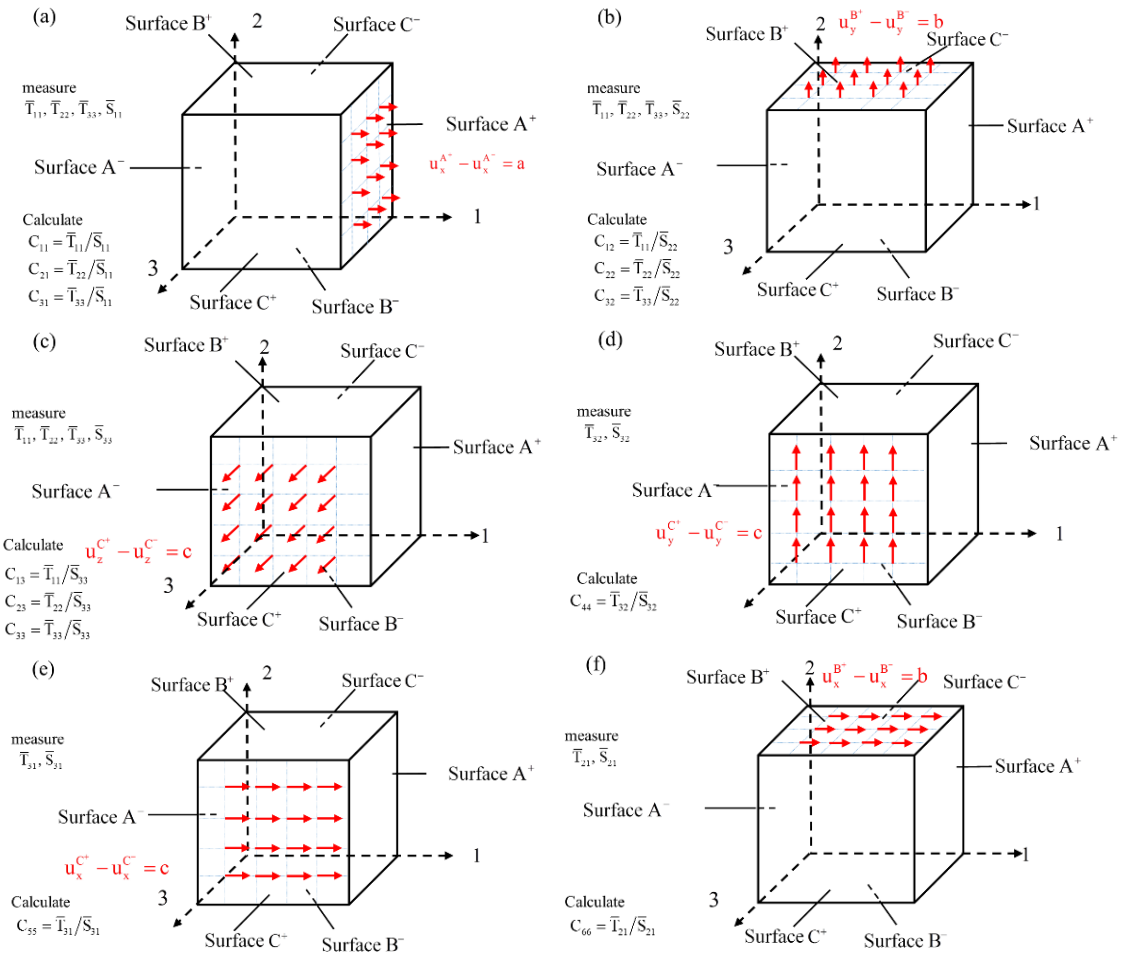

Figure 3.5: Schematic view for applying periodic boundary conditions to calculate a) C_{11}, C_{21}, C_{31} b) C_{12}, C_{22}, C_{32} c) C_{13}, C_{23}, C_{33} d) C_{44} e) C_{55} f) C_{66}

For further details, equations of the periodic boundary condition for calculating C_{11}, C_{21}, and C_{31} are depicted in Figure 3.6. As shown in this figure, the periodic boundary conditions are applied to corner points, lines without corner points, and the surfaces without lines. But, the external load are only applied on specific points (2, 3, 6, 7), lines (2, 3), and surface (2). Furthermore, the difference of displacements along x direction are only nonzero for mentioned nodes, lines, and surfaces. In other words, the nonzero conditions are only applied on the specific nodes, lines, and surfaces to calculate the desired effective material properties.

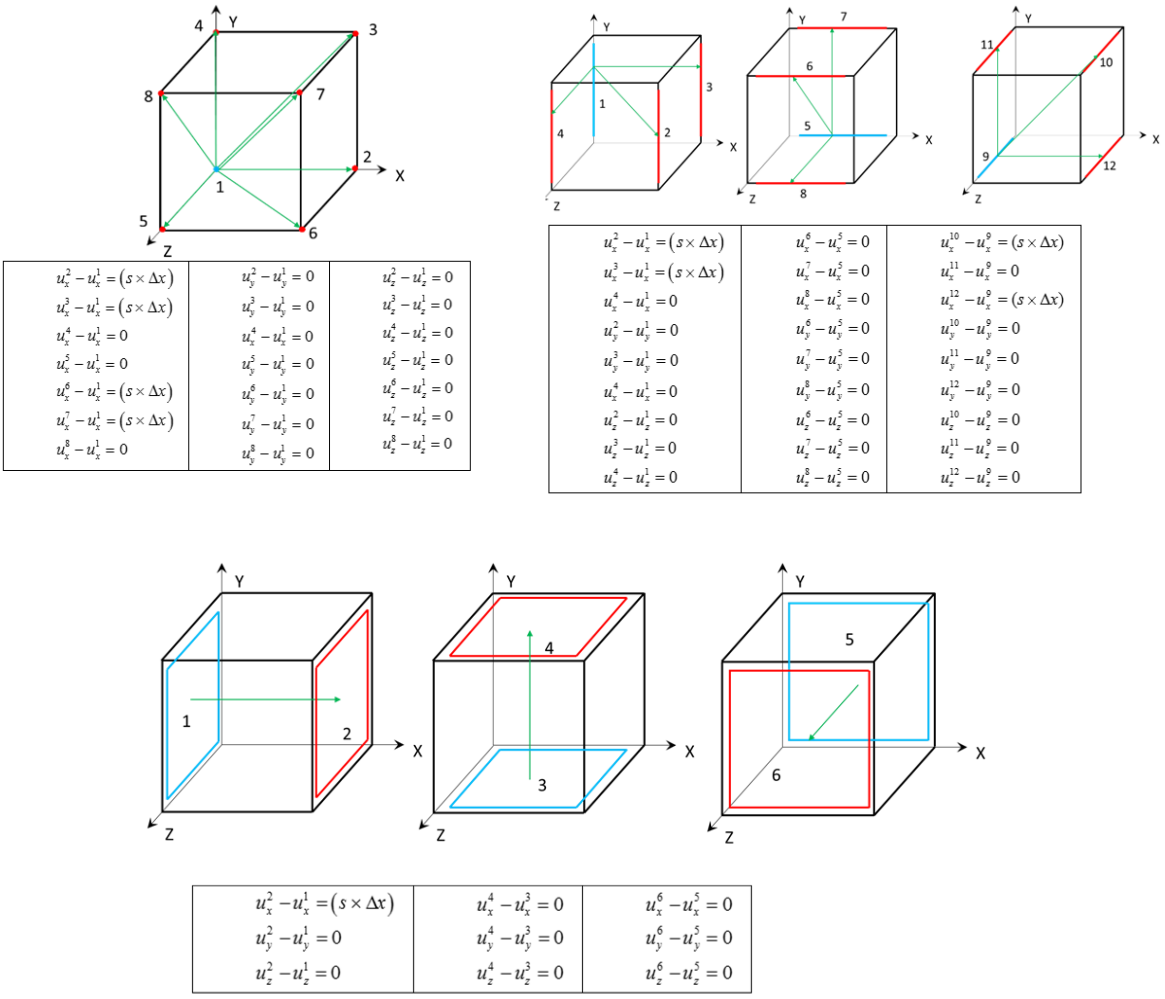

$u_x^2-u_x^1=(s\times\Delta x)$	$u_y^2-u_y^1=0$	$u_z^2-u_z^1=0$
$u_x^3-u_x^1=(s\times\Delta x)$	$u_y^3-u_y^1=0$	$u_z^3-u_z^1=0$
$u_x^4-u_x^1=0$	$u_x^4-u_x^1=0$	$u_z^4-u_z^1=0$
$u_x^5-u_x^1=0$	$u_y^5-u_y^1=0$	$u_z^5-u_z^1=0$
$u_x^6-u_x^1=(s\times\Delta x)$	$u_y^6-u_y^1=0$	$u_z^6-u_z^1=0$
$u_x^7-u_x^1=(s\times\Delta x)$	$u_y^7-u_y^1=0$	$u_z^7-u_z^1=0$
$u_x^8-u_x^1=0$	$u_y^8-u_y^1=0$	$u_z^8-u_z^1=0$

$u_x^2-u_x^1=(s\times\Delta x)$	$u_x^6-u_x^5=0$	$u_x^{10}-u_x^9=(s\times\Delta x)$
$u_x^3-u_x^1=(s\times\Delta x)$	$u_x^7-u_x^5=0$	$u_x^{11}-u_x^9=0$
$u_x^4-u_x^1=0$	$u_x^8-u_x^5=0$	$u_x^{12}-u_x^9=(s\times\Delta x)$
$u_y^2-u_y^1=0$	$u_y^6-u_y^5=0$	$u_y^{10}-u_y^9=0$
$u_y^3-u_y^1=0$	$u_y^7-u_y^5=0$	$u_y^{11}-u_y^9=0$
$u_x^4-u_x^1=0$	$u_y^8-u_y^5=0$	$u_y^{12}-u_y^9=0$
$u_z^2-u_z^1=0$	$u_z^6-u_z^5=0$	$u_z^{10}-u_z^9=0$
$u_z^3-u_z^1=0$	$u_z^7-u_z^5=0$	$u_z^{11}-u_z^9=0$
$u_z^4-u_z^1=0$	$u_z^8-u_z^5=0$	$u_z^{12}-u_z^9=0$

$u_x^2-u_x^1=(s\times\Delta x)$	$u_x^4-u_x^3=0$	$u_x^6-u_x^5=0$
$u_y^2-u_y^1=0$	$u_y^4-u_y^3=0$	$u_y^6-u_y^5=0$
$u_z^2-u_z^1=0$	$u_z^4-u_z^3=0$	$u_z^6-u_z^5=0$

Figure 3.6: periodic boundary equations for calculating C_{11}, C_{21}, and C_{31}

3.2.2 RVE size and calculating effective material properties

According to a previous work [67], the number of randomly oriented fibers that fulfill the 2D-RVE size requirements in the UD composite was calculated. In the present study, the same procedure is followed and the size of the RVE is determined. An RVE with length, width, and height of 62 µm is simulated to obtain the constitutive coefficients using the finite element method. The distributions of effective material properties at pristine state are investigated due to the different locations fibers. 15 different RVEs are modeled to

determine the distributions of the effective material properties. The fiber diameter is 7 μm and the fiber volume fraction is 50%. Interfaces between the fiber and matrix were assumed to be perfectly bonded [127]. The material properties of the fiber and the matrix are listed in Table 3.1. To analyze the problem using ANSYS, linear tetrahedral element type was selected. The periodic boundary conditions were applied to the RVE using Table 3.2 where a, b, c are 62 μm. To implement the periodic boundary conditions using ANSYS software based on Eq. (3-4), Table 3.2, Eq. (3-1) was employed. This investigation is in the range of linear elastic materials. To solve the problem, equations which is listed in Table 3.2 are rewritten in form of FEM for each desired constitutive coefficient as follows:

$$\begin{aligned} & u_i^{K+} - u_i^{K-} = \bar{S}_{ij}\left(x_j^{K+} - x_j^{K-}\right) \qquad i, j = 1,2,3 \quad K = A, B, C \\ & [K]^g \{u_i\} = \{F\} \end{aligned} \tag{3-7}$$

Where $\{F\}$ is equal to $\bar{S}_{ij}\left(x_j^{K+} - x_j^{K-}\right)$ and it can be a, b or c which is 62 μm for each case, $\{u_i\}$ displacement, and [K]^g the coefficient of displacement. To find the effective material properties after solving Eq. (3-7), the stresses and the strains were extracted from each element. Then using Eq. (3-5) and Eq. (3-6) average stress and the average strain were calculated. ANSYS interface is used to obtain integral stresses and strains for each constitutive coefficient.

3.2.3 Modeling Voids in the RVE

To understand the perturbation of effective material properties due to the voids [72, 78, 79], the RVEs were developed to simulate 1%, 2%, 3%, and 5% void content in the RVE. To determine the size of RVE with void contents, the procedure of established in [67, 76] are followed and the size of the RVE is calculated. The size of the RVE for the UD composite with void contents was 90 μm. Element types and material properties of the

fiber and the matrix are similar, discussed in the previous section. Figure 3.7 depicts the schematic diagram of the RVEs including spherical, ellipsoid, and combination of spherical and ellipsoid void contents. Bear in mind that ellipsoid void shapes are parallel to the fiber direction.

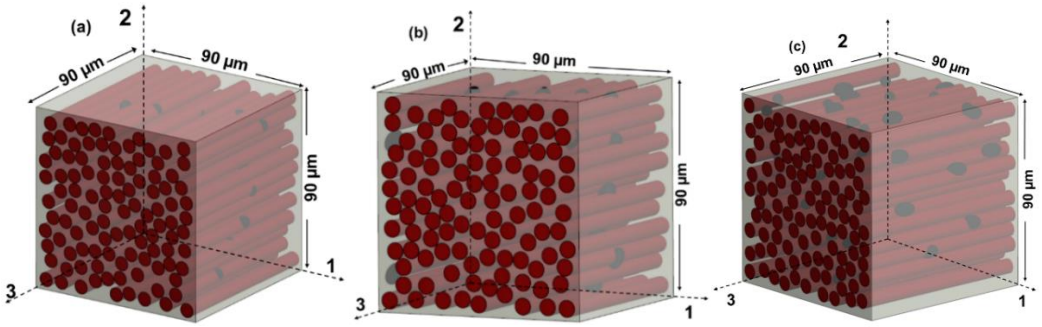

Figure 3.7: Schematic of an RVE including a) Spherical voids b) Ellipsoid voids c) Combination of spherical and ellipsoid voids

The voids are located in the RVE based on a specific algorithm. The center and radii of the spherical and ellipsoid voids are generated with random numbers generated from a normal distribution. Location and radius of the voids were constantly checked with the fiber locations and the voids are placed such a way that there is no contact/interfere between the fibers and the voids. This procedure was continued until the desired void content percentage is achieved. Figure 3.8 depicts the mesh generation on the RVE and its cross section. The void locations and void shapes may affect degraded material properties. In other words, the degradation amount of each effective material property may change due to the different void shapes and void locations. Therefore, a comprehensive study is carried out to quantify not only the range of degraded material properties but also their distributions. Figure 3.9 shows the design of simulations of RVEs with a fixed void percentage. As shown in this figure, the different void shapes with different locations are considered in the simulations

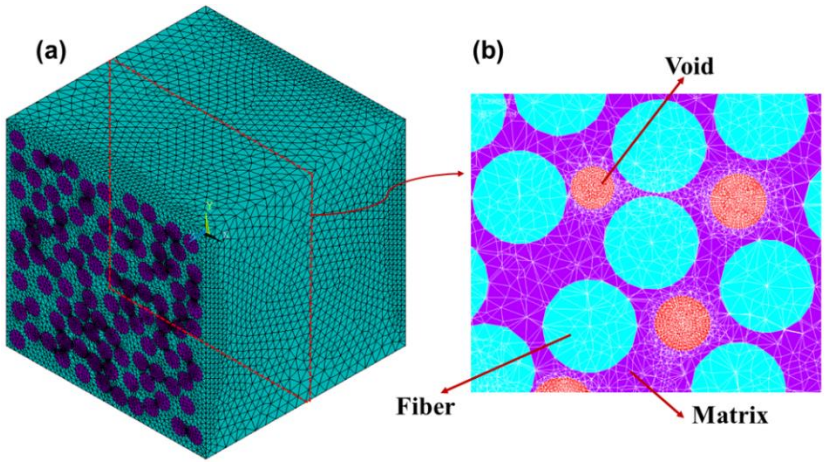

Figure 3.8: Mesh generation a) RVE b) Cross section of RVE

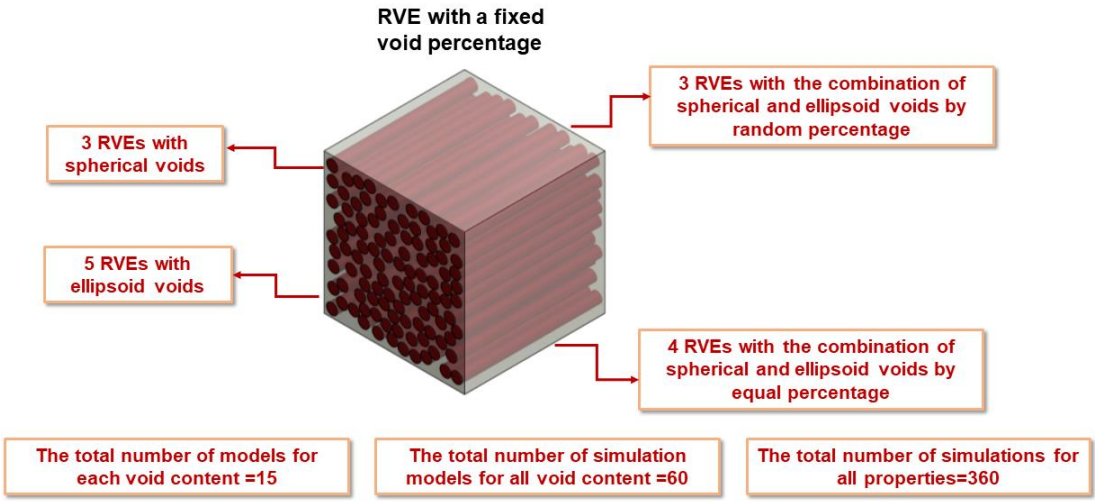

Figure 3.9: Design of simulations for RVEs with a fixed void percentage

For a fixed void percentage, 15 RVEs was simulated. These RVEs were considered as follows: 3 RVEs with the spherical voids, 5 RVEs with ellipsoid voids, 4 RVEs with the combination of spherical and ellipsoid voids by the equal percentage, and 3 RVEs with the combination of spherical and ellipsoid voids by the different percentages. The effective material properties are calculated for 15 RVEs with 1%, 2%, 3% and 5% void percentage to thoroughly understand the effect of void shapes and locations on the constitutive coefficients.

3.2.4 Modeling fiber breakage in the RVE

Different angles of fiber breakage are introduced in the RVEs to find the effect of the angle of fiber breakage on the perturbation of the effective material properties. Thus, a unit cell with 45° and 90° of fiber breakage with respect to the fiber direction are modeled, respectively. The dimension of the RVE for fiber breakage study is determined based on the previous procedure discussed in 3.2.3. The size of the RVE for fiber breakage was considered 90 μm. the diameter of the fiber filaments, fiber locations, element types and the material properties of the fiber and the matrix are identical to the unit cell discussed previously. Figure 3.10-a shows a schematic of RVE including fiber breakage with 90° respect to the fiber direction. To consider the influence of the location of the fiber breakage on the constitutive coefficients, additional studies were performed for different location of the fiber breakage in microscale length on the constitutive coefficients.

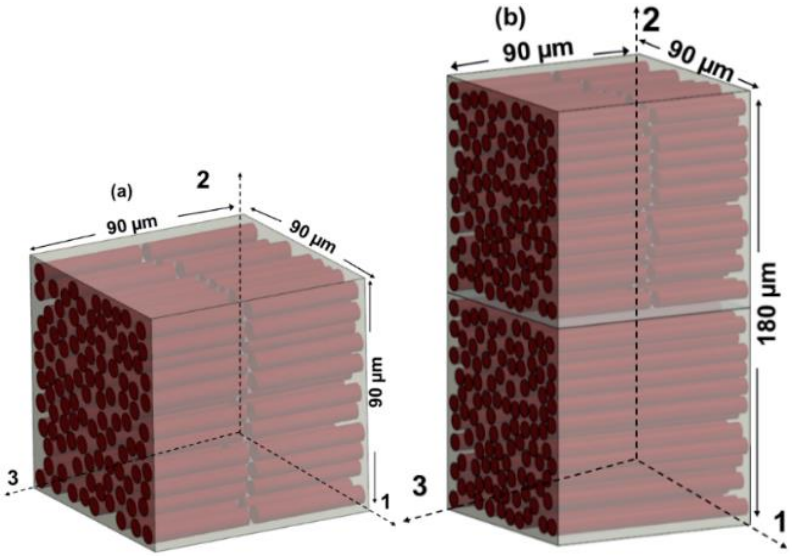

Figure 3.10: Fiber breakage with 90˚ a) in micro-scale length b) multi-scale length

To consider the effect of partial layer-wise fiber breakage on the effective material properties of an RVE, the multilayered RVE model is employed. This is achieved by simulating a two-layer RVE with one layer being pristine and the second layer being

damaged with the fiber breakage. Figure 3.10-b demonstrates multilayered RVE with different angles of fiber breakage. The configurations of the first and second layer are the same as the one-layer RVE which was modeled in section 3.2.3.

Table 3.3: Implementing periodic boundary conditions for multilayered of RVE with fiber breakage

Constitutive Coefficients	Surfaces X_{max}/ X_{min}			Surfaces Y_{max}/ Y_{min}			Surfaces Z_{max}/ Z_{min}		
C_{11}, C_{21}, C_{31}	$\Delta u_x=a$	$\Delta u_y=0$	$\Delta u_z=0$	$\Delta u_x=0$	$\Delta u_y=0$	$\Delta u_z=0$	$\Delta u_x=a$	$\Delta u_x=a$	$\Delta u_z=0$
C_{12}, C_{22}, C_{32}	$\Delta u_x=0$	$\Delta u_y=0$	$\Delta u_z=0$	$\Delta u_x=0$	$\Delta u_y=2b$	$\Delta u_z=0$	$\Delta u_x=0$	$\Delta u_x=0$	$\Delta u_z=0$
C_{13}, C_{23}, C_{33}	$\Delta u_x=0$	$\Delta u_y=0$	$\Delta u_z=0$	$\Delta u_x=0$	$\Delta u_y=0$	$\Delta u_z=0$	$\Delta u_x=0$	$\Delta u_x=0$	$\Delta u_z=c$
C_{44}	$\Delta u_x=0$	$\Delta u_y=0$	$\Delta u_z=0$	$\Delta u_x=0$	$\Delta u_y=0$	$\Delta u_z=0$	$\Delta u_x=0$	$\Delta u_x=c$	$\Delta u_z=0$
C_{55}	$\Delta u_x=0$	$\Delta u_y=0$	$\Delta u_z=0$	$\Delta u_x=0$	$\Delta u_y=0$	$\Delta u_z=0$	$\Delta u_x=c$	$\Delta u_x=0$	$\Delta u_z=0$
C_{66}	$\Delta u_x=0$	$\Delta u_y=0$	$\Delta u_z=0$	$\Delta u_x=2b$	$\Delta u_y=0$	$\Delta u_z=0$	$\Delta u_x=0$	$\Delta u_x=0$	$\Delta u_z=0$

The basic equations of the periodic boundary conditions which are applied to the multilayered RVE with fiber breakage are listed in Table 3.3 for each desired constitutive coefficient. In Table 3.3, the difference in displacements of the surfaces Y_{max}/Y_{min} is 2b which is 180 µm where the RVE has two layers. To solve the problem, equations which are listed in Table 3.3 are simplified in the FEM form for each desired constitutive coefficient as follows

$$u_i^{K+} - u_i^{K-} = \bar{S}_{ij}\left(x_j^{K+} - x_j^{K-}\right) \qquad i,j = 1,2,3 \quad K = A,B,C \tag{3-8}$$

$$[K]^g \{u_i\} = \{F\}$$

Where $\{F\}$ is equal to $\bar{S}_{ij}\left(x_j^{K+} - x_j^{K-}\right)$ and it can be a, 2b or c, $\{u_i\}$ displacement, and $[K]^g$ the coefficient of displacement. By solving Eq.(3-8), the average stresses and the average strains are calculated.

3.3 Results and discussion

To verify the procedure of applying periodic boundary conditions and element types, the result in the Ref. [52] was replicated with linear and quadratic tetrahedral elements which is non-isotropic material. The obtained results are listed in Table 3.4. By comparing the results obtained which are demonstrated in Table 3.4, Figure 3.11, and Figure 3.12, it is found that the calculated constitutive coefficients using the linear tetrahedral element type have good agreement with the existing literature.

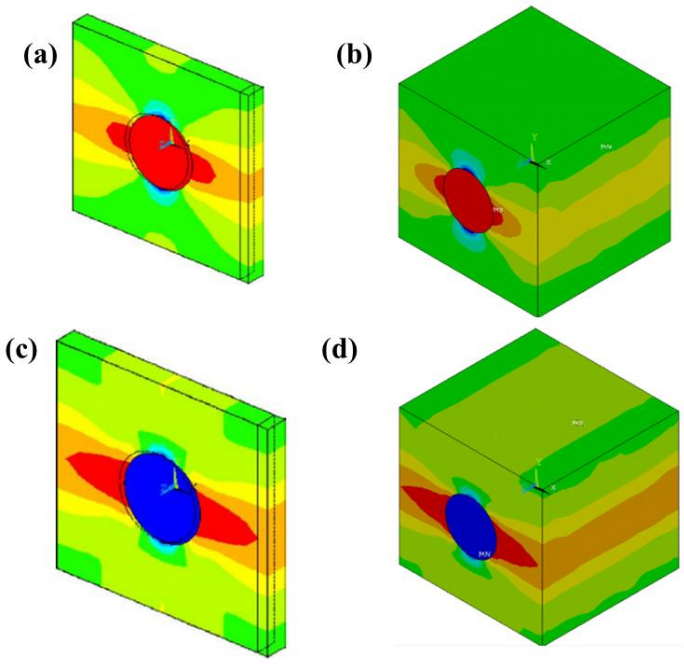

Figure 3.11: Comparing stress and strain distribution results a) T_{11} obtained by quadratic tetrahedral element [52] b) T_{11} obtained by linear tetrahedral element c) S_{11} obtained by quadratic tetrahedral element [52] b) S_{11} obtained by linear tetrahedral element

Additionally, it is observed that the computation time and memory required with the linear tetrahedral element type is less (~20%) than the simulation using the quadratic

tetrahedral element type. Thus, in this study, all the results are obtained using the linear tetrahedral elements.

Table 3.4: verification of the results with existing literature

Constitutive Coefficient	Berger et al [52] [GPa]	AHM method [52] [GPa]	Present work (Linear tetrahedral element)[GPa]	Present work (Quadratic tetrahedral element)[GPa]
C_{11}	10.86	9.74	11.06	10.86
C_{12}	4.62	5.54	4.48	4.65
C_{13}	6.02	5.95	6.05	6.04
C_{33}	35.36	35.11	35.02	35.36
C_{44}	1.85	2.17	2.18	2.05
C_{55}	1.54	2.1	1.61	1.54

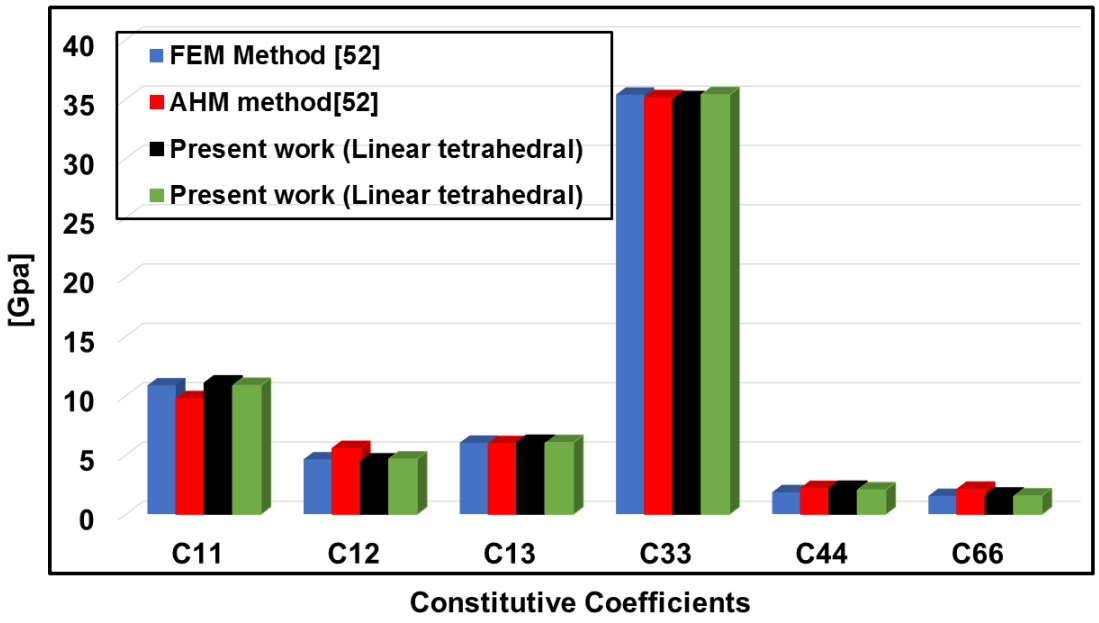

Figure 3.12: Obtained constitutive coefficients in the present work compare to Ref. [52]

Since the results obtained were verified with the results in the existing literature, the effective material properties of the RVE can be obtained with multiple fibers in the pristine state and the damaged state by dividing the average stress over the average strain. Multiple fibers RVE at pristine state

15 Multi-fiber RVE models at pristine state are solved by applying periodic boundary conditions and the constitutive matrix was obtained using the method presented in the previous section. The mean of constitutive matrix for 15 RVEs can be written as:

$$[C]=\begin{bmatrix} 8.46 & 1.27 & 2.06 & 0 & 0 & 0 \\ 1.27 & 8.46 & 2.06 & 0 & 0 & 0 \\ 2.06 & 2.06 & 116.46 & 0 & 0 & 0 \\ 0 & 0 & 0 & 4.88 & 0 & 0 \\ 0 & 0 & 0 & 0 & 4.87 & 0 \\ 0 & 0 & 0 & 0 & 0 & 3.54 \end{bmatrix} \; GPa \tag{3-9}$$

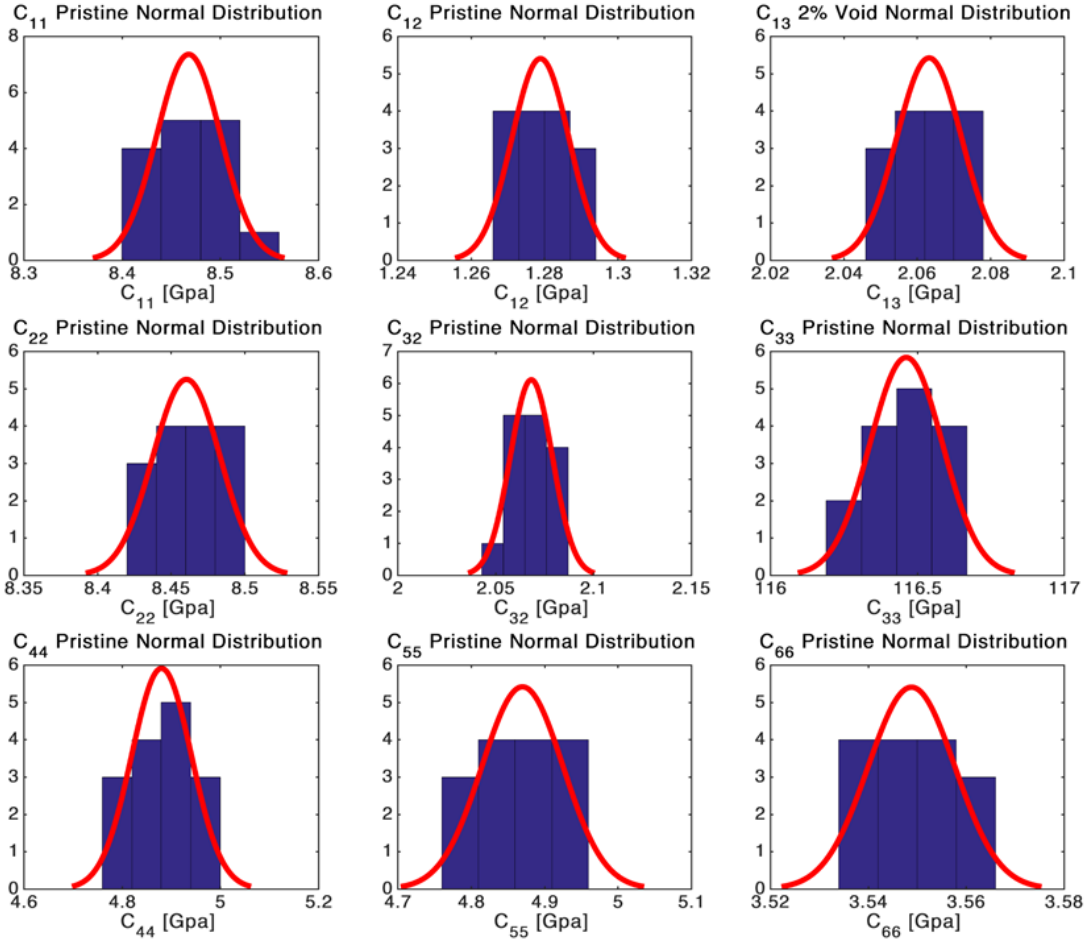

Figure 3.13: Distribution of effective material properties at pristine state

The distribution of effective material properties at pristine state due to the different fiber locations are depicted in Figure 3.13.

3.3.1 Introducing void in a unit cell

The periodic boundary conditions were implemented on the RVEs with different void contents and different void shapes. The full matrix of effective material properties and their distributions were calculated and the results with 1%, 2%, 3%, and 5% void content were evaluated. Figure 3.13 to Figure 3.16 demonstrates the minimum, mean, and maximum perturbation of each constitutive coefficient with respect to increasing the void percentage in the RVE.

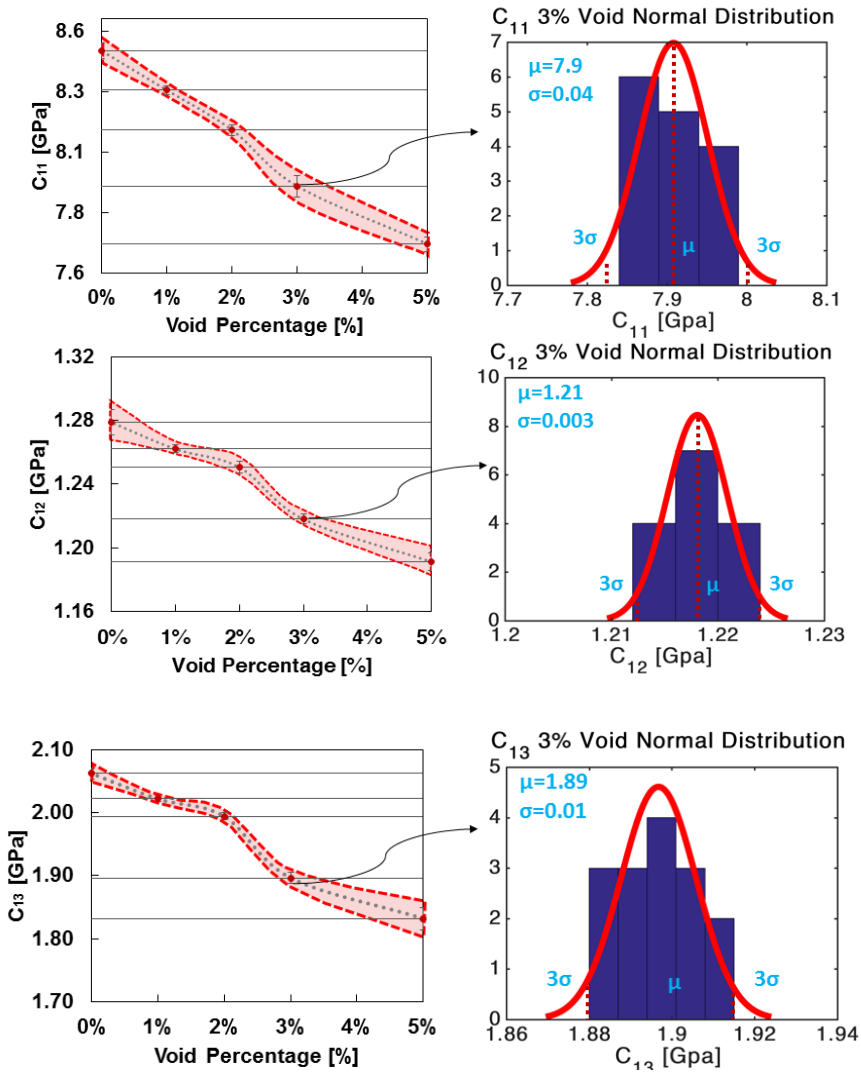

Figure 3.14: Perturbation of constitutive coefficients due to the voids

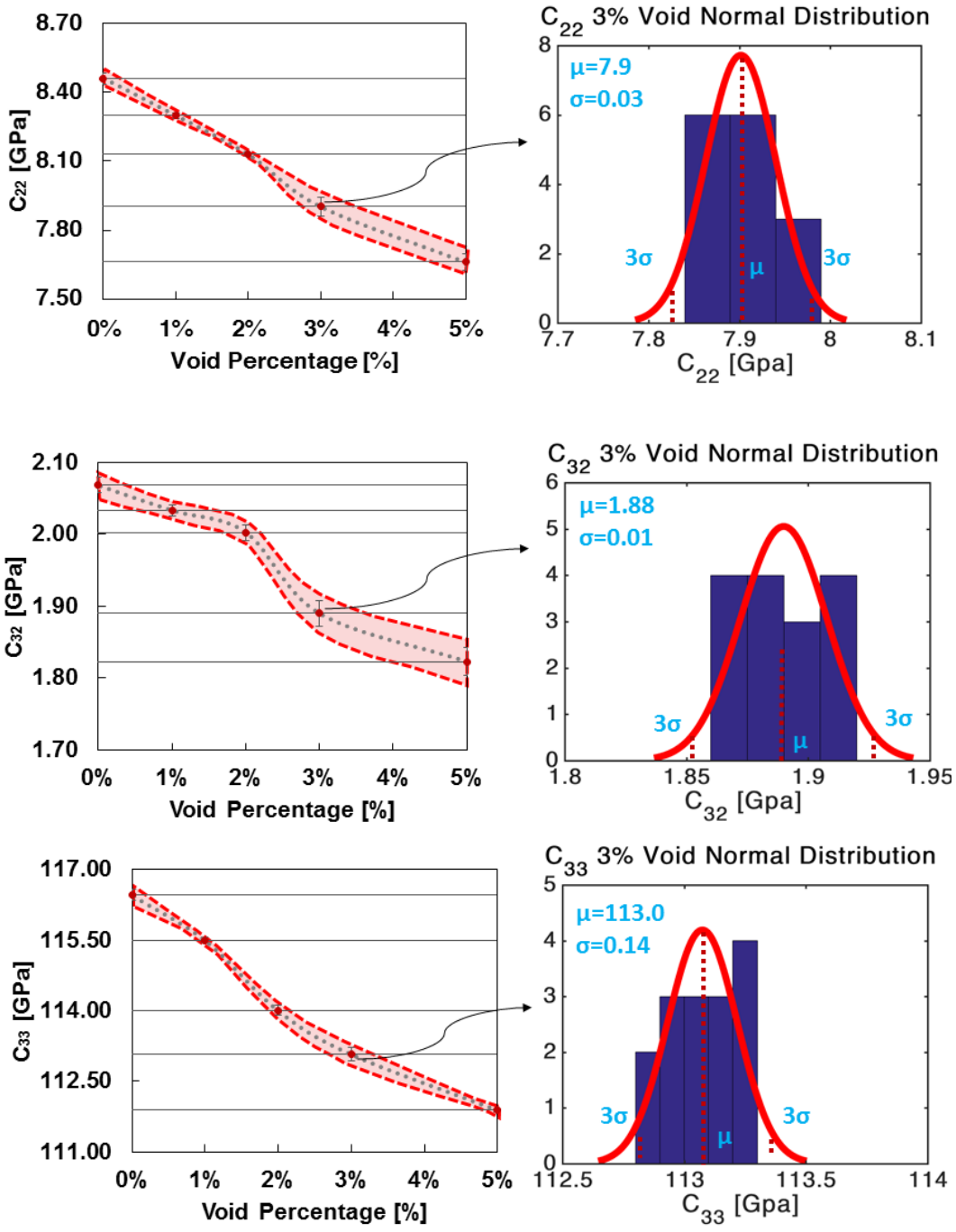

Figure 3.15: Perturbation of constitutive coefficients due to the voids

Moreover, Figure 3.13 to Figure 3.16 shows the distributions of each effective material property with 3% void content. As it shown in these figures, the effective material properties degrades with increasing percentage of void content. As shown in Figure 3.13,

the mean value of C_{11}, C_{12}, and C_{13} for 3% void content are 7.9 GPa, 1.21 GPa, and 1.89 GPa, respectively. As illustrated in Figure 3.14, the mean value of C_{22}, C_{32}, and C_{33} for 3% void content are 7.9 GPa, 1.88 GPa, and 113 GPa, respectively.

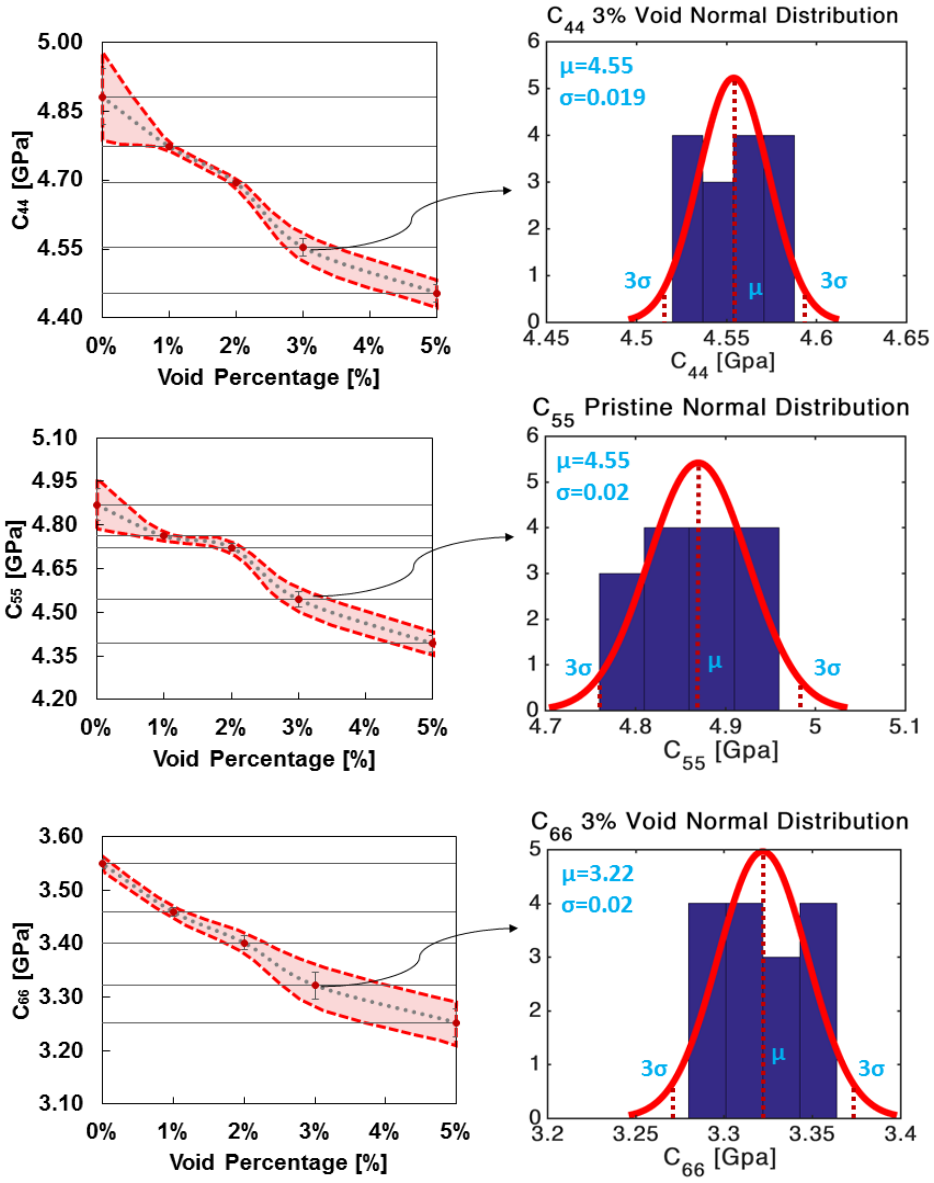

Figure 3.16: Perturbation of constitutive coefficients due to the voids

As illustrated in Figure 3.14, the mean value of C_{22}, C_{32}, and C_{33} for 3% void content are 7.9 GPa, 1.88 GPa, and 113 GPa, respectively. The change percentage of mean values of each effective material property for the RVEs with 1% void is written in Eq.(3-10).

Figure 3.17 shows the distributions of effective material properties when the void content is 1%.

$$[C]^{1\%void} = \begin{bmatrix} -1.91\% & sym & sym & 0 & 0 & 0 \\ -1.31\% & -1.91\% & sym & 0 & 0 & 0 \\ -1.95\% & -1.68\% & -0.82\% & 0 & 0 & 0 \\ 0 & 0 & 0 & -2.2\% & 0 & 0 \\ 0 & 0 & 0 & 0 & -2.2\% & 0 \\ 0 & 0 & 0 & 0 & 0 & -2.53\% \end{bmatrix} \quad (3\text{-}10)$$

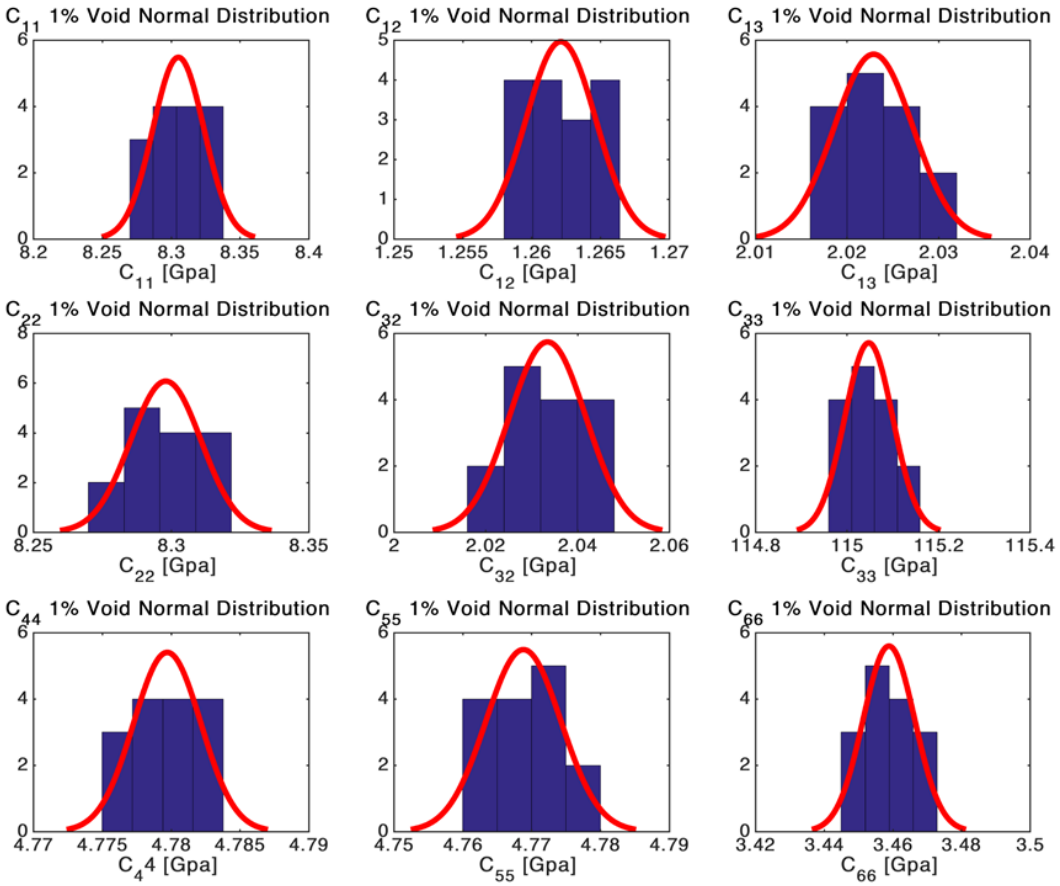

Figure 3.17: Distribution of effective material properties with 1% void content

As listed in Eq. (3-10), all the coefficients on the matrix of effective material property decreased once the void content is 1%. C_{11} and C_{22} were decreased by approximately ~2%, and the C_{33} was decreased by ~0.8% with 1% void content. C_{33} (fiber direction) have less degradation compare to C_{11}, and C_{22} since fibers contributes to carry the load. All the off-diagonal coefficients were also degraded due to the presence of voids. C_{31} and C_{32} were

decreased by ~2% and C_{21} was decreased by ~1%. C_{31} and C_{32} have higher degradation compare to C_{21} since the matrix carry the less stresses along perpendicular to fiber direction compare to pristine state. C_{44}, C_{55}, and C_{66} were decreased by almost ~3%. However, the degradation of C_{66} is higher than C_{55} and C_{66} since the matrix contributes to carry the load. The change percentage of mean values of each effective material property for the RVEs with 2% void is written in Eq. (3-11). Figure 3.18 shows the distributions of effective material properties when the void content is 2%.

$$[C]^{2\%void} = \begin{bmatrix} -3.9\% & sym & sym & 0 & 0 & 0 \\ -2.2\% & -3.9\% & sym & 0 & 0 & 0 \\ -3.3\% & -3.16\% & -2.1\% & 0 & 0 & 0 \\ 0 & 0 & 0 & -3.81\% & 0 & 0 \\ 0 & 0 & 0 & 0 & -3.77\% & 0 \\ 0 & 0 & 0 & 0 & 0 & -4.15\% \end{bmatrix} \tag{3-11}$$

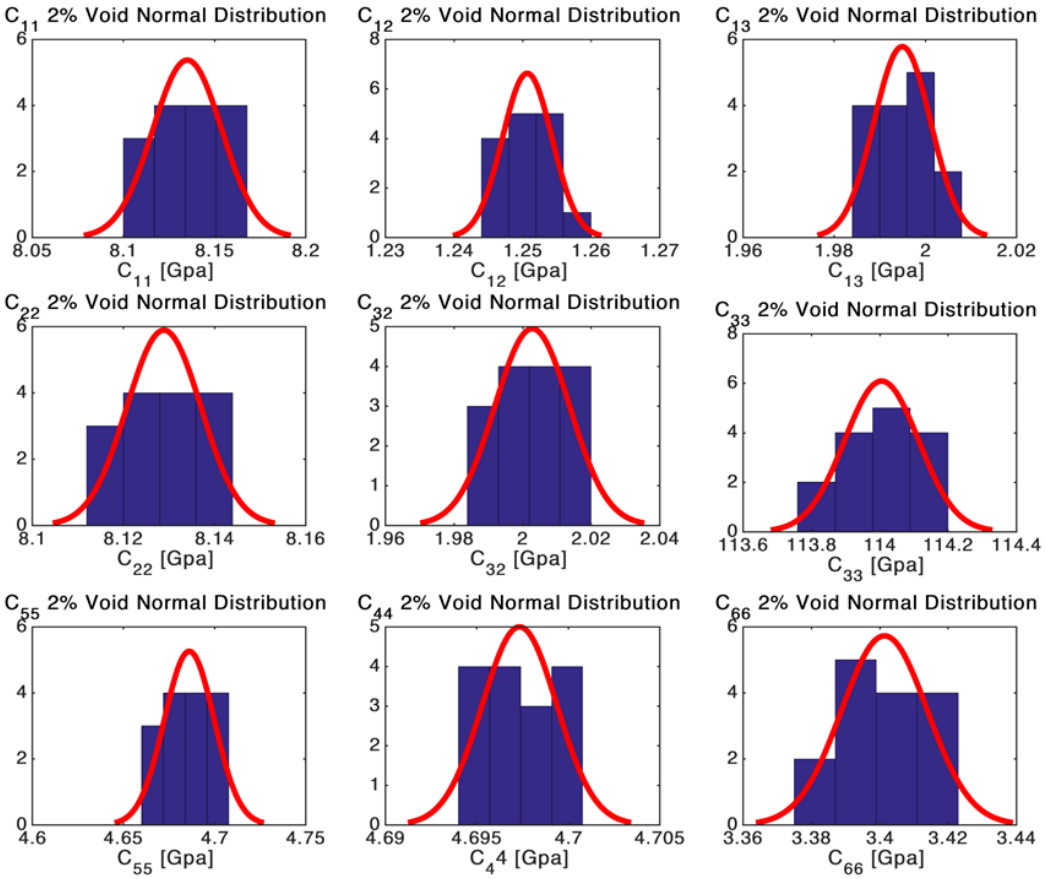

Figure 3.18: Distribution of effective material properties with 2% void content

The change percentage of mean values of each effective material property for the RVEs with 5% void is written in Eq. (3-12). Figure 3.19 shows the distributions of effective material properties when the void content is 2%.

$$[C]^{5\%void} = \begin{bmatrix} -9.4\% & sym & sym & 0 & 0 & 0 \\ -6.8\% & -9.4\% & sym & 0 & 0 & 0 \\ -11.2\% & -11.8\% & -3.9 & 0 & 0 & 0 \\ 0 & 0 & 0 & -8.7\% & 0 & 0 \\ 0 & 0 & 0 & 0 & -8.5\% & 0 \\ 0 & 0 & 0 & 0 & 0 & -9.7\% \end{bmatrix} \tag{3-12}$$

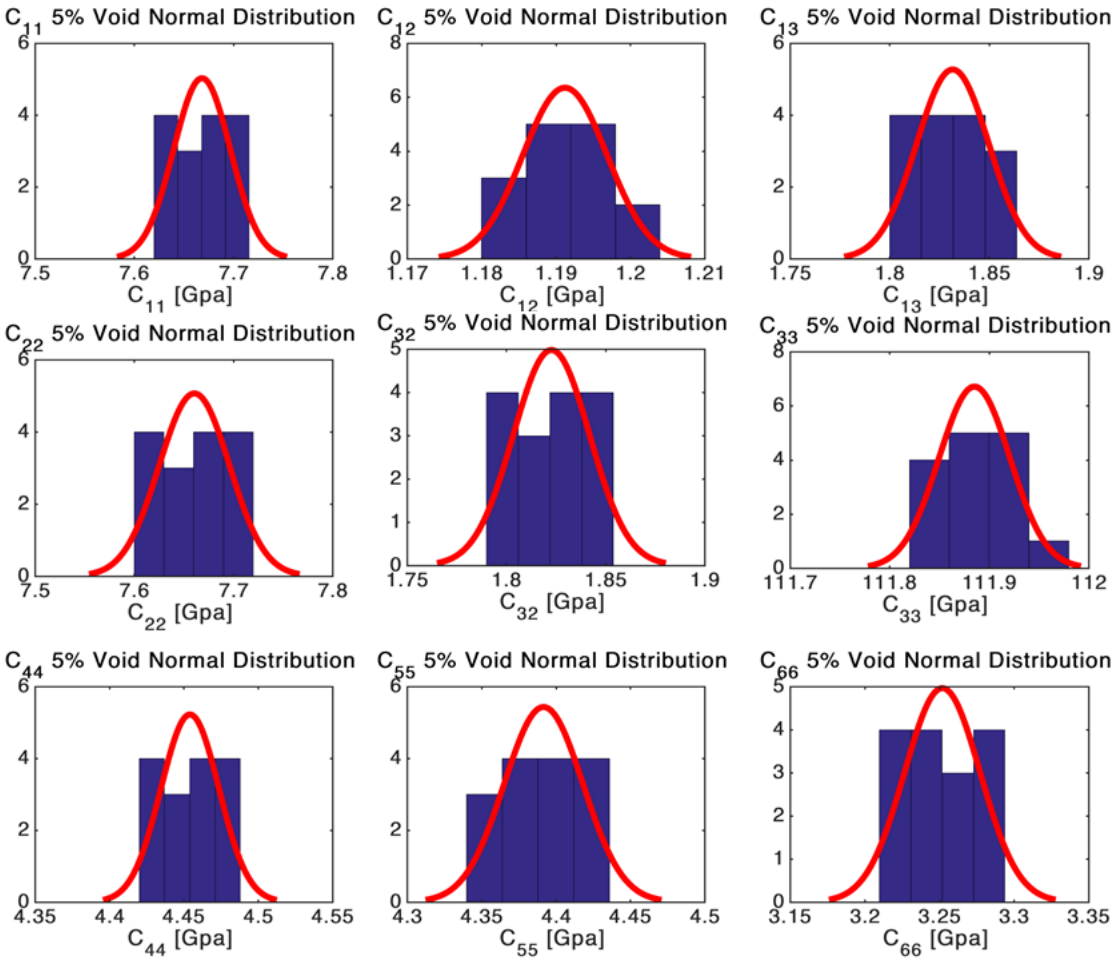

Figure 3.19: Distribution of effective material properties with 5% void content

As listed in Eq. Figure 3.19, all the coefficients on the matrix of effective material property decreased once the void content is 5%. C_{11} and C_{22} were decreased by

approximately ~9%, and the C_{33} was decreased by ~4%. All the off-diagonal coefficients were also degraded due to the presence of voids. C_{31} and C_{32} were decreased by ~11% and C_{21} was decreased by ~7%. C_{44}, C_{55}, and C_{66} were decreased by almost ~9%.

3.3.2 Engineering constant in presence of voids

The prediction of effective engineering constants has been evaluated for unidirectional composite [128]. The same procedure was followed to quantify the engineering constants. Figure 3.20 the effect of void content on the effective engineering constants. As shown in Figure 6-8, the transverse elastic modulus (E_{22}) and in-plane shear modulus (G_{12}) have good correlations with the literature [79]. In this study, additional information about effective engineering constant is quantified using a 3D RVE model. The effective elastic properties along the fiber directions (E_{33}) and out-plane shear modulus (G_{23}) and bulk modulus (k_{33}) are decreased due to the void.

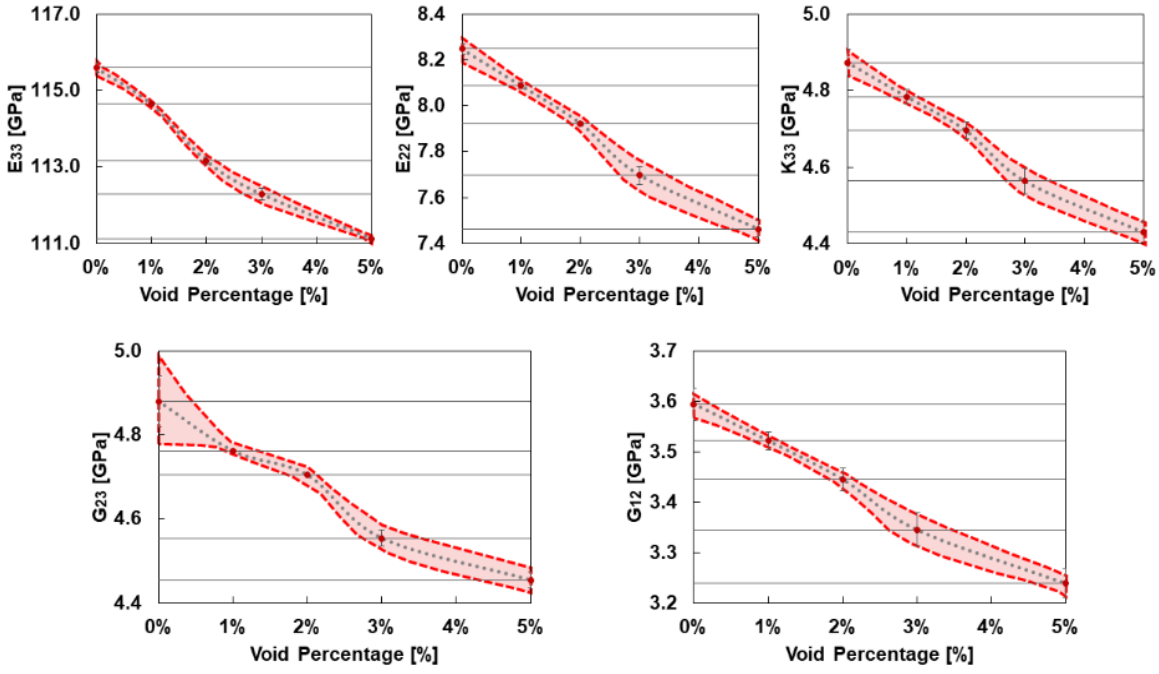

Figure 3.20: Engineering constant perturbation due to the voids

3.3.3 Microscale length model of different angles of fiber breakage

First, the microscale length model of RVE was employed to simulate fiber breakage with different angles of fiber breakage. The effective material properties for One-layer of RVE for 45° and 90° fiber breakage are listed in Eq. (3-13) and (3-14)

$$[C]^{45^\circ} = \begin{bmatrix} -0.90\% & sym & sym & 0 & 0 & 0 \\ -0.28\% & -0.88\% & sym & 0 & 0 & 0 \\ -62.10\% & -57.27\% & -91.95\% & 0 & 0 & 0 \\ 0 & 0 & 0 & -1.15\% & 0 & 0 \\ 0 & 0 & 0 & 0 & -1.12\% & 0 \\ 0 & 0 & 0 & 0 & 0 & -1.14\% \end{bmatrix} \quad (3\text{-}13)$$

$$[C]^{90^\circ} = \begin{bmatrix} -1.91\% & sym & sym & 0 & 0 & 0 \\ -2.14\% & -1.44\% & sym & 0 & 0 & 0 \\ -62.78\% & -62.54\% & -92.26\% & 0 & 0 & 0 \\ 0 & 0 & 0 & -1.15\% & 0 & 0 \\ 0 & 0 & 0 & 0 & -1.10\% & 0 \\ 0 & 0 & 0 & 0 & 0 & -1.37\% \end{bmatrix} \quad (3\text{-}14)$$

To assess the effect of fiber breakage location at microscale on material properties, the simulations were performed for 45° of fiber breakage. The results were the same as previous results for 45° of fiber breakage. In other words, the location of fiber breakage in microscale does not affect the effective material properties. Figure 3.21-a shows the perturbation of effective material properties due to the different angles of fiber breakage at microscale length. As shown in Figure 3.21-a, fiber breakage has a substantial influence on C_{31} and C_{32}. Based on Eq. (3-13) and (3-14), the effect of fiber breakage on other coefficients is approximately ignorable compared to C_{31}, C_{32}, and C_{33}. The change percentage of C_{31} was 62.10% and 67.78% 5 for 45˚and 90˚, respectively. The perturbations of C_{33} for 45˚ and 90˚ were 91.95% and 92.26%, respectively. Results verify that when the fiber breakage occurs, the composite materials tolerate less load along their fiber direction (z-direction) and consequently, the strains increased along load direction compared to pristine. Thus, the corresponding material properties, C_{31}, C_{32}, and C_{33} degraded more than the other coefficients.

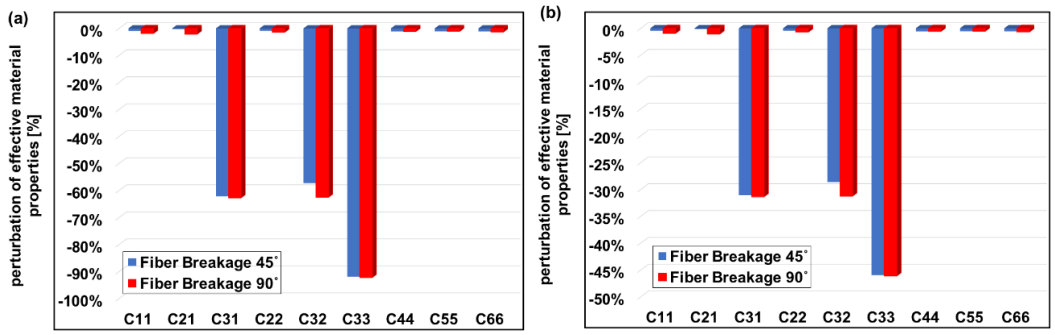

Figure 3.21: Effective material properties due to the different angles of fiber breakage a) one-layer of RVE b) Two-layer of RVE

In a practical case, the fiber breakage may occur only in one layer and other layers may remain pristine. Then, to conduct further study on the effect of fiber breakage, a two-layer model was used in the RVE. Fig. Figure 3.21-b depicts the perturbation of constitutive coefficients for different angles of fiber breakage which has been occurred into one layer of two-layered of RVE model. Based on Figure 3.21-b, fiber breakage has a significant effect on C_{31}, C_{32}, and C_{33} for different angles of fiber breakage which were decreased by nearly ~45% which is 45% less than the previous case since only one layer was damage. Like one-layer RVE with fiber breakage, the composite materials withstand less load along their fiber direction (z-direction) compared to pristine. Therefore, the material properties which are related to fiber direction degraded more. The engineering constants are quantified for fiber breakage with 45˚and 90˚. Figure 3.22 demonstrates the engineering constants in terms of fiber breakage angle.

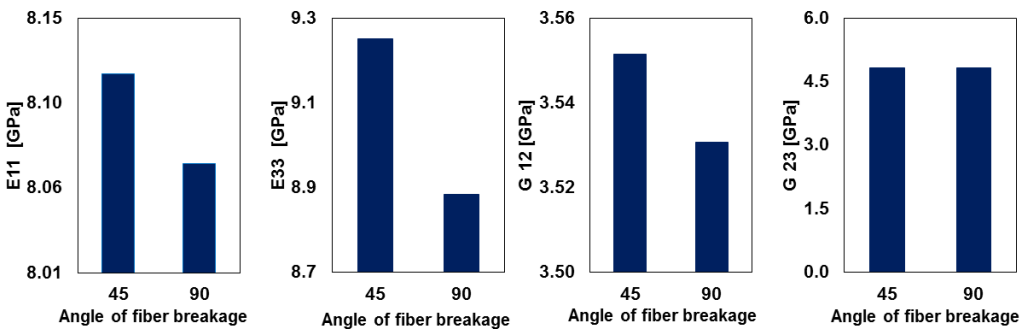

Figure 3.22: Engineering constants for different angles of fiber breakage

The results for engineering constants verified that the fiber breakage with 90˚ has lower elastic modulus along fiber direction and perpendicular to fiber direction as well as shear modulus compare to other angles of fiber breakage. This observation is as a result of more local damage at 90˚and fibers provides less strength to composite materials compare to 45.

CHAPTER 4

EFFECT OF MATERIAL DEGRADATION DUE TO PRECURSOR DAMAGES ON THE STRENGTH OF COMPOSITE PLATEs WITH OPEN HOLES

4.1 Peridynamic Theory

The PD theory is defined based on the interaction of a material point with other material points within a certain distance. This certain distance, H, is called the "horizon" of material point x, introduced by radius δ. All the material points ($\acute{x}$) placed within the horizon are called "family members" of x. In Figure 4.1, x and y are the un-deformed and deformed configuration of material points, respectively. For a bond-based theory, the interaction forces between the material point x and its family member $\acute{x}$ are defined by a pair of forces f which are in the opposite direction with identical magnitude. In the PD theory, the integral form of the equations of motion is used compare to its differential representation. The result of equations of motion are valid in the entire domain, even in the presence of discontinuity, since the calculation of derivatives of displacement is not required. The equations of motion of the PD theory is expressed in Eq. (4-1).

Where ρ is the material point density at *x*, u and $\acute{u}$ are the displacements of material point X and $\acute{X}$ at time *t*, the volume of the material point is expressed by $dV_{\acute{X}}$, and *b(X,t)* is the body force.

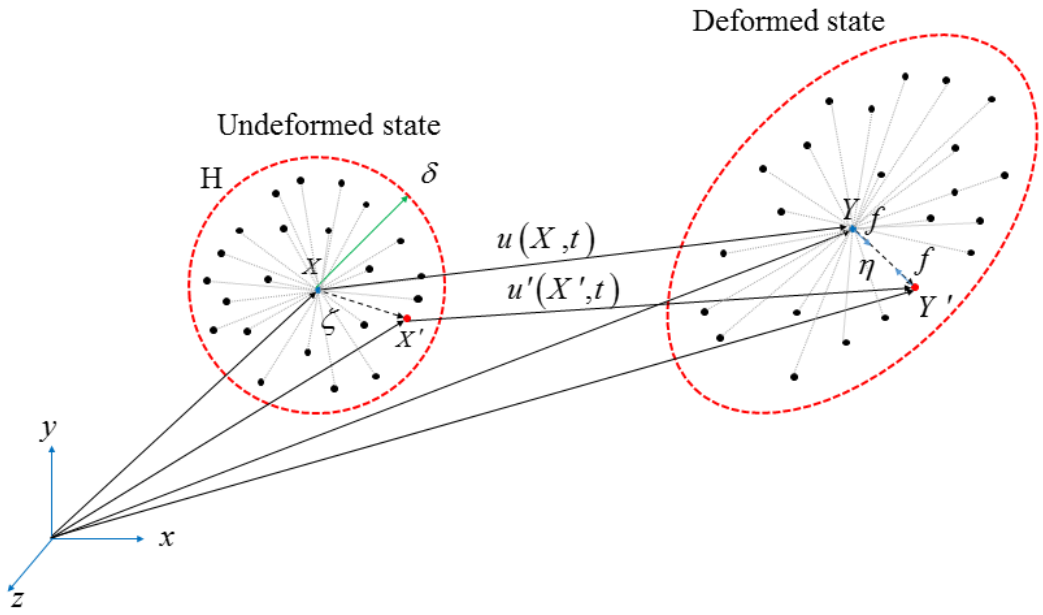

Figure 4.1: Un-deformed and deformed state configuration of x and its family member

$$\rho(x)\ddot{u}(X,t)=\int_H f(\eta,\zeta)\,dV_{X'}+b(X,t) \quad \forall x \in R, \tag{4-1}$$

As shown in Figure 4.1, the pairwise force is considered between the material point X and X' which is dependent on the relative position at un-deformed state (ζ) and deformed state (η) at time t. The relative position at the un-deformed and the deformed state are given as

$$\zeta = X - X', \quad \eta = \vec{u}'(X',t)-\vec{u}(X,t) \tag{4-2}$$

The pairwise force vector $\vec{f}$ is defined as the following

$$f(\eta,\zeta)=\mu cs\frac{\eta+\zeta}{\|\eta+\zeta\|}, \ \eta+\zeta=Y'-Y \tag{4-3}$$

According to the bond-based PD theory, μ is a parameter showing the status of a bond (Intact or broken). The parameter c indicates the bond constant, and s is the bond stretch which is expressed as Eq. (4-4)

$$s(\eta,\zeta)=\frac{\|\eta+\zeta\|-\|\zeta\|}{\|\zeta\|} \tag{4-4}$$

As indicated in Eq. (4-2) and Eq. (4-3), $\|\zeta\|$ is the bond length at the un-deformed state and $\|\eta+\zeta\|$ is the bond length after deformation. When the stretch between material points violates the critical stretch, the bond will be broken. The critical stretch is given by Eq. (4-5)

$$s_0=\sqrt{\frac{10G_0}{\pi\, c\, \delta^5}} \tag{4-5}$$

Where G_0 is the energy release rate of the material point. The bond status parameter is defined as Eq. (4-6)

$$\mu(t,\eta,\zeta)=\begin{cases}1 & if\ \ s(t',\eta,\zeta)<s_0 \quad for\ all\ \ 0\le t'\le t\\ 0 & otherwise\end{cases} \tag{4-6}$$

Damage index at the material point x can be defined as Eq. (4-7)

$$\psi(X,t)=1-\frac{\int_H \mu(t,\eta,\zeta)\,dV_{X'}}{\int_H dV_{X'}} \tag{4-7}$$

4.2 Numerical solutions and composite modeling

Numerical solutions are required to solve Eq. (4-1) using the PD method. To calculate the integral term of the internal force, the composite structure should be discretized with the number of material points. Thus, the integral term in Eq. (4-1) is replaced with a finite summation. The equations of motion can be rewritten as [106]:

$$\rho \ddot{u}_i^n = \sum_{m=1}^{M(i)} f_{iq}\left(u_m^n\left(X_m, t^n\right) - u_i^n\left(X_i, t^n\right), X_m - X_i, t^n\right) V_m + b_i^n \tag{4-8}$$

Where superscript n indicates the time step number, subscript i denotes the material point X_i, summation range $M(i)$ is the number of associated family members of material point X_i, and f_{iq} indicates the interactions between material point X_i and its associated family member. To discretize the left-hand side, the explicit central finite difference method is used.

$$\ddot{u}_i^n = \frac{u_i^{n+1} - 2u_i^n + u_i^{n-1}}{\Delta t^2} \tag{4-9}$$

Where Δt is a constant time step that is required to satisfy the stability condition. In this study, the time step is calculated using reference [129].

$$\Delta t < \sqrt{\frac{2\rho}{\sum_{p=1}^{N} \frac{c}{\left\| x_p - x_i \right\|} V_p}} \tag{4-10}$$

Similarly, Eq. (4-8) should be rewritten as a finite summation and expressed by (4-11)

$$\psi\left(X, t\right) = 1 - \frac{\sum_{m=1}^{M(i)} \mu\left(t, \eta, \zeta\right) V_m}{\sum_{m=1}^{M(i)} V_m} \tag{4-11}$$

In an isotropic material, the interaction forces between the material points within the horizon are independent of direction. However, it is required to consider the directional dependency in the composite structure to calculate these forces. Therefore, to model a fiber-reinforced composite structure which fiber direction is γ, two different bond constants should be defined. These bond constants are called fiber bond and matrix bond. As depicted in Figure 4.2, the fiber bond describes interaction between two material points

along fiber direction. However, the matrix bond introduces the interaction between the material points which are not along fiber direction. The fiber bond constant is indicated by c_f while the matrix bond constant is denoted by c_m. The fiber direction is specified by γ.

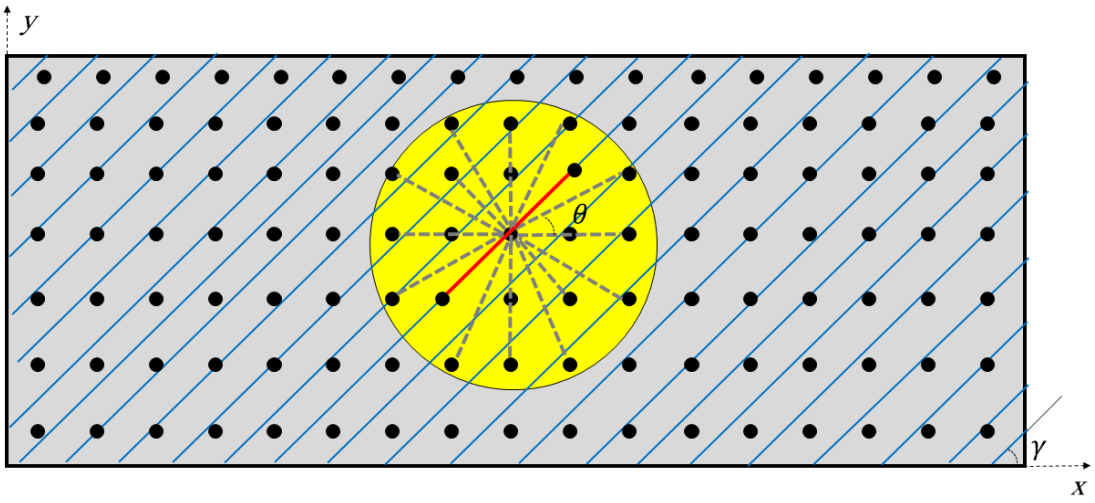

Figure 4.2: Fiber bond and matrix bond configuration in unidirectional composite

The fiber bond and matrix bond are expressed by (4-12):

$$c_f = \frac{2E_1\left(E_1 - E_2\right)}{\left(E_1 - \frac{1}{9}E_2\right)\left(\sum_{m=1}^{q}\xi_{qi}V_q\right)}, \quad c_m = \frac{8E_1E_2}{\left(E_1 - \frac{1}{9}E_2\right)l\,\delta^3} \tag{4-12}$$

Where E_1 and E_2 are the elastic material properties of the unidirectional composite, ζ_{mi} is the distance between the material points x_i, and q is the total number of material points along fiber direction, and l is the thickness of the unidirectional composites. The bond constant c is obtained based on directional dependency. Eq. (4-13) can be written for calculating bond constant.

$$c = \begin{cases} c_f + c_m & if \quad \theta = \gamma \\ c_m & if \quad \theta \neq \gamma \end{cases} \tag{4-13}$$

The critical stretch for a unidirectional composite is dependent on fiber direction. The critical stretch can be defined based on fiber bond and matrix bond. The critical stretch for the failure of matrix bond and fiber bond is expressed as (4-14) [129].

$$S_f = \sqrt{\frac{10\,G_f}{\pi\, c_f\, \delta^5}}, \quad S_m = \sqrt{\frac{10\,G_m}{\pi\, c_m\, \delta^5}} \tag{4-14}$$

In Eq.(4-14), the critical energy release rates are denoted by G_m, and G_f, respectively.

4.3 Results and discussion

The peridynamic technique is applied to the unidirectional composite plates containing one, two, and four open holes with different orientations. The effects of the hole orientations and fiber direction are studied on the strength of the composite plates and crack propagation. To validate the PD results, the strength and crack propagation path of the open-hole composite plates are compared to the results of the experimental study. Furthermore, the effects of the degraded material properties on the strength of unidirectional composite plates are considered. To conduct this study, the degraded material properties are used to calculate the updated bond constant around the holes.

4.3.1 Geometry of problem

The unidirectional plates with 12-inch in length, 1.5-inch in width, and 0.059-inch in thickness with five different hole configurations are considered in the present study. All hole diameters are ¼-inch and the distance between holes is 0.75-inch side by side. Figure 4.3 to Figure 4.5 illustrates the problem geometry adopted in this study. As shown in Figure

4.3 illustrates different orientations of open-hole unidirectional plates with 0˚ fiber direction.

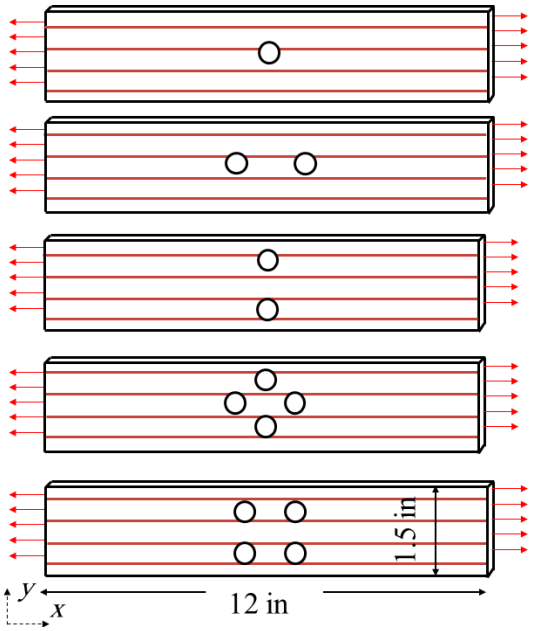

Figure 4.3: Different orientations of open-hole unidirectional composite plates with 0˚ fiber direction

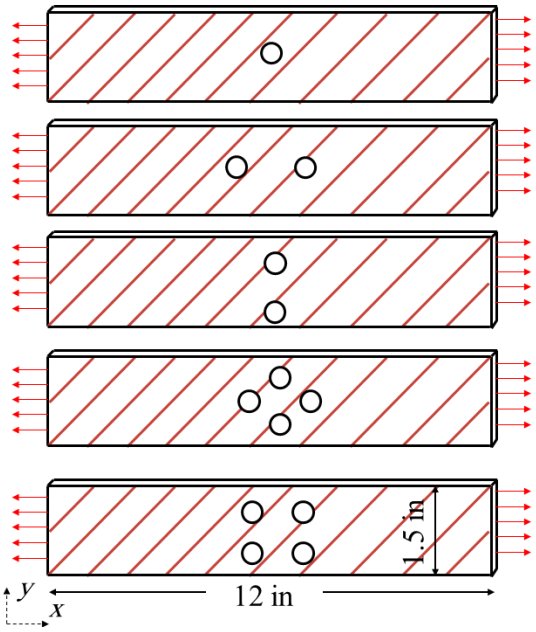

Figure 4.4: Different orientations of open-hole unidirectional composite plates with 45˚ fiber direction

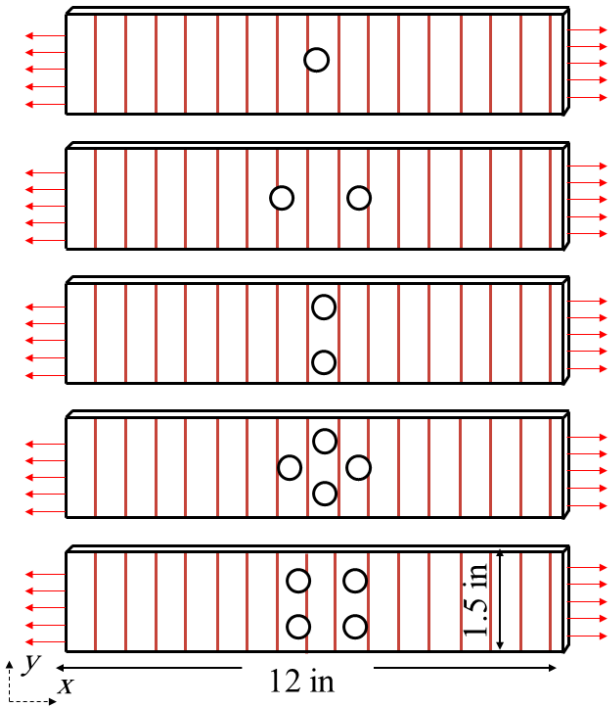

Figure 4.5: Different orientations of open-hole unidirectional composite plates with 90˚ fiber direction

Figure 4.4, Figure 4.5 depict different orientations of open-hole unidirectional plates with 45˚, 90˚ fiber direction, respectively.

4.3.2 Peridynamic simulations

A uniform space discretization is employed in this technique in such way that all the nodes have an identical volume. The model has 0.8 mm × 0.8 mm grid spacing. The unidirectional plates under the uniform velocity of 2 m/s. The time step is selected $\Delta t = 2\times10^{-8}$ s. The material properties of the unidirectional composite are listed in Table 4.1.

Table 4.1: The material properties of unidirectional composite materials

E_1 (GPa)	E_2 (GPa)	ν_{12}	Density (Kg/m^3)
116	8.5	0.33	1580

The peridynamic method was applied to the unidirectional composite plate with one hole for 0˚, 45˚, and 90˚ fiber direction. The obtained results are depicted in

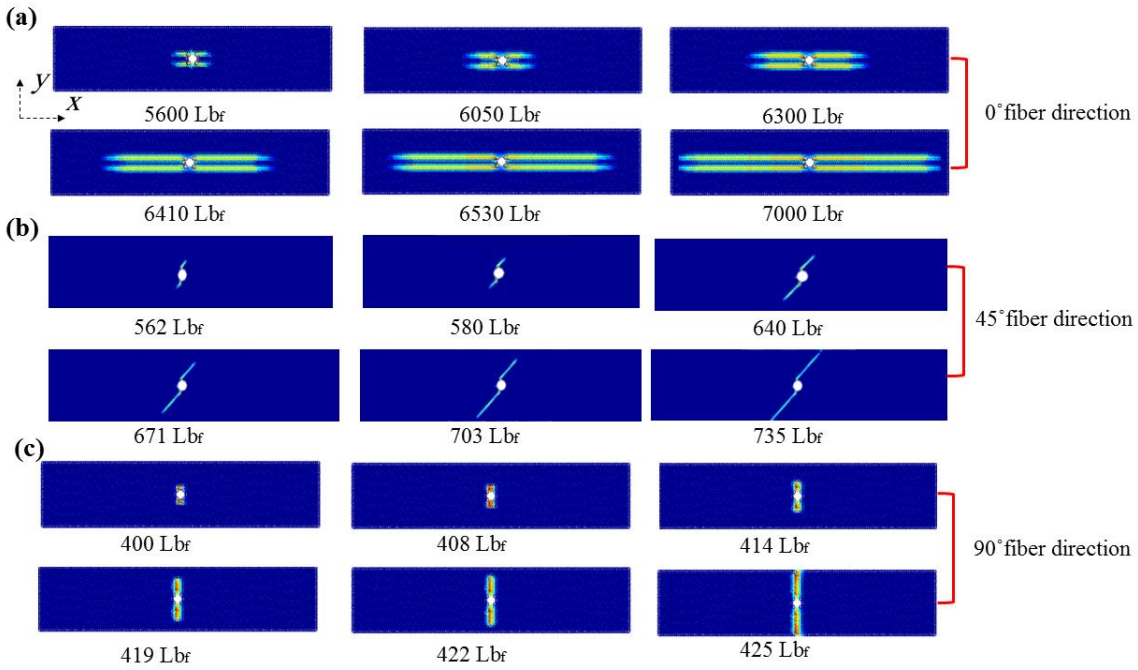

Figure 4.6: Observation of crack propagation in unidirectional composite plates with one hole for three different fiber directions a) 0˚ b) 45˚ c) 90˚

The obtained PD result for unidirectional composite with one hole has a good agreement with the literature [119]. Based on the results obtained, it is found that the failure load of the unidirectional composite plate with 0˚ fiber direction is higher than the unidirectional composite plates with 45 and 90˚ fiber directions, as shown in Figure 4.6. This can be as a result of applied load direction on the composite plates. For the plate with 0˚ fiber direction, the applied load is along fiber direction. Therefore, the load is mostly carried out through the fibers. However, fiber and matrix contribute to carrying the load in the unidirectional plates with 45˚, and 90˚ fiber directions.

Succeeding the study, the unidirectional composite plates with 0, 45, and 90 fiber directions with two horizontal holes, two vertical holes, four holes with a square array, and

four holes with a diamond array were simulated by the PD technique. As illustrated in Figure 4.7 to Figure 4.10, the crack propagated along the fiber direction.

Figure 4.7 shows the crack propagation and applied load of the unidirectional plates with two horizontal holes with three different fiber directions. As depicted in this figure, the failure load of the plates with 90˚ are lower than the plates with 45˚, and 0˚. Moreover, for plates with 0˚ fiber direction, the results showed that cracks started initiating from one side of holes. Cracks were not propagating between two holes once the cracks which were already initiated and propagated reach to the end of the plates.

Figure 4.8 depicts crack paths and failure load of unidirectional plates with two horizontal holes with three different fiber directions. As shown in this figure, the failure loads were calculated for three different fiber directions.

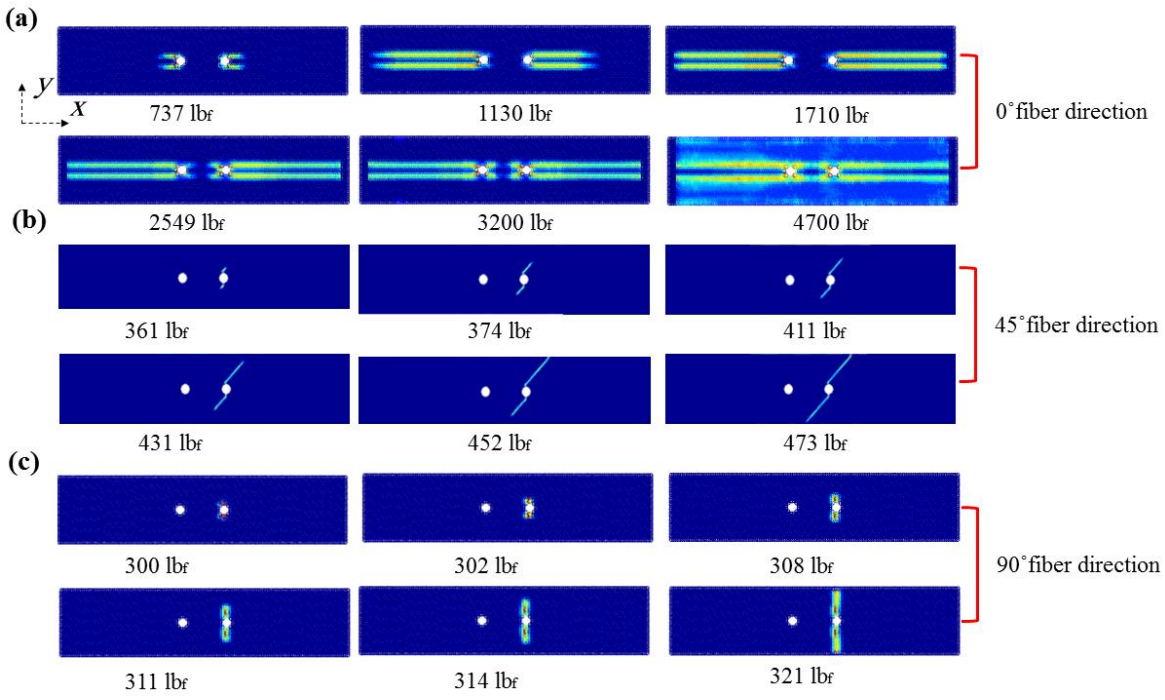

Figure 4.7: Observation of crack propagation in unidirectional composite plates with two horizontal holes for three different fiber directions a) 0˚ b) 45˚ c) 90

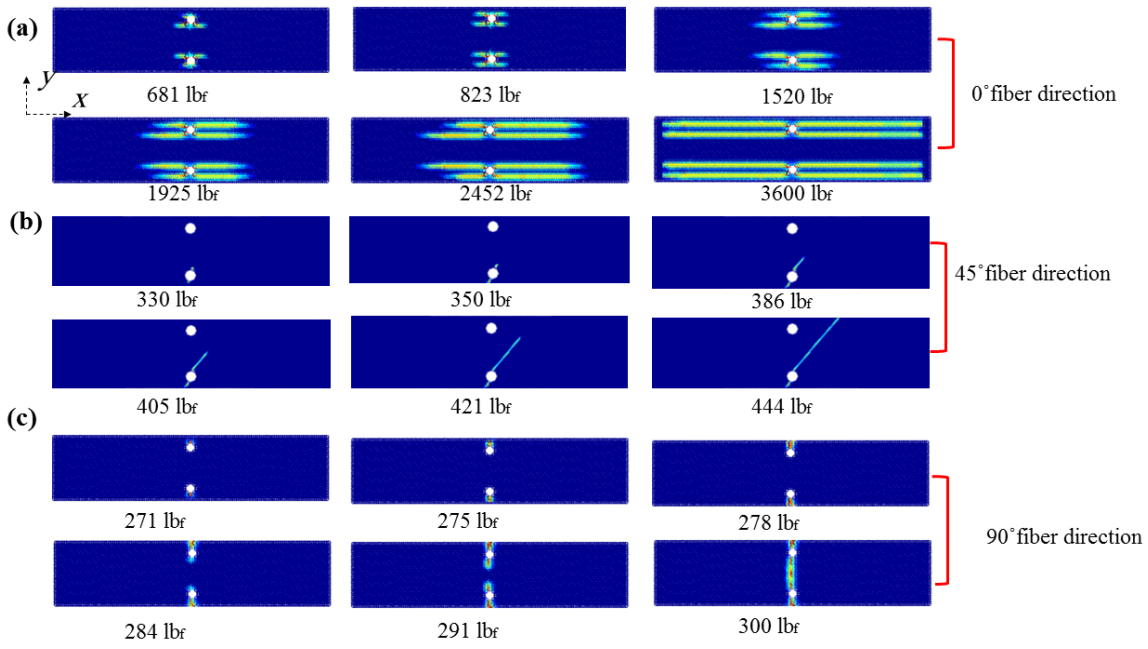

Figure 4.8: Observation of crack propagation in unidirectional composite plates with two vertical holes for three different fiber directions a) 0˚ b) 45˚ c) 90

For plates with 90˚ fiber direction, the results showed that cracks started initiating from one side of holes. Once the cracks reach to the end of the plates, the new crack cites started initiating on another side of holes. Furthermore, the results showed that the final failure load for the plate with 2 horizontal holes are higher than 2 vertical holes with the same fiber direction due to the locations of holes. The holes are closer to the edges in plates with 2 vertical holes rather than the plates with 2 horizontal holes. Hence, the crack started initiating in lower loads. The final failures were calculated at 4700 lb_f, 473 lb_f, and 321 lb_f for the plates with 2 horizontal holes with 0, 45, and 90 fiber direction respectively. On the other hand, the failure loads were obtained 3600 lb_f, 444 lb_f, and 300 lb_f for the plates with 2 vertical holes with 0, 45, and 90 fiber direction respectively.

Figure 4.9 and Figure 4.10 show the crack propagation and applied load of unidirectional plates with four holes, with a square and, diamond configurations for three

different fiber directions. As illustrated in these figures, crack only started initiating between holes when cracks that have previously started initiating to reach to the edges of the plates.

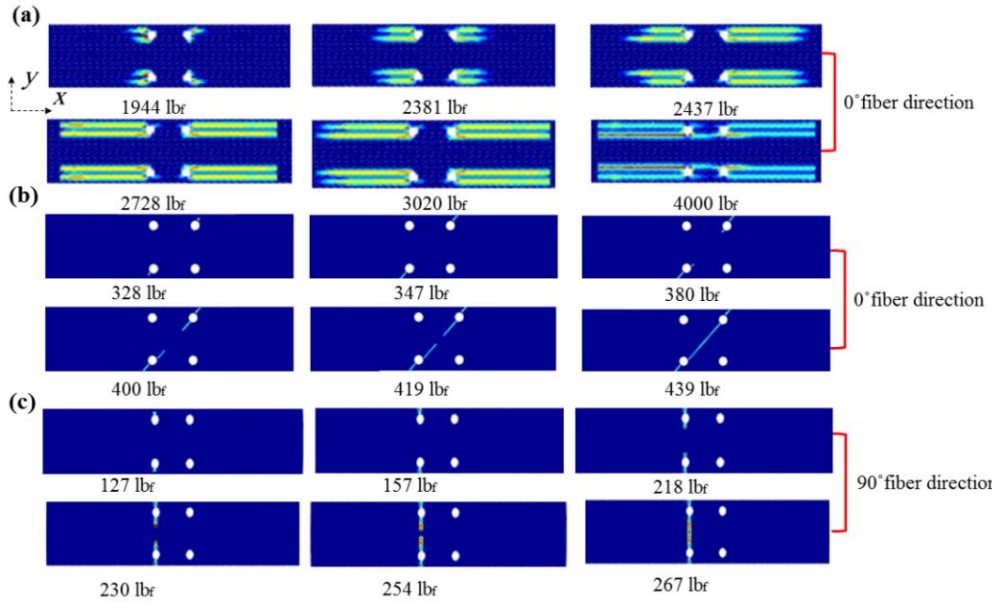

Figure 4.9: Observation of crack propagation in unidirectional composite plates with 4 holes with a square array for three different fiber directions a) 0˚ b) 45˚ c) 90

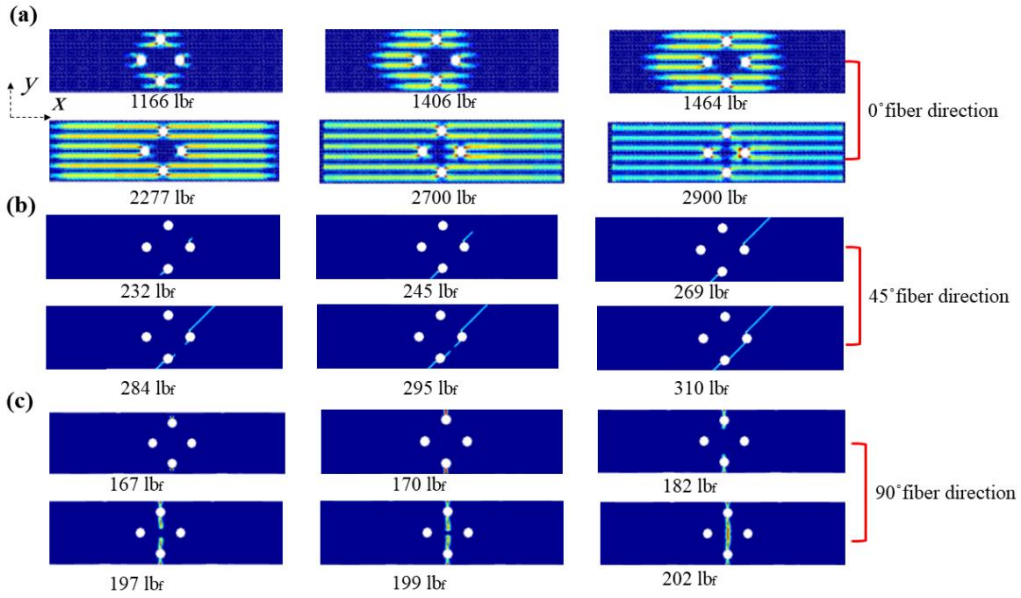

Figure 4.10: Observation of crack propagation in unidirectional composite plates with 4 holes with a diamond array for three different fiber directions a) 0˚ b) 45˚ c) 90

Based on the results, the finial failure loads of unidirectional plates with the square array for each fiber direction are higher than finial failure loads of unidirectional plates with the diamond configurations. The final failures were calculated 4000 lb_f, 439 lb_f, and 268 lb_f for the plates with the square hole orientation with 0, 45, and 90 fiber direction respectively. On other hand, the failure loads were obtained 2900 lb_f, 310 lb_f, and 202 lb_f for the plates with the diamond hole orientation and with 0, 45, and 90 fiber direction respectively.

4.3.3 Validation

The experimental study was carried out to validate the PD simulation results. Three specimens for each case were planned for tensile testing. As shown in Figure 4.11 to Figure 4.13, the experimental study was designed for 5 different holes configurations with 0˚, 45˚, and 90˚ unidirectional composite plate.

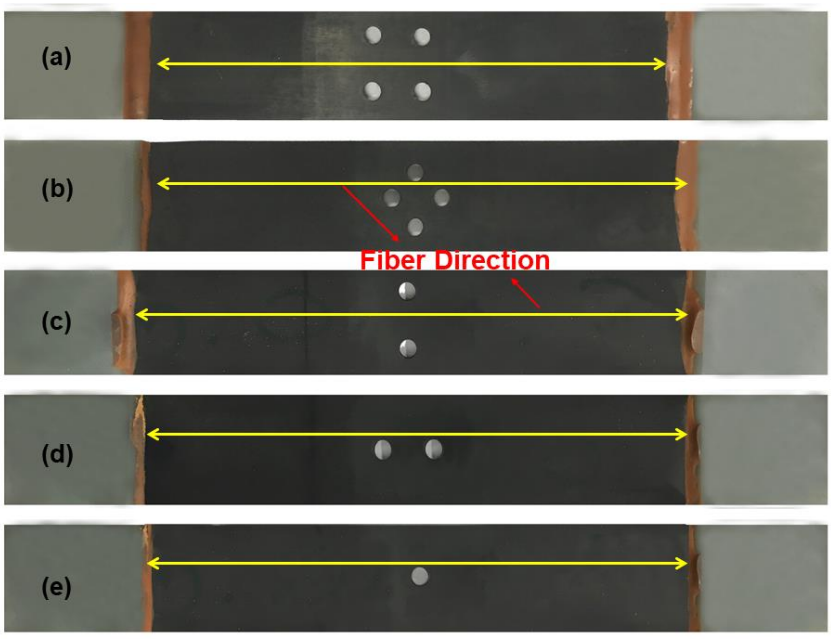

Figure 4.11: Unidirectional composite samples with 0° fiber direction with different hole orientations

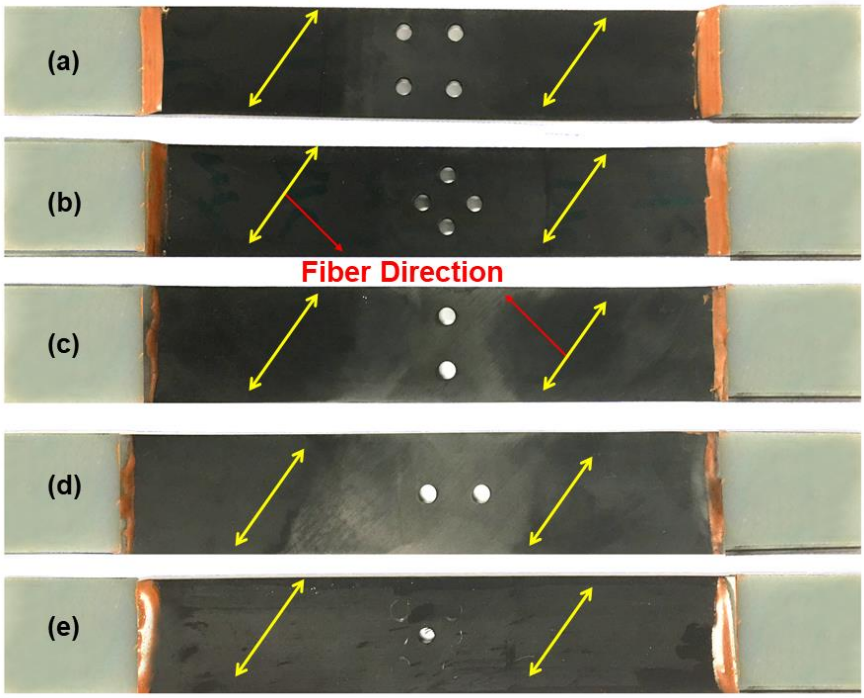

Figure 4.12: Unidirectional composite samples with 45° fiber direction with different hole orientations

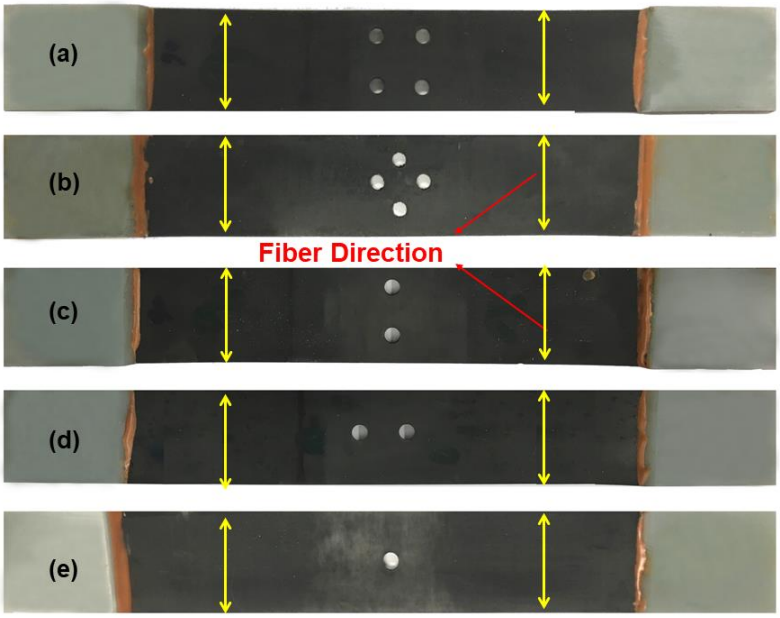

Figure 4.13: Unidirectional composite samples with 90° fiber direction with different hole orientations

The tabs were attached to the specimens with Epoxy 9394 from Loctite (48 h curing time). Specimens were tested with the tensile–tensile fatigue loading on an MTS 810 machine. The increment of load was 0.5 lb_f/s. To validate the obtained PD results, the numerical simulations are compared to the experimental study. The specimens are scanned with the scanning Acoustic microscope (SAM). The results obtained are presented at Figure 4.14 to Figure 4.17

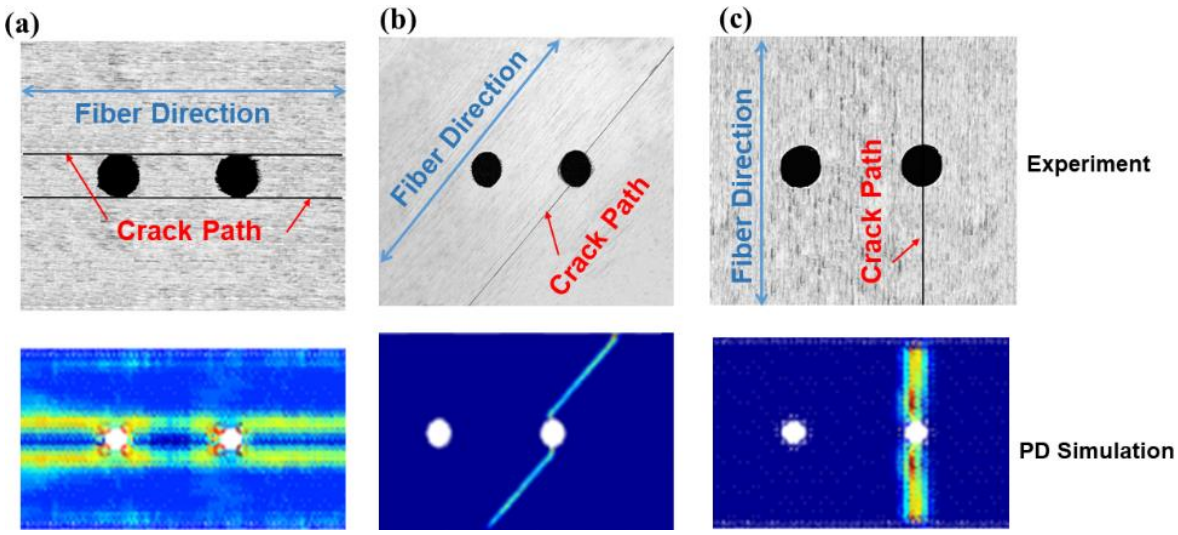

Figure 4.14: Comparison of crack propagation in unidirectional plates with 2 horizontal holes a) 0˚ b) 45˚ c) 90˚ fiber directions

Evidently, the crack paths obtained from PD simulations followed the same pattern as experimental study. This showed that PD simulation can predict the crack path accurately. As depicted in Figure 4.14, the crack path has for the unidirectional plates with 2 horizontal holes with 0˚, 45˚, and 90˚ fiber directions which have a good agreement with PD simulations. The tensile test was performed and the failure loads of unidirectional plates with different holes orientation with 45˚and 90˚ fiber direction are obtained and compared with PD simulations.

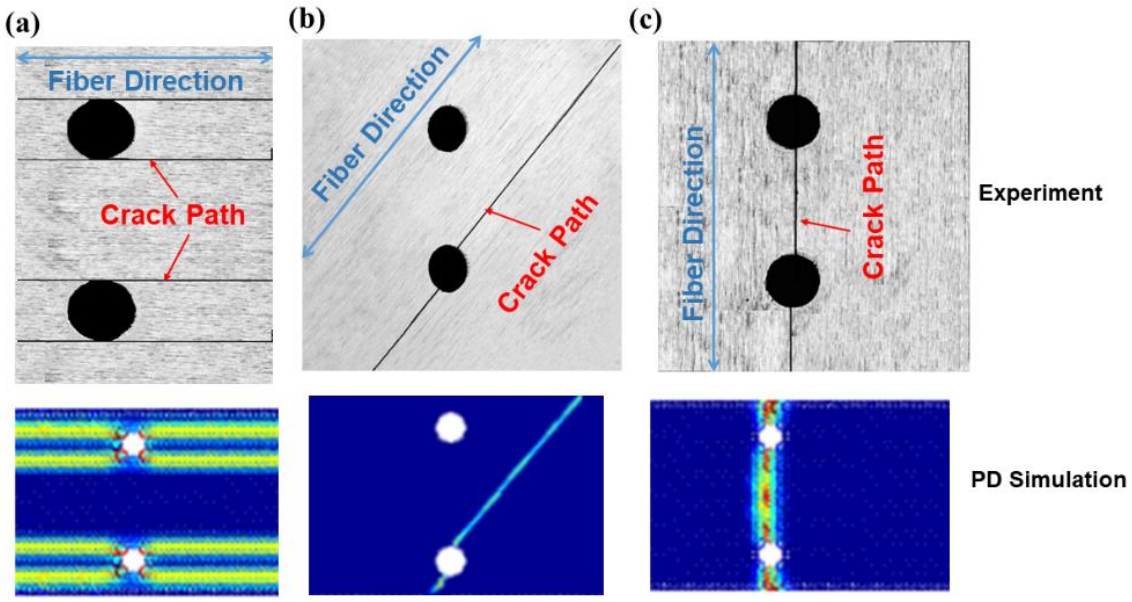

Figure 4.15: Comparison of crack propagation in unidirectional plates with 2 vertical holes a) 0˚ b) 45˚ c) 90˚ fiber directions

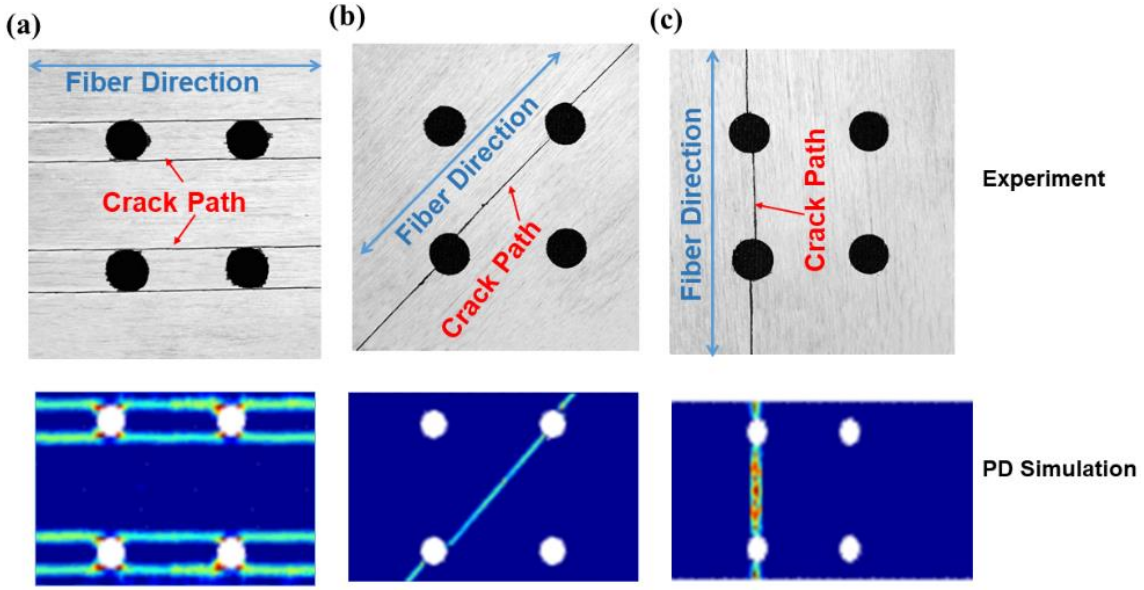

Figure 4.16: Comparison of crack propagation in unidirectional plates with 4 holes (square array) a) 0˚ b) 45˚ c) 90˚ fiber directions

The failure loads data are listed in

Table 4.2. Figure 4.18 shows the comparison of failure loads of the unidirectional plates with different holes orientations

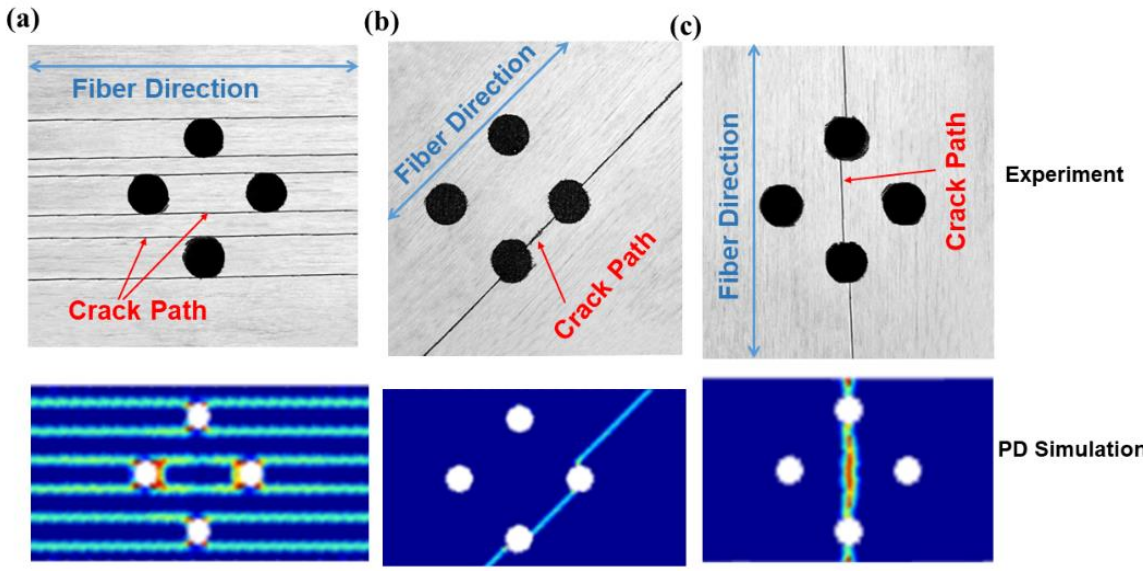

Figure 4.17: Comparison of crack propagation in unidirectional plates with 4 holes (diamond array) a) 0˚ b)45˚ c) 90˚ fiber directions

Table 4.2: Failure loads of unidirectional plates with different holes orientations and fiber direction obtained by tensile test

Hole orientations	Fiber direction	Failure loads (lb_f)
Two horizontal holes	45˚	444
	90˚	302
Two vertical holes	45˚	420
	90˚	274.5
4 holes with square array	45˚	417
	90˚	256.5
4 hole with diamond array	45˚	297.5
	90˚	187

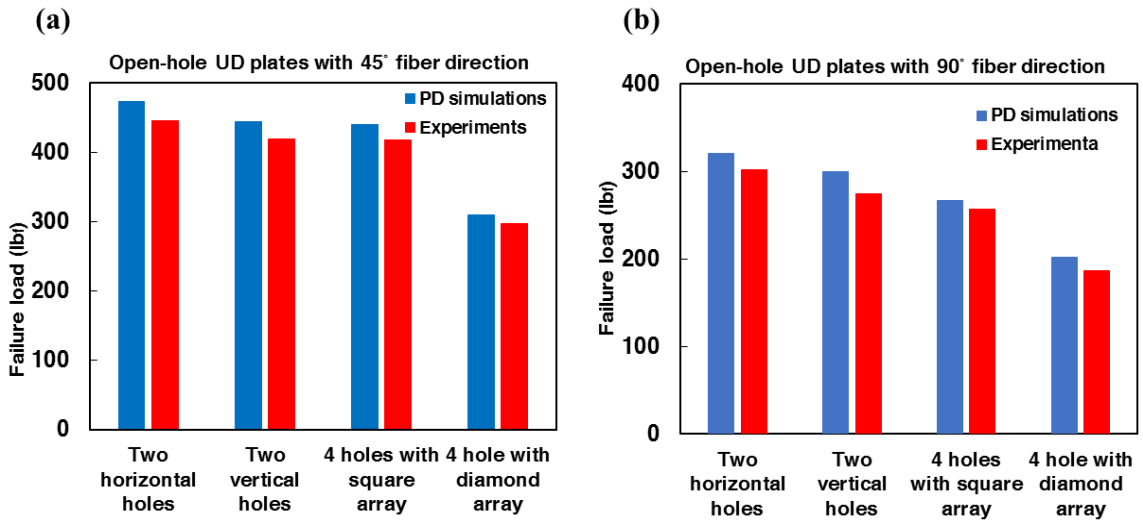

Figure 4.18: Comparison of failure loads of PD simulations and experiments

4.3.4 Effect of degraded martial properties on strength of UD plates with an open-hole

Making holes in composite materials may cause material degradation at the vicinity of their edges. Consideration of degraded material properties around the hole edges is necessary to predict the strength of unidirectional composite plate with an open hole accurately. In this study, the degraded material properties is applied to the problem using recalculating bond constant for those material points which degrade and they are located around the hole edge. Figure 4.19 shows location of considered material degradation around the hole. The engineering constants for unidirectional composite plates were calculated in section 3.3.2. Hence, the updated bond constants for degraded material points are calculated using Eq. (4-12). In this study the bond constants are calculated when the degraded area has 1%, 2%, and 3% void content. The PD method was employed using updated bond constant for the degraded area. Figure 4.20 depicted change percentage of failure loads in degraded unidirectional plates and pristine ones.

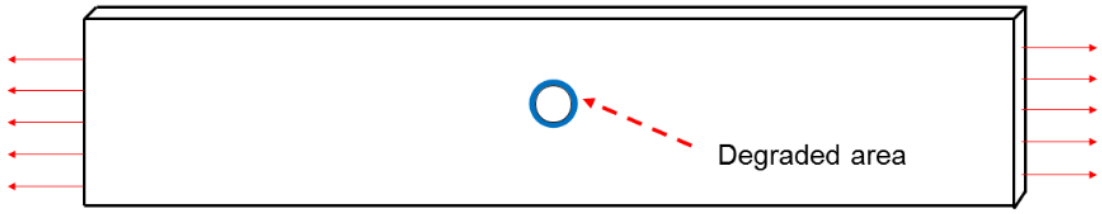

Figure 4.19: Degraded material properties area

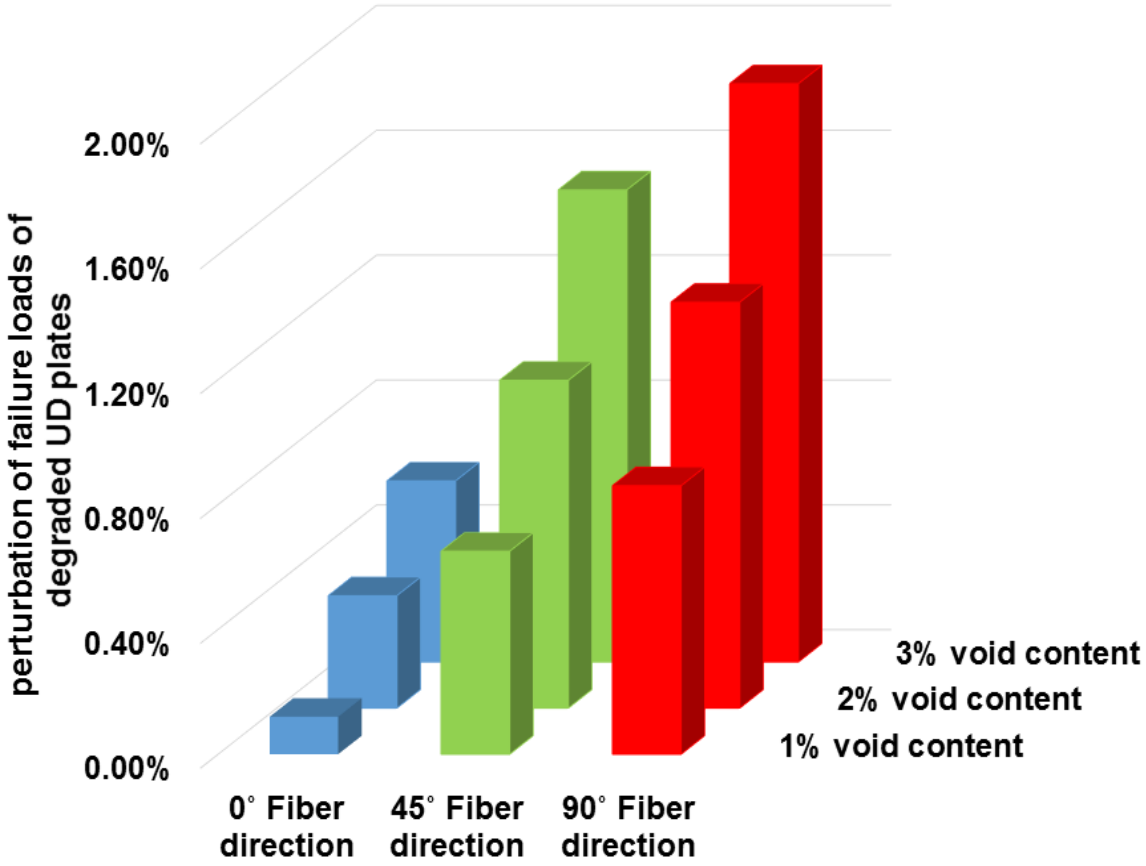

Figure 4.20: Perturbation of failure loads of degraded unidirectional plates in comparison of pristine plates

The results are listed in Table 4.3. As listed in this table, The results showed that the degraded material properties has less effect on the unidirectional plates with 0˚ fiber direction in comparison to the composite plates with 45˚, and 90˚ fiber direction since the void content has less effect on the elastic modulus along the fiber directions.

Table 4.3: Effect of degraded material properties on failure loads of unidirectional composite plate with an open hole

Void content	Fiber direction	Failure load (lb_f)
1%	0	6991.6
	45	730.2
	90	421.3
2%	0	6974.8
	45	727.2
	90	419.4
3%	0	6959.4
	45	723.8
	90	417.1

CHAPTER 5

SUMMARY AND CONCLUSION

5.1 Quantification of material degradation

In this dissertation, a method was developed to calculate the effective material properties of the composite material in presence of different types of distributed damages such as voids and fiber breakage using the finite element method. A 3D multi-fiber of RVE was considered to observe the effect of different void content, different locations of constant void, void shape and different angle of fiber breakage. Periodic boundary conditions were applied to compute the effective material properties. The results showed that all the effective material properties were decreased with the increment of void content. Additionally, the distributions of each effective material properties were calculated using modeling different locations, shapes of void content when the percentage of void content.

- For 1% void, C_{11} and C_{22} were decreased by approximately ~2%, and the C_{33} was decreased by ~0.8% with 1% void content. C_{33} (fiber direction) have less degradation compare to C_{11}, and C_{22} since fibers contributes to carry the load. All the off-diagonal coefficients were also degraded due to the presence of voids. C_{31} and C_{32} were decreased by ~2% and C_{21} was decreased by ~1%. C_{31} and C_{32} have higher degradation compare to C_{21} since the matrix carry the less stresses along perpendicular to fiber direction compare to pristine

state. C_{44}, C_{55}, and C_{66} were decreased by almost ~3%. However, the degradation of C_{66} is higher than C_{55} and C_{66} since the matrix contributes to carry the load.

- For 5% void content, C_{11} and C_{22} were decreased by approximately ~9%, and the C_{33} was decreased by ~4%. All the off-diagonal coefficients were also degraded due to the presence of voids. C_{31} and C_{32} were decreased by ~11% and C_{21} was decreased by ~7%. C_{44}, C_{55}, and C_{66} were decreased by almost ~9%.
- The results showed that all the effective material properties were decreased with the increment of void content. Based on the results, the void content has a significant effect on C_{31}, C_{32} and a minor effect on C_{33}.
    - For further study, the different angles of fiber breakage were considered in two different models of RVEs. In both cases, the fiber breakage had a significant effect on C_{31}, C_{32}, and C_{33}.
- The results showed that the different void locations, sizes, and shapes have an effect on the effective material properties. Therefore, in this study, the distributions of effective material properties were studded.
- The study confirmed that each effective material property degraded by different percentages.
- The distributions of each effective material properties are changing with different void content.

5.2 Effect of degraded material properties on the strength of composite plates with open holes

The degraded material properties are required to accurately determine the strength of unidirectional composite plates with open holes. Hence, the peridynamic method was employed on the unidirectional composite plate with five different hole configurations to calculate the strength of unidirectional composite plate with different fiber direction. Furthermore, the effects of hole orientation and fiber direction were studied on strength of plates and the crack propagation. The PD results were validated with the experiment results. The results showed that the PD method could successfully determine the strength of unidirectional plates with different fiber directions and hole orientations. The PD results were also predicted the crack path for the unidirectional composite plates and they were in a good agreement with experimental results. Next, the effect of degraded material properties on the strength of composite plates with an open hole were studied.

- In the unidirectional composite plates with one hole, the failure load of the plate with 0˚ fiber direction is higher than the plates with 45 and 90˚ fiber directions since the applied load is along fiber direction. Hence, the load is mostly carried out through the fibers. However, fiber and matrix contribute to carrying the load in the unidirectional plates with 45˚, and 90˚ fiber directions and matrix has less strength rather to fibers.
- The study showed that the strength of unidirectional plates with two horizontal holes are higher than the plates with two vertical holes.

- Based on the results, the finial failure loads of unidirectional plates with the square array for each fiber direction are higher than finial failure loads of unidirectional plates with the diamond configurations
- For unidirectional plate with two horizontal holes, the failure load of the plates with 90˚ are lower than the plates with 45˚, and 0˚. Moreover, for plates with 0˚ fiber direction, the results showed that cracks started initiating from one side of holes. Cracks were not propagating between two holes once the cracks which were already initiated and propagated reach to the end of the plates.
- The results showed that the degraded material properties has less effect on the unidirectional plates with 0˚ fiber direction in comparison to the composite plates with 45˚, and 90˚ fiber direction since the void content has less effect on the elastic modulus along the fiber directions.

CHAPTER 6
MIS·CEL·LA·NE·OUS WOR: GENERALIZED DISPERSION EQUATIONS FOR RAYLEIGH-LAMB AND SHEAR HORIZONTAL WAVES FOR CORRUGATED WAVEGUIDES

Abstract

Corrugated waveguides are periodic structures that exhibit important acoustic features such as bandgaps, and thus, exhibit the ability to filter acoustic and ultrasonic frequencies. By varying the mean thickness, corrugation height, and periodicity, one can vary their bandgaps, and hence, their propagation modes. This study aims to obtain a generalized Rayleigh–Lamb equation for corrugated waveguides such that a single equation is sufficient for both flat waveguides such as plates as well as corrugated and tapered ones. Further, the objective was to understand the effects of the corrugation height, periodicity, and mean thickness on the band structures to allow for the physics-based predictive design of wave filters. The dispersion relationships were determined using the Bloch–Floquet theorem for the scalar and vector potentials of the Helmholtz decomposition. The equations for these relationships were then solved using a logical root-finding algorithm. To verify the obtained expression, guided waveband structures were modeled based on the generalized Rayleigh–Lamb equation by setting the corrugation height to zero. The analytical solutions were validated through a comparison with the results of finite element

simulations. Finally, the effects of the corrugation height and periodicity on the propagation and evanescent wave modes were also studied.

Keywords: wave propagation, generalized Rayleigh waves, elastodynamics, corrugated structure, periodic structure, metamaterials

6.1 Introduction

For decades, researchers have been trying to create innovative technologies that can help protect industrial structures [130-133], cities (within the concept of smart cities), and even human organs from the harmful effects of acoustic and impact-generated stress waves. Hence, the phenomena of impact mitigation, energy absorption, and wave trapping, to name a few, have been explored based on manmade materials such as metamaterials and periodic structures. Impact mitigation is one of the primary methods of mitigating the detrimental effects of the shock waves generated by impacts on structures, structural components, and even the human body [134]. Several methods have been developed since the 1960s for improving the shock mitigation characteristics of materials and minimizing the peak amplitude of the generated shock waves. For instance, sandwich-like structures with fluid-impregnated foam [135] are used for blast mitigation. Foam cores with filler materials such as aerogels, soda-lime glass beads, glycerin, and tuff [136, 137] along with multiresonators [138] have also been used. Recently, the development of negative mass density metamaterials was reported [139-141] for mitigating low-frequency shock waves for impact mitigation. Metamaterials are characterized by their outstanding material properties, which are not found commonly in natural materials.

Energy absorbers are used almost in all aerospace structures such as space shuttles, satellites, and rocket components. These structures can absorb energy in two ways [142]: through an irreversible deformation and via friction or damping. Energy-absorbent structures are fabricated using energy-absorbent materials. Foams [143], structures with collapsible mechanisms [144, 145], bistable structures [146-148], periodic structures such as honeycombs, and structures combining foam materials and periodic structures [145] are all examples of such materials and structures. Although researchers were able to create some structure for impact mitigation, evolution through natural selection has resulted in several animals, such as birds, exhibiting energy-absorbing mechanisms in different parts of their bodies.

In recent years, researchers have studied the anatomy of the skull of woodpeckers with the aim of understanding how they can withstand the strong shockwaves generated from the impact of their beaks on wood substrates at 1000 g i.e. 1000 time of gravitational acceleration and not undergo damage to the brain [149-151]. It has been reported that a woodpecker's skull has a specific mechanism for absorbing the shockwaves and minimizing damage. There have been several studies at the microscopic and nanoscopic scales on the skull and beak of woodpeckers. These studies showed that the woodpecker's ability to withstand large shockwaves is related to the microstructure of their cancellous frontal skull bone and the unique architecture of their hyoid bone [152]. This microstructure starts at the front bottom of the beak and then, near the facial structure, splits into two tapered arcs, which surround the woodpecker's skull, finally ending at the upper end of the facial structure at the top end of the beak. This microstructure can effectively absorb 75% of the stress [153] that propagates to the woodpecker's brain.

Other studies have shown that, at the lower scale, the beak structure is composed of corrugated structural joints that are like stitches.

These microstructures form a corrugated mesh around the brain and are shaped such that they support and protect the brain [150-152]. The bones in the human skull are also stitched together in a similar corrugated manner. This helps them block certain lower-frequency stress waves otherwise they were not necessary. Hence, the use of bioinspired structures based on those found in nature could help mitigate the harmful effects of the high-impact stress waves on both structures and human organs and help prevent undesirable phenomena such as concussions in the human brain. In addition, understanding the underlying physics of these features could lead to the development of impact mitigation systems for cars and airplanes. To this end, the corrugated structure like stitches are essential component for impact mitigation and hence, it is essential to understand wave propagation in corrugated media. In the following paragraph background of wave propagation in corrugated media is discussed.

Corrugated waveguides have been a topic of interest for decades. Researchers have studied electromagnetic wave propagation in corrugated waveguides [154, 155] with a very high degree of corrugation as well as the stopbands of sinusoidally corrugated plates [156]. El-Bahrawy [157] studied elastic wave propagation in a sinusoidally corrugated plate with symmetric Rayleigh–Lamb modes. However, as the depth of corrugation approached zero, the passband and stopband did not disappear; this was in contradiction of the previously reported experimental and theoretical results for plates with plane boundaries. Later, El-Bahrawy [158] derived the wave propagation equation in an elastic half-space for a doubly corrugated surface. Nico et al. [159] studied the diffraction of homogeneous and

inhomogeneous plane waves on a doubly corrugated liquid/solid interface. They showed that the theory for the diffraction of sound by one-dimensional corrugated surfaces can be extended to two-dimensional corrugated surfaces as well but stop band did not disappear when corrugation approached zero.

To overcome the limitation, Banerjee and Kundu [160] reformulated the problem by considering the P-wave and S-wave potentials and studied the symmetric and antisymmetric Rayleigh–Lamb modes in sinusoidally corrugated plates. They observed passbands corresponding to both modes, which exhibited cut-on resonance along the direction of wave propagation. Kundu et. al. [161] performed experiments to quantify the stopbands and passbands for corrugated waveguides and compared the obtained results with those based on theoretical predictions [160]. The experimental results [161] confirmed that an elastic wave can propagate at the passband frequency but cannot propagate at the stopband one. Later, Das et al. [162] studied the interactions between bounded ultrasonic beams and corrugated plates using the distributed point source method. Their observations were validated by the experimental results. They reported that the strength of the reflected beam in the case of a planar waveguide is higher than that for corrugated plates. Further, the degree of backward scattering was weaker for the planar waveguides as compared to that for the corrugated plates.

Recently, the effects of the initial stress on the shear waves in a periodic waveguide with a small degree of corrugation were reported by Hawwa [163], who found that corrugated surfaces with small wavelengths have a greater effect on the wave phase speed as compared to corrugated surfaces with large wavelengths. The acoustic bandgaps in composite structures were studied by Kushwaha [164] whereas Huang et al. [165] investigated the

effects of plate symmetry on the defect states of shear horizontal (SH) waves propagating in periodically corrugated piezoelectric plates with square corrugation. They reported that, with an increase in the defect size, the frequency of the defect bands decreases.

Although corrugated waveguides have been studied in depth, a generalized expression for Rayleigh–Lamb and SH waves is still not available. In the case of most recently reported expressions [160, 161], the stopbands disappear when the corrugation depth is zero. However, the dispersion behavior in planar waveguides cannot be analyzed using the Rayleigh–Lamb equation. Hence, the following question arises: is it possible to obtain a generalized expression for guided waves that is applicable for both planar waveguides ($\varepsilon = 0$) and corrugated plates ($\varepsilon > 0$). In addition, while the stopbands and passbands of the Rayleigh–Lamb wave modes in corrugated waveguides have been studied extensively [157, 158, 160], the effects of the corrugation height and periodicity are not yet fully understood. Therefore, a generalized expression that is applicable for any depth of corrugation, any corrugation wavelength, and for any mean plate thickness is needed. Moreover, quantitative studies are necessary to understand the effects of different types of corrugations on the bandgaps of the corresponding media and the wave modes that can pass readily through these media.

In this paper, we report a generalized mathematical expression for Rayleigh–Lamb and SH wave propagation in media with and without corrugation. The equations for Rayleigh–Lamb and SH wave propagation in corrugated plates are derived analytically using scalar and vector potential functions. By solving the dispersion equations, the dispersion curves for the corrugated waveguides for propagating and evanescent waves could be obtained. Waveguides with different periodicities and different corrugation heights were analyzed

using the generalized expression. To confirm the validity of the expression, first, the Rayleigh–Lamb wave and SH wave dispersion band structures were compared using the conventional dispersion equation and the proposed generalized dispersion equation ($\varepsilon = 0$). Further, to confirm the results, the dispersion curves obtained based on the analytical solution were compared to those obtained using a finite element model. Next, the bandgaps for different corrugation heights and periodicities were studied. The governing equation for Rayleigh–Lamb wave and SH wave propagation and the boundary conditions for corrugated waveguides are discussed. Verification of the results, the dispersion curve for different corrugations, and bandgap study are explained in the results and discussion section.

6.2 Underlying theory

To study Rayleigh-Lamb wave and SH wave propagation, let us consider a periodically corrugated elastic waveguide plate with isotropic and homogenous material properties. Figure 6.1 shows a schematic of the corrugated plate. As can be seen in the figure, *h* is half of the average thickness of the plate, which is *d*. The corrugation depth is ε whereas *e* is the corrugation coefficient, which is to be multiplied with *h* to control the corrugation depth. The wavelength of the periodic waveguide is *D*. The governing equation of motion can be written in the Cartesian coordinate system. The equations for the surfaces (top with + and bottom with -) of the plate can be written as

$$\begin{aligned} x_2^+ &= h + \varepsilon\cos(2\pi\, x_1/D) \\ x_2^- &= -h - \varepsilon\cos(2\pi\, x_1/D) \end{aligned} \tag{6-1}$$

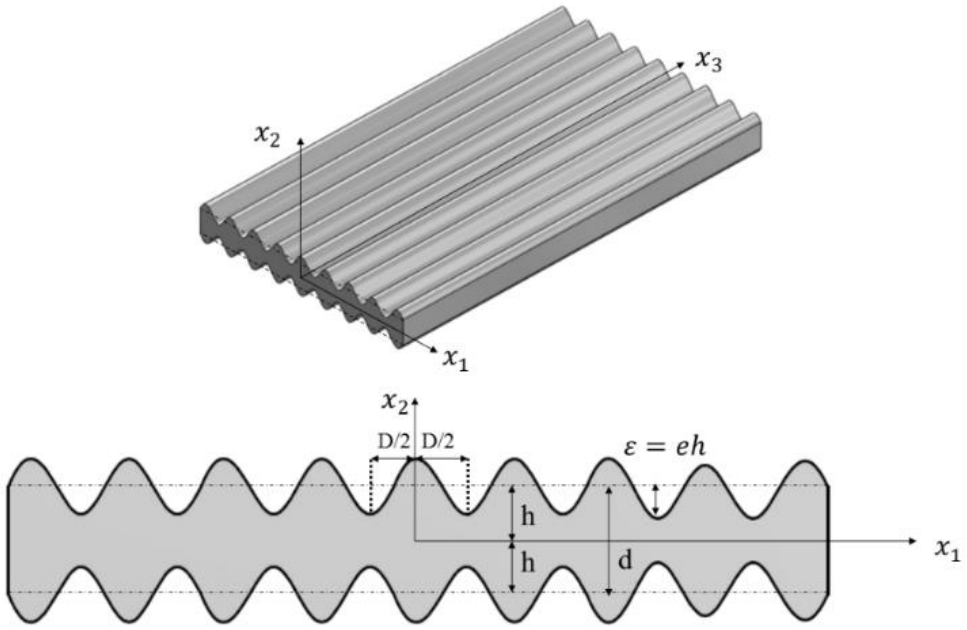

Figure 6.1: Schematic of corrugated plate.

where $-D/2 \leq x_1 \leq D/2$ and $\varepsilon = eh$. Further, the positive and negative superscripts represent the top and bottom surfaces, respectively. The fundamental equation of motion or the Navier's equation for isotropic solids can be written as

$$(\lambda + 2\mu)u_{j,ji} - \mu \in_{ijk} \in_{kpq} u_{q,pj} + f_i = \rho \ddot{u}_i \tag{6-2}$$

where λ and μ are the Lamé constants, $\in$ is the permutation symbol, and u_i is the displacement field. To derive the stress and displacement equations for Rayleigh–Lamb wave propagation, both compressional waves (P-waves) and shear waves (SV-waves) are considered. On applying the Helmholtz decomposition, $u_i = \phi_i + \in_{ijk} \psi_{k,j}$, where ϕ and ψ are two potential functions. Eq. (6-2) can be divided into two Helmholtz equations for a planar two-dimensional case, where the out-of-plane displacement (u_3) is assumed to be zero.

$$\nabla^2\phi + k_p^2\,\phi = 0 \text{ and } \nabla^2\psi + k_s^2\,\psi = 0 \tag{6-3}$$

To obtain Eq. (6-3), it is assumed that plane harmonic monochromatic waves propagate through the structure in Figure 6.1, such that the time-harmonic part of the potentials is $e^{-i\omega t}$. A solution for Eq. (6-3) for periodically corrugated media can be obtained using the Bloch theorem [166]. When studying waves in phononic crystals [167], the Bloch theorem is used directly with the displacement field $u_i(x_j) = A\,e^{i(k.x+G.x)}$, where $G = \frac{2\pi n}{D}$ and D is the periodicity of the structure or the length of a single wave in the periodic structure. Further, n take the values $0,\ \pm 1,\ \pm 2,\ \pm 3$. In the present study, the Bloch theorem was used directly with the potential functions, ϕ and ψ, which automatically satisfy the governing equation of motion.

All the up-going and down-going P-waves and SV-waves can be written in terms of the scalar and vector potential functions, which are given by Eqs. (6-4) and (6-5), respectively. As can be seen from Figure 6.1, the plate exhibits periodicity only along the x_1-axis. Thus, the Bloch potentials are assumed only for the x_1-axis. To determine the time harmonic part a monochromatic wave for the potentials, $e^{-i\,\omega t}$ is omitted from the equations.

$$\phi = \sum_{n=-\infty}^{n=+\infty} A_{Pun}\,e^{i\left(\eta_n x_2 + k\,x_1 + \frac{2\pi n}{D}x_1\right)} + \sum_{n=-\infty}^{n=+\infty} A_{Pdn}\,e^{i\left(-\eta_n x_2 + k\,x_1 + \frac{2\pi n}{D}x_1\right)} \quad \text{for P-wave} \tag{6-4}$$

$$\psi = \sum_{n=-\infty}^{n=+\infty} B_{SVun}\,e^{i\left(\beta_n x_2 + k\,x_1 + \frac{2\pi n}{D}x_1\right)} + \sum_{n=-\infty}^{n=+\infty} B_{SVdn}\,e^{i\left(-\beta_n x_2 + k\,x_1 + \frac{2\pi n}{D}x_1\right)} \quad \text{for SV-wave} \tag{6-5}$$

where k is the fundamental component of the wavenumber along the x_1-axis, η_n is the n-th component of the P-wave wavenumber in the x_2-direction (Eq. (6-4)), and β_n is the n-th wavenumber component in the x_2-direction for the SV-waves (Eq. (6-5)). The amplitudes

of the wave modes are designated as A and B for the longitudinal and shear waves, respectively. Subscript P corresponds to longitudinal waves and SV for shear vertical waves in the $x_1 - x_2$ plane, whereas subscript u corresponds to the up-going waves and d to the down-going waves. Further, n is used to distinguish the n-th wave mode.

$$\eta_n = \sqrt{k_p^2 - \left(k + \frac{2\pi n}{D}\right)^2} = \sqrt{k_p^2 - k_n^2} \tag{6-6}$$

$$\beta = \sqrt{k_s^2 - \left(k + \frac{2\pi n}{D}\right)^2} = \sqrt{k_s^2 - k_n^2} \tag{6-7}$$

In Eqs. (6-6) and (6-7), $k_p=\omega/c_p$ is the P-wave number and $k_s=\omega/c_s$ is the SV-wave number. Further, ω is the propagating angular frequency in rad/s. The P-wave speed is $c_p = \sqrt{\frac{\lambda+2\mu}{\rho}}$ whereas the S-wave speed in the medium is $c_s = \sqrt{\frac{\mu}{\rho}}$. The mass density of the elastic material is ρ. The displacement field can be defined using the Stokes-Helmholtz decomposition for in-plane-wave propagation, as shown below. Here, the wave potentials in Eqs. (6-4) and (6-5) should be differentiated as given in Eq. (6-8).

$$\begin{aligned} u_1 &= \frac{\partial \phi}{\partial x_1} + \frac{\partial \psi}{\partial x_2} \\ u_2 &= \frac{\partial \phi}{\partial x_2} - \frac{\partial \psi}{\partial x_1} \end{aligned} \tag{6-8}$$

The strain displacement equations for a linear elastic medium are given by

$$\varepsilon_{ij} = \frac{1}{2}\left(\frac{\partial u_i}{\partial x_j} + \frac{\partial u_j}{\partial x_i}\right) \quad i,j = 1,2 \tag{6-9}$$

Further, the stress-strain relation for a linear elastic material can be written as

$$\sigma_{ij} = 2\mu\varepsilon_{ij} + \lambda\varepsilon_{kk}\delta_{ij} \tag{6-10}$$

Using the potentials in Eqs. (6-4) and (6-5) and by substituting Eqs. (6-8) and (6-9) into Eq. (6-10), the stresses along the x_1- and x_2-directions can be written as follows:

$$\sigma_{11} = \sum_{n=-\infty}^{n=+\infty} e^{ik_n x_1} \begin{bmatrix} \left(-2\mu k_n^2 - \lambda(k_n^2+\eta_n^2)\right) A_{Pun} e^{i\eta_n x_2} + \left(-2\mu k_n^2 - \lambda(k_n^2+\eta_n^2)\right) A_{Pdn} e^{-i\eta_n x_2} \\ +(-2\mu k_n \beta_n) B_{SVun} e^{i\beta_n x_2} + (2\mu k_n \beta_n) B_{SVdn} e^{-i\beta_n x_2} \end{bmatrix}$$

$$\sigma_{12} = \sum_{n=-\infty}^{n=+\infty} e^{ik_n x_1} \begin{bmatrix} (-2\mu k_n \eta_n) A_{Pun} e^{i\eta_n x_2} + (2\mu k_n \eta_n) A_{Pdn} e^{-i\eta_n x_2} \\ +\mu(k_n^2 - \beta_n^2) B_{SVun} e^{i\beta_n x_2} + \mu(k_n^2 - \beta_n^2) B_{SVdn} e^{-i\beta_n x_2} \end{bmatrix} \quad (6\text{-}11)$$

$$\sigma_{22} = \sum_{n=-\infty}^{n=+\infty} e^{ik_n x_1} \begin{bmatrix} \left(-2\mu \eta_n^2 - \lambda(k_n^2+\eta_n^2)\right) A_{Pun} e^{i\eta_n x_2} + \left(-2\mu \eta_n^2 - \lambda(k_n^2+\eta_n^2)\right) A_{Pdn} e^{-i\eta_n x_2} \\ +(2\mu k_n \beta_n) B_{SVun} e^{i\beta_n x_2} + (-2\mu k_n \beta_n) B_{SVdn} e^{-i\beta_n x_2} \end{bmatrix}$$

Similarly, in the case of SH waves, it is assumed that the waves propagate in the $x_1 - x_2$ plane. However, the particles are displaced along the x_3-direction. In other words, u_1=u_2=0 and u_3 is nonzero. If the displacements are substituted in Eq. (2), the following equation is obtained for harmonic SH waves:

$$\nabla^2 u_3 + k_s^2 u_3 = 0 \quad (6\text{-}12)$$

The displacement field solution for u_3 can be defined as

$$u_3 = \sum_{n=-\infty}^{n=+\infty} B_{SHun} e^{i\left(\beta_n x_2 + k x_1 + \frac{2\pi n}{D} x_1\right)} + \sum_{n=-\infty}^{n=+\infty} B_{SHdn} e^{i\left(-\beta_n x_2 + k x_1 + \frac{2\pi n}{D} x_1\right)} \quad (6\text{-}13)$$

The displacement field for SH waves can only generate the following shear stresses:

$$\sigma_{31} = \mu\left(\frac{\partial u_3}{\partial x_1} + \frac{\partial u_1}{\partial x_3}\right) = \mu \frac{\partial u_3}{\partial x_1} = \mu \sum_{n=-\infty}^{n=+\infty} (ik_n) e^{ik_n x_1} \left[B_{SHun} e^{i\beta_n x_2} + B_{SHdn} e^{-i\beta_n x_2}\right]$$
$$\sigma_{32} = \mu\left(\frac{\partial u_3}{\partial x_2} + \frac{\partial u_2}{\partial x_3}\right) = \mu \frac{\partial u_3}{\partial x_2} = \mu \sum_{n=-\infty}^{n=+\infty} (i\beta_n) e^{ik_n x_1} \left[B_{SHun} e^{i\beta_n x_2} + B_{SHdn} e^{-i\beta_n x_2}\right] \quad (6\text{-}14)$$

6.3 Boundary conditions and dispersion equations

Traction-free boundary conditions are applied to the upper (x_2^+) and lower (x_2^-) surfaces of the corrugated plate. As stated previously, the upper and lower surfaces of the corrugated plate are given by Eq. (1). To derive the normal and shear stresses on these surfaces, the acting stresses on x_1-x_2 plane should be transformed along the normal and tangential directions of on these surfaces. The direction cosine of angles between The projections of the normal unit vector are given by n_1 and n_2. Note that n_1 and n_2 are the cosine direction of angles the projections of the normal unit vector along the x_1- and x_2-directions, respectively. These equations can be written as follows:

$$n_1 = \frac{(2\pi\varepsilon/D)\sin(2\pi x_1/D)}{\sqrt{\left((2\pi\varepsilon/D)\sin(2\pi x_1/D)\right)^2+1}} \quad n_2 = \frac{1}{\sqrt{\left((2\pi\varepsilon/D)\sin(2\pi x_1/D)\right)^2+1}} \text{ for } x_2^+ \qquad n_1 = \frac{-(2\pi\varepsilon/D)\sin(2\pi x_1/D)}{\sqrt{\left((2\pi\varepsilon/D)\sin(2\pi x_1/D)\right)^2+1}} \quad n_2 = \frac{1}{\sqrt{\left((2\pi\varepsilon/D)\sin(2\pi x_1/D)\right)^2+1}} \text{ for } x_2^- \tag{6-15}$$

Using Eq. (6-15), a transformation matrix can be constructed to transform the local stresses into the transformed coordinate system, x_1', x_2', and x_3. The transformation matrix, $[R]$, is constructed as follows:

$$[R] = \begin{bmatrix} n_1 & n_2 & 0 \\ -n_2 & n_1 & 0 \\ 0 & 0 & 1 \end{bmatrix}$$

$$\begin{bmatrix} \sigma'_{11} & \sigma'_{12} & \sigma'_{13} \\ \sigma'_{21} & \sigma'_{22} & \sigma'_{23} \\ \sigma'_{31} & \sigma'_{32} & \sigma'_{33} \end{bmatrix} = [R]\begin{bmatrix} \sigma_{11} & \sigma_{12} & \sigma_{13} \\ \sigma_{12} & \sigma_{22} & \sigma_{23} \\ \sigma_{13} & \sigma_{23} & \sigma_{33} \end{bmatrix}[R]^T \tag{6-16}$$

$$= \begin{bmatrix} \sigma_{11}n_1^2 + \sigma_{22}n_2^2 + 2\sigma_{12}n_1n_2 & (\sigma_{22}-\sigma_{11})n_1n_2 + \sigma_{12}(n_1^2-n_2^2) & \sigma_{13}n_1 + \sigma_{23}n_2 \\ (\sigma_{22}-\sigma_{22})n_1n_2 + \sigma_{12}(n_1^2-n_2^2) & -\sigma_{11}n_1^2 + \sigma_{22}n_2^2 - 2\sigma_{12}n_1n_2 & -\sigma_{13}n_2 + \sigma_{23}n_1 \\ \sigma_{13}n_1 + \sigma_{23}n_2 & -\sigma_{13}n_2 + \sigma_{23}n_1 & \sigma_{33} \end{bmatrix}$$

For Lamb wave and SH wave propagation, with respect to the general boundary conditions for determining the traction-free boundary conditions at the upper and lower surfaces, the appropriate stresses should be made zero. For Lamb wave propagation, the stresses that must be zero are σ'_{11} and σ'_{12}. However, for SH wave propagation, only σ'_{13} needs to be equal to zero. The boundary conditions, which are given in Eq. (6-16), are not defined well enough to allow one to find the solutions for the equations for dispersion relationships for a corrugated plate. Owing to the Bloch expansion of the wave function, it is necessary to apply the orthogonality principle. Hence, the corresponding boundary conditions for Lamb wave and SH wave propagation are multiplied with the normalized eigen functions, that is, by $\frac{e^{-ikx_1-\frac{2\pi n}{D}x_1}}{n_2^2}$ and $\frac{e^{-ikx_1-\frac{2\pi n}{D}x_1}}{n_2}$, respectively. Subsequently, the boundary conditions need to be integrated along x_1 over the period of corrugation of the plate. By doing so, one can impose the conditions of orthogonality on the boundary conditions. Thus, the resultant equations are transferred to the wavenumber-frequency domain. For Lamb wave propagation, the orthogonality-imposed boundary conditions can be given by

$$\begin{bmatrix}\bar{\sigma}'_{11}\\ \bar{\sigma}'_{12}\end{bmatrix} = \int_{-D/2}^{D/2} e^{-ik_n x_1} \begin{bmatrix} \sigma_{11}\left(\frac{n_1}{n_2}\right)^2 + \sigma_{22} - 2\sigma_{12}\left(\frac{n_1}{n_2}\right) \\ \sigma_{12}\left(\left(\frac{n_1}{n_2}\right)^2 - 1\right) + (\sigma_{11} - \sigma_{22})\left(\frac{n_1}{n_2}\right) \end{bmatrix} dx_1 \tag{6-17}$$

For SH wave propagation, the orthogonality-imposed boundary conditions can be expressed by

$$\bar{\sigma}'_{13} = \int_{-D/2}^{D/2} e^{-ik_n x_1} \left[\sigma_{13}\left(\frac{n_1}{n_2}\right) + \sigma_{23}\right] dx_1 \tag{6-18}$$

Note that the integrals $\int_{-D/2}^{D/2} e^{-ik_n x_1}\left(-2\sigma_{12}\left(\frac{n_1}{n_2}\right)\right)dx_1$, $\int_{-D/2}^{D/2} e^{-ik_n x_1}\sigma_{13}\left(\frac{n_1}{n_2}\right)dx_1$, and $\int_{-D/2}^{D/2} e^{-ikx_1}(\sigma_{11}-\sigma_{22})\frac{n_1}{n_2}dx_1$ are automatically equal to zero for the first Bloch mode, $n = 0$. Hence, the stress equations with the fundamental solution for wavenumber k along x_1 axis using $n = 0$, with one period of corrugation the stresses on the upper and lower surfaces of the corrugated plate can be expressed by Eqs. (6-19) and (6-20) for Lamb wave propagation and SH wave propagation, respectively.

$$\bar{\sigma}'_{11} = \int_{-D/2}^{D/2}\left[\frac{4\pi^2\varepsilon^2}{D^2}\sin^2\left(\frac{2\pi x_1}{D}\right)\begin{pmatrix}\left(-2\mu k^2-\lambda(k^2+\beta^2)\right)A_{pu0}e^{i\eta x_2}+\left(-2\mu k^2-\lambda(k^2+\beta^2)\right)A_{pd0}e^{-i\eta x_2}\\ +(-2\mu k\beta)B_{SVu0}e^{i\beta x_2}+(2\mu k\beta)B_{SVd0}e^{-i\beta x_2}\end{pmatrix}\right.$$
$$\left.+\begin{pmatrix}\left(-2\mu\eta^2-\lambda(k^2+\beta^2)\right)A_{pu0}e^{i\eta x_2}+\left(-2\mu\eta^2-\lambda(k^2+\beta^2)\right)A_{pd0}e^{-i\eta x_2}\\ +(2\mu k\beta)B_{SVu0}e^{i\beta x_2}+(-2\mu k\beta)B_{SVd0}e^{-i\beta x_2}\end{pmatrix}\right]dx_1 \quad (6\text{-}19)$$

$$\bar{\sigma}'_{12} = \int_{-D/2}^{D/2}\left[\left(\frac{4\pi^2\varepsilon^2}{D^2}\sin^2\left(\frac{2\pi x_1}{D}\right)-1\right)\begin{pmatrix}(-2\mu k\eta)A_{pu0}e^{i\eta x_2}+(2\mu k\eta)A_{pd0}e^{-i\eta x_2}\\ +\mu(k^2-\beta^2)B_{SVu0}\,e^{i\beta x_2}+\mu(k^2-\beta^2)B_{SVd0}e^{-i\beta x_2}\end{pmatrix}\right]dx_1$$

$$\bar{\sigma}'_{13} = \int_{-D/2}^{D/2}\mu i\beta\left(A_{SHu0}\,e^{i\beta x_2}+A_{SHd0}e^{-i\beta x_2}\right)dx_1 \quad (6\text{-}20)$$

In the above equation, the wavenumber, k, along the x_1-axis is the fundamental wavenumber of the corrugated waveguide. However, according to the Bloch theorem, if k is a solution of the system with $n = 0$, then all the other wavenumbers that follow the rule $k + \frac{2\pi n}{D}$ are also solutions of the system for all other values of n $(-\infty < n < +\infty)$. Thus, by imposing $n = 0$ in the Bloch solution for the fundamental modes, Eqs. (6-19) and (6-20) can be rewritten for the top, x_2^+, and bottom, x_2^-, surfaces. After solving the integrals in Eq. (6-19), the dispersion equation matrix for the corrugated plate can be defined as:

$$[C] = \begin{bmatrix} C_{11} & C_{12} & C_{13} & C_{14} \\ C_{21} & C_{22} & C_{23} & C_{24} \\ C_{31} & C_{32} & C_{33} & C_{34} \\ C_{41} & C_{42} & C_{43} & C_{44} \end{bmatrix} \begin{bmatrix} A_{Pu0} \\ A_{Pd0} \\ B_{SVu0} \\ B_{SVd0} \end{bmatrix} = 0 \tag{6-21}$$

where the generalized coefficients in the matrix for a corrugated or planar waveguide with a height of corrugation ε are expressed as

$$C_{11} = \mu D \left[\left(-2k^2 - S\, k_p^2 \right) T \frac{J_1(\varepsilon\eta)}{\eta} + (2k^2 - k_s^2) J_0(\varepsilon\eta) \right] E$$

$$C_{12} = \mu D \left[\left(-2k^2 - S\, k_p^2 \right) T \frac{J_1(\varepsilon\eta)}{\eta} + (2k^2 - k_s^2) J_0(\varepsilon\eta) \right] E^{-1}$$

$$C_{13} = \mu D \left[-2k\beta B \left(T \frac{J_1(\varepsilon\beta)}{\beta} - J_0(\varepsilon\beta) \right) \right], \quad C_{14} = \mu D \left[2k\beta B^{-1} \left(T \frac{J_1(\varepsilon\beta)}{\beta} - J_0(\varepsilon\beta) \right) \right]$$

$$C_{21} = \mu D \left[\left(-2k^2 - S\, k_p^2 \right) T \frac{J_1(\varepsilon\eta)}{\eta} + (2k^2 - k_s^2) J_0(\varepsilon\eta) \right] E^{-1}$$

$$C_{22} = \mu D \left[\left(-2k^2 - S\, k_p^2 \right) T \frac{J_1(\varepsilon\eta)}{\eta} + (2k^2 - k_s^2) J_0(\varepsilon\eta) \right] E$$

$$C_{23} = \mu D \left[-2k\beta B^{-1} \left(T \frac{J_1(\varepsilon\beta)}{\beta} - J_0(\varepsilon\beta) \right) \right], \; C_{24} = \mu D \left[2k\beta B \left(T \frac{J_1(\varepsilon\beta)}{\beta} - J_0(\varepsilon\beta) \right) \right]$$

$$C_{31} = \mu D \left[-2k\eta E \left(T \frac{J_1(\varepsilon\eta)}{\eta} - J_0(\varepsilon\eta) \right) \right], \; C_{32} = \mu D \left[2k\eta E^{-1} \left(T \frac{J_1(\varepsilon\eta)}{\eta} - J_0(\varepsilon\eta) \right) \right] \tag{6-22}$$

$$C_{33} = \mu D \left[(2k^2 - k_s^2) B \left(T \frac{J_1(\varepsilon\beta)}{\beta} - J_0(\varepsilon\beta) \right) \right], \; C_{34} = \mu D \left[(2k^2 - k_s^2) B^{-1} \left(T \frac{J_1(\varepsilon\beta)}{\beta} - J_0(\varepsilon\beta) \right) \right]$$

$$C_{41} = \mu D \left[-2k\eta E^{-1} \left(T \frac{J_1(\varepsilon\eta)}{\eta} - J_0(\varepsilon\eta) \right) \right], \; C_{42} = \mu D \left[2k\eta E \left(T \frac{J_1(\varepsilon\eta)}{\eta} - J_0(\varepsilon\eta) \right) \right]$$

$$C_{43} = \mu D \left[(2k^2 - k_s^2) B^{-1} \left(T \frac{J_1(\varepsilon\beta)}{\beta} - J_0(\varepsilon\beta) \right) \right], \; C_{44} = \mu D \left[(2k^2 - k_s^2) B \left(T \frac{J_1(\varepsilon\beta)}{\beta} - J_0(\varepsilon\beta) \right) \right]$$

where $S = \frac{\lambda}{\mu}, T = \frac{4\pi^2 \varepsilon}{D^2}, E = e^{ih\eta}, E^{-1} = e^{-ih\eta}, B = e^{i\beta h},$ and $B^{-1} = e^{-i\beta h}$.

Similarly, the SH wave dispersion equation matrix for the corrugated plate can be defined as follows:

$$[C^{SH}] = \begin{bmatrix} C_{11}^{SH} & C_{12}^{SH} \\ C_{21}^{SH} & C_{22}^{SH} \end{bmatrix} \begin{bmatrix} A_{SHu0} \\ A_{SHd0} \end{bmatrix} = 0 \tag{6-23}$$

Where the generalized coefficients in the dispersion matrix for a corrugated or planar waveguide can be expressed as

$$\begin{aligned} C_{11}^{SH} &= \mu D \left[i\beta J_0(\varepsilon\eta)\, e^{i\beta h} \right], \quad C_{12}^{SH} = \mu D \left[i\beta J_0(\varepsilon\eta)\, e^{-i\beta h} \right] \\ C_{21}^{SH} &= \mu D \left[i\beta J_0(\varepsilon\eta)\, e^{-i\beta h} \right], \quad C_{22}^{SH} = \mu D \left[i\beta J_0(\varepsilon\eta)\, e^{i\beta h} \right] \end{aligned} \tag{6-24}$$

To obtain the dispersion solution, the determinant of matrix [*C*] must be zero (*Det (C)=0*). The Lamb wave dispersion curve for the planar waveguide can be found if the ε value is set to zero. First, we attempted to confirm whether Eq. (6-21) would yield the same expression as that obtained using the conventional approach for determining the dispersion equations for a planar waveguide. It was found that Eq. (6-21) was similar to Eq. (6-25), which is the equation given for Rayleigh–Lamb wave dispersion in textbooks on wave propagation [168].

$$\Delta = det \begin{vmatrix} (k^2-\beta^2)e^{i\eta h} & (k^2-\beta^2)e^{-i\eta h} & 2k\beta e^{i\beta h} & -2k\beta e^{-i\beta h} \\ (k^2-\beta^2)e^{-i\eta h} & (k^2-\beta^2)e^{i\eta h} & 2k\beta e^{-i\beta h} & -2k\beta e^{i\beta h} \\ -2k\eta e^{i\eta h} & 2k\alpha e^{-i\eta h} & (k^2-\beta^2)e^{i\beta h} & (k^2-\beta^2)e^{-i\beta h} \\ -2k\eta e^{-i\eta h} & 2k\eta e^{i\eta h} & (k^2-\beta^2)e^{-i\beta h} & (k^2-\beta^2)e^{i\beta h} \end{vmatrix} = 0 \tag{6-25}$$

Hence, Eqs. (6-21) and Eq. (6-23) are the generalized dispersion equations for the Rayleigh–Lamb wave and SH wave modes in corrugated and noncorrugated flat isotropic plates. Next, the equations for the dispersion relationships in the frequency-wavenumber domain are solved using the root-finding algorithm by plugging the appropriate structural and material properties of the waveguides. The extended solutions for both real and imaginary wavenumber domains are calculated. The root-finding procedure for real and

imaginary wavenumbers is identical. This procedure is performed separately using a certain assumed frequency for a range of real and imaginary wavenumbers. Using MATLAB code, each root is calculated from Eqs. (6-21) and Eq. (6-23). Here, the procedure is described only for real wavenumbers. At a certain frequency, the determinants are calculated for all the real wavenumbers in the problem domain. The calculated determinants can be in the form of real or complex numbers. If the calculated determinants are real, the expected roots are found between two pairs of wavenumbers that have negative multiplication of calculated determinants. If the calculated determinants are complex, the roots are found between two pairs of wavenumbers that exhibit negative values after the multiplication of their real and imaginary parts. The procedure is performed for the rest of the frequencies until the entire frequency domain has been covered. As stated above, this procedure is also followed for the imaginary wavenumbers. Then, all the calculated roots are plotted on frequency-wavenumber domain graphs.

6.4 Results and discussion

Lamb wave have been used to quantify damage growth and stress relaxation [169-173]. Therefore, We investigated Lamb wave propagation in flat and corrugated aluminum plates both analytically and numerically. First, the dispersion curves for the Rayleigh–Lamb wave modes in a planar waveguide obtained using the proposed generalized approach with $\varepsilon=0$ were compared to those reported previously [168]. Next, the dispersion curves in a planar waveguide as determined using the analytical approach (i.e., by solving Eq. (6-21) while setting $\varepsilon=0$) were compared with the dispersion patterns obtained using the finite element method (FEM). In this study, aluminum, which has a Young's modulus, E, of 72.4 GPa, Poisson's ratio, ν, of 0.33, and density, ρ, of 2780 kg/m^3, was considered. To get a more

general sense of the phenomena of guided Rayleigh–Lamb and SH wave propagation, it is helpful to obtain a nonbiased generalized solution, wherein the axes for the frequency and wavenumber are dimensionless. The SI units for angular frequency and wavenumber are rad/s and 1/m, respectively. Hence, we used $\Omega = fd/c_p$ and $\overline{\mathrm{k}} = kD$ as the dimensionless frequency and wavenumber, respectively. For the guided SH waves, we used $\Omega = fd/c_s$. The wave velocities in the aluminum plate were $c_p = 6212\ m/s$ and $c_s = 3130\ m/s$. The dimensionless frequency axis (Ω) was divided into intervals of 0.1 and was considered to extend till 5 for Rayleigh–Lamb waves and till 10 for SH waves. For example, in the case of $\Omega = fd/c_s$, a Ω value of 1 meant that $f \cong 626\ KHz$ for SH waves in a 5-mm-thick ($2h = d = 5$ mm) aluminum plate. The roots (k), which are the wavenumbers at each normalized frequency, were calculated from the material and geometrical properties using a computer program.

The dispersion curves were plotted by solving the analytically obtained Eq. (6-21) for corrugated plates for different corrugation heights and periodicities. The bandgaps as determined from the analytical solutions were subsequently validated using an FEM model.

6.4.1 Verification and Validation

In Section 6.3, the Rayleigh–Lamb wave dispersion equations for $\varepsilon=0$ were verified analytically through a comparison with the dispersion equations reported in the literature. A pictorial depiction of the verification of the equations for Rayleigh–Lamb and SH waves is given in Figure 6.2, which shows the dispersion curves for Rayleigh–Lamb and SH waves in a planar waveguide as determined using Eq. (6-21) and Eq. (6-23) and $\varepsilon=0$. The dispersion curves reported previously in the literature are also shown. It can be seen that

the dispersion curves obtained using the generalized expression proposed in this study and $\varepsilon=0$ for a planar waveguide are similar to those reported previously. Although the curves for SH waves are also compared in Figure 6.2, in the discussion that follows, we focus only on the Rayleigh–Lamb wave modes in corrugated waveguides.

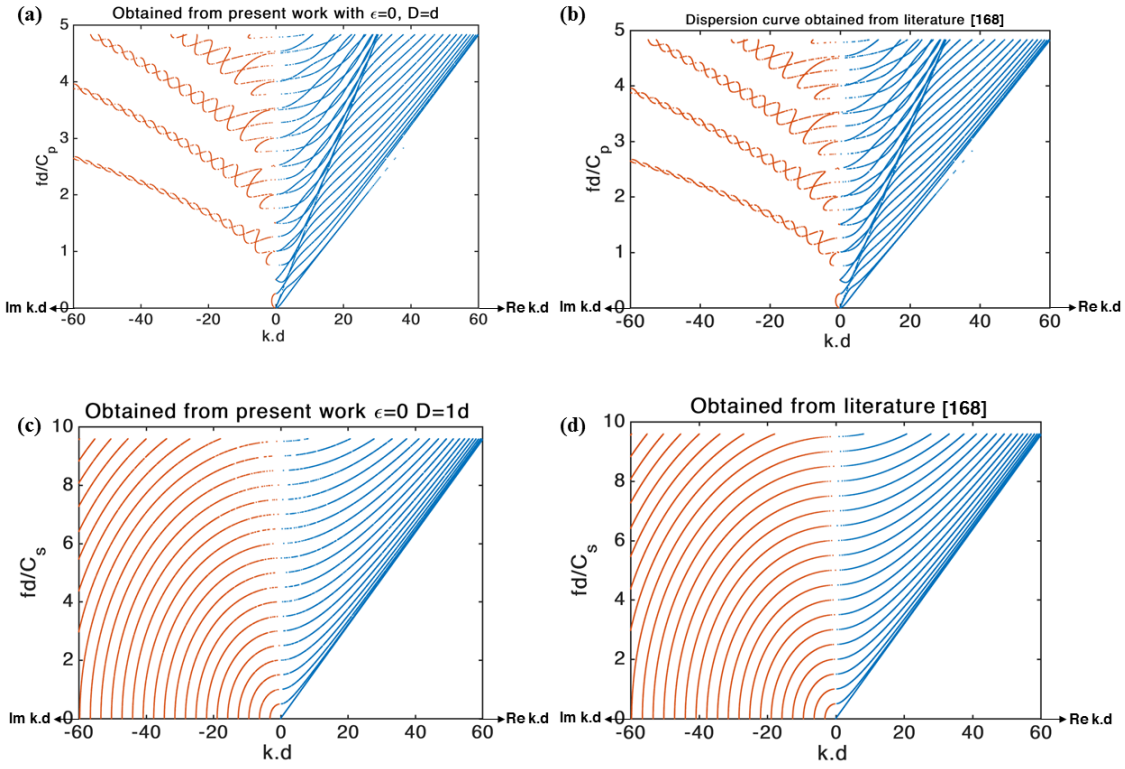

Figure 6.2: Comparison of Lamb wave dispersion curves: (a) those determined in present study and (b) those reported in [168].

To validate the generalized solution given in Eq. (6-21), the dispersion behavior in a planar waveguide was simulated using a FEM model, and the results were compared with the dispersion curves obtained from the generalized analytical solution. The multiphysics software COMSOL was used to simulate the propagation of a Rayleigh–Lamb wave in a planar waveguide. A planar waveguide ($\varepsilon = 0$) with a length of 100 mm was excited with a chirp signal with frequencies in the range of 100 kHz to 1 MHz. Figure 6.3 shows the process of determining the dispersion curve for the planar waveguide using the FEM

model. Stress-free boundary conditions were imposed on the upper and lower surfaces of the waveguide. Further, perfectly matched layer boundary conditions were applied at the start and end of the plate. Next, the planar waveguide was excited with a chirp signal, and the displacements of 250 points were determined in the time domain. The measurement points were distributed uniformly on the central axis such that the distance between each point was 0.4 mm. Ensuring that spatial and temporal discretization is performed correctly is essential for the convergence of the solution during wave propagation simulations. The maximum spatial (Δx) and temporal (Δt) discretization levels for meeting the convergence criteria were calculated from the expressions $\Delta x = \lambda_{\min}/10$ and $\Delta t = \Delta x / C_{\max}\sqrt{3}$, where $\lambda_{\min}$ is the minimum wavelength of the Lamb wave modes and $C_{\max}$ is the maximum phase velocity of the wave propagation modes [174]. The mesh size (0.4 mm) and time step (2×10^{-8} s) were calculated based on [174]. Linear triangular elements were used in the FEM simulation, and a total of 10122 elements were employed. The displacements along the central line of the plate were determined, and the spatiotemporal displacement field was plotted, as shown in Figure 6.3. Next, the two-dimensional (2D) fast Fourier transform (FFT) was used to determine the frequency-wavenumber domain plot (Figure 6.3).

To elucidate the numerically determined dispersion behavior from the FEM simulation results, the frequency-wavenumber plot was superimposed on the analytically obtained dispersion curve for a planar waveguide, as shown in Figure 6.4. Since the excitation signal was considered to be symmetric in this study, the antisymmetric modes were not prominent in the frequency-wavenumber plot obtained from the FEM simulation. However, the symmetric modes were in good agreement, as shown in Figure 6.4.

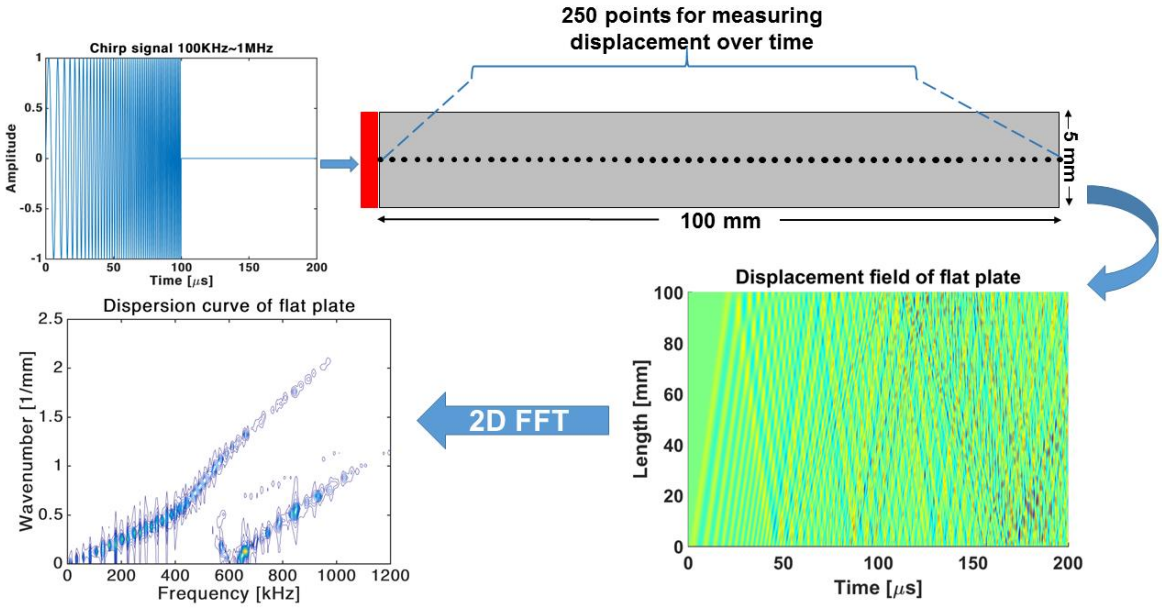

Figure 6.3: Process for obtaining dispersion curve for planar waveguide using finite element method.

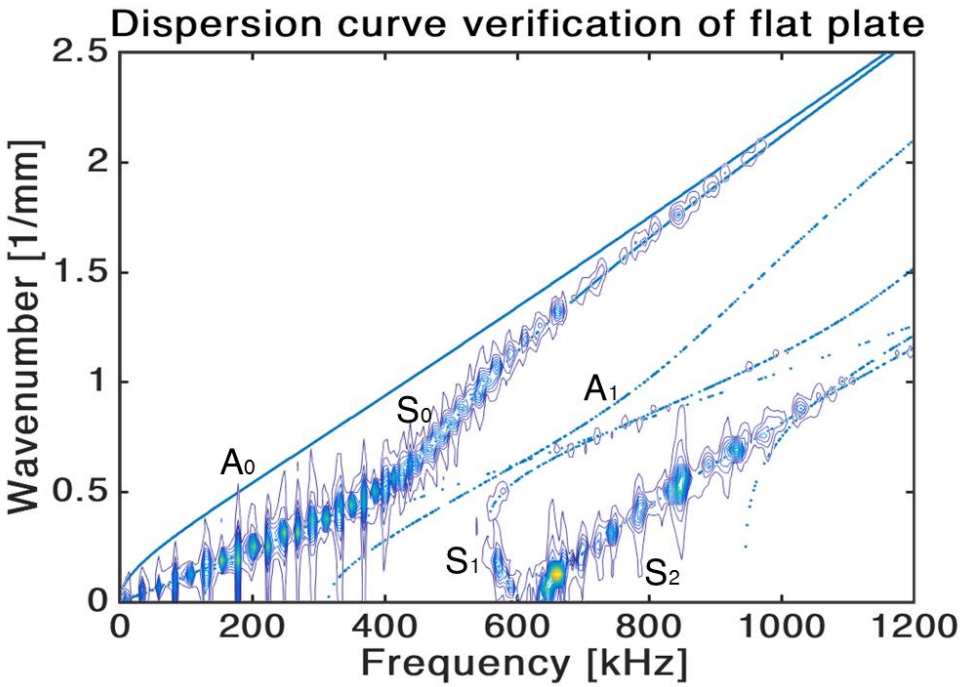

Figure 6.4: Comparison of dispersion curves for planar waveguide as determined by finite element method and obtained from analytical solution.

Next, both symmetric and antisymmetric Rayleigh–Lamb solutions were obtained for corrugated waveguides with different periodicities and corrugation heights.

The dispersion curves for a planar waveguide were compared with those for wave dispersion in a corrugated waveguide with a degree of corrugation, ε, of *0.5h* and periodicity, *D*, of *3d* (see Figure 6.5). The fabricated dimensionless variable $\bar{k}$ ($k.D$) was assumed to be either real or purely imaginary. As is apparent from Figure 6.5, the corrugated waveguide exhibited several mode conversions in the real-$\bar{k}$ domain. Corrugated waveguides can exhibit additional modes in the evanescent zone (imaginary $\bar{k}$) that are not present in planar waveguides because of the corrugation [175]. Given this context, the two red boxed areas in Figure 6.4(b) are shown separately in Figure 6.4(c) and Figure 6.4(d). These areas were identified as the mode conversion zones for the corrugated waveguide. Based on a subsequent analysis, it was found that the mode conversion zones in the frequency-wavenumber plots for corrugated waveguides decreases and becomes more collimated with an increase in the depth of corrugation.

A unique feature of these zones is that, for a specific wavenumber and a specific wave mode, multiple frequency solutions (up to three) can exist.

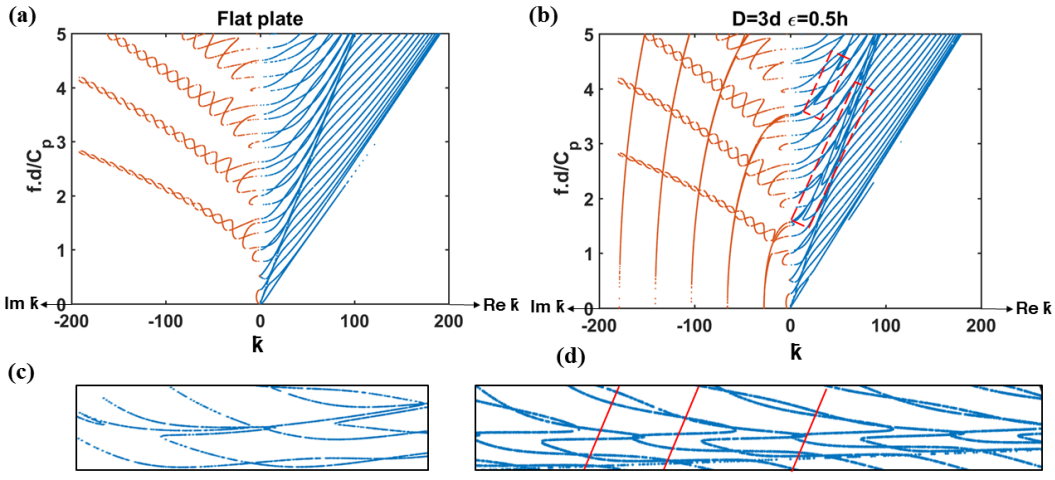

Figure 6.5: Dispersion curve for (a) planar waveguide and (b) corrugated plate

This makes a specific mode to demonstrate wave propagation with both positive and negatively group velocities at a certain wavenumber. Such zones and such modes can be studied separately to understand the unique wave transport phenomenon. However, this was not the objective of the present study.

6.4.2 Parametric Study

Next, we investigated the effects of the corrugation height on the Rayleigh–Lamb modes. As depicted in Figure 6.6, the dispersion curves for $\varepsilon = 0.1h$, $\varepsilon = 0.2h$, $\varepsilon = 0.3h$, and $\varepsilon = 0.5h$ were plotted while keeping the periodicity ($D = 2d$) fixed.

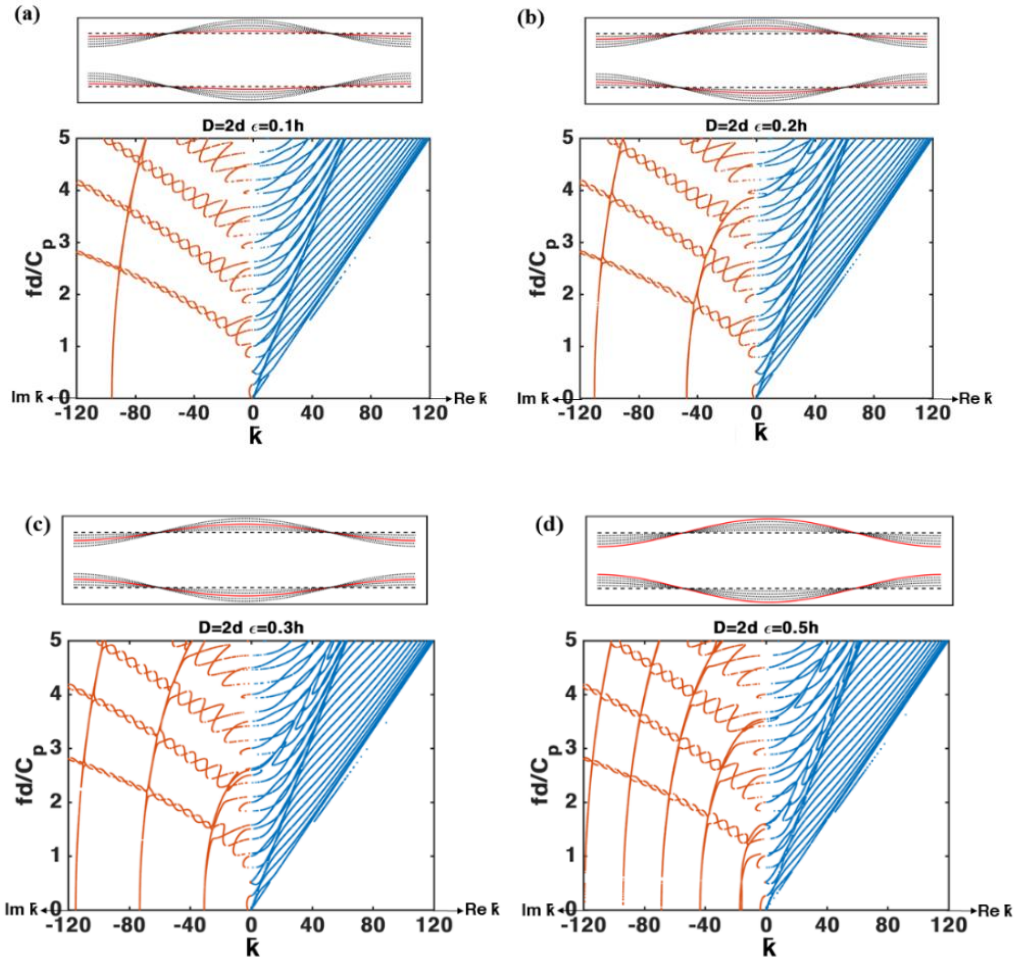

Figure 6.6: Effects of corrugation height on Lamb wave propagation.

As can be seen from the figure, additional evanescent modes were generated with an increase in the corrugation height. Further, the number of additional modes increased with an increase in the depth of corrugation. Finally, with an increase in the depth of corrugation, the mode conversion zones became narrower.

Next, the effects of periodicity on the dispersion curves were studied while keeping the corrugation height constant.

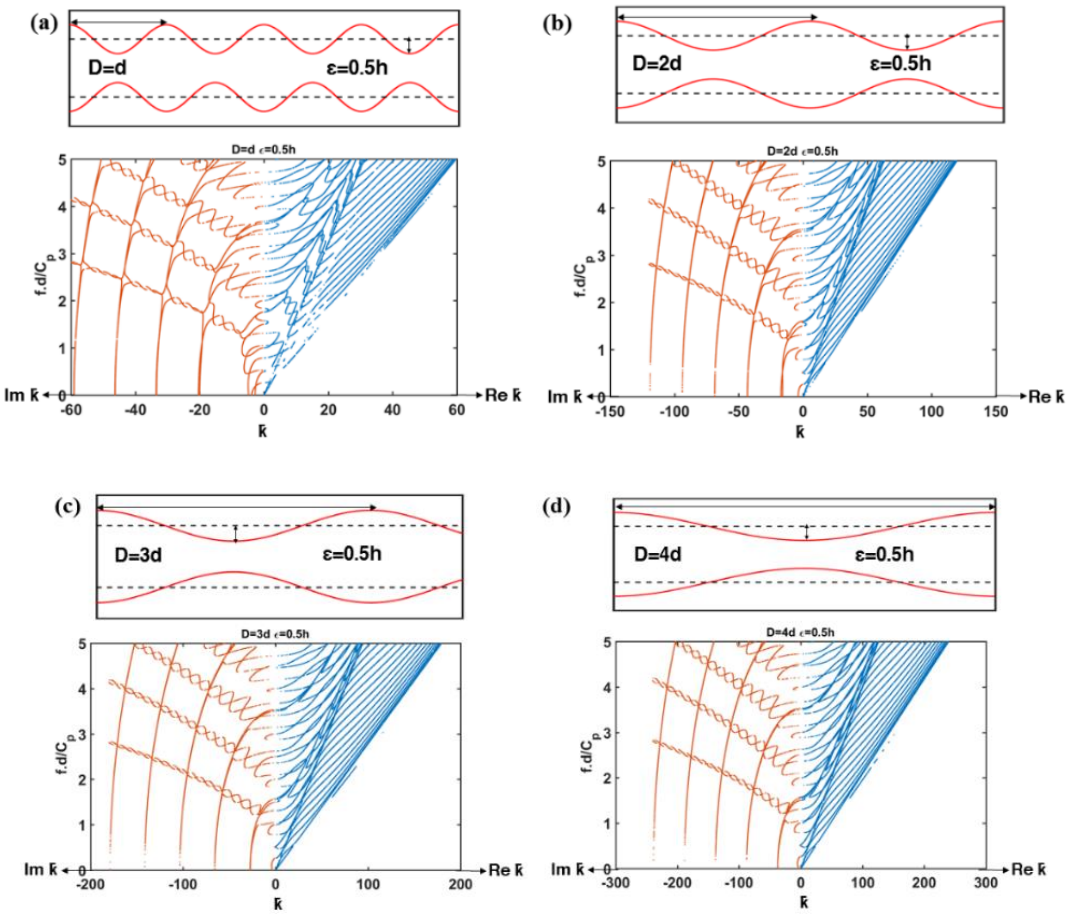

Figure 6.7: Effects of periodicity length on Lamb wave propagation.

Figure 6.7 shows Rayleigh–Lamb wave propagation in corrugated waveguides with different periodicities (*D=d*, *D=2d*, *D=3d*, and *D=4d*) and a corrugation height, ε, of $0.5h$. The number of solution spaces for the corrugated waveguide with D=d (Figure 6.7(a)) in

the frequency-wavenumber domain was the lowest. Further, with an increase in the periodicity, the range of the wavenumber solutions increased for certain frequencies.

6.4.3 Bandgap study

In order to determine the bandgaps of corrugated waveguides, their dispersion curves must be analyzed. According to the Bloch theorem, all possible solutions for the wavenumber vector (k) can be obtained by adding a factor, $2\pi n/D$, to the fundamental wavenumber, where $n = 0, \pm1, \pm2, \pm3$. In the present study, the solutions were restricted to the first Brillouin zone [164, 176, 177]. The propagation of an elastic wave along the ΓX direction of the irreducible Brillouin zone for which $0 < Re(k) < \frac{\pi}{D}$ [178] was considered. All the bandgaps in the corrugated waveguide were determined for $0 < Re(k.D = \bar{k}) < \pi$ for the frequency range of 0 to 3 MHz.

To understand the effects of the waveguide parameters (periodicity and corrugation height) on the bandgaps, a parametric study was performed for different configurations of the corrugated waveguide. The equations for the dispersion relationships were solved for different periodicities (*D=d*, *D=2d*, *D=3d*, *D=4d*, *D=5d*, and *D=6d*) and different corrugation heights (*ε=0.1h*, *ε=0.15h*, *ε=0.2h*, *ε=0.25h*, *ε=0.3h*, *ε=0.35h*, *ε=0.4h*, *ε=0.45h*, and *ε=0.5h*). Next, the bandgaps were determined for each corrugated waveguide. Corrugated waveguides with a certain periodicity and corrugation height exhibit multiple bandgaps. Each bandgap has its own upper and lower frequency limit. To study the influence of the corrugation height and corrugation periodicity on the bandgaps, based on the upper and lower frequency limits, six bandgap plots were created while varying the corrugation factor, e, from 0.1 to 0.5; these are shown in Figure 6.8, which was obtained

by connecting the lower and higher frequency limits of the first, second, third, and fourth bandgap zones for corrugated waveguides with the same periodicity but different corrugation heights.

It can be seen that there are four bandgaps in the corrugated plates with D=d. However, the number of bandgaps in the waveguides with D=2d is three. Moreover, once the periodicity was changed from D=3d to D=6d, the bandgap zones merged. Thus, increasing the periodicity can affect the number of bandgaps in a waveguide. Here, the normalized wavenumber ($\bar{k} = k.D$) was limited to range from 0 to π within the first Brillouin Zone. However, when the periodicity was increased, the wavenumber decreased to be in the range of 0 to π. Consequently, at a certain frequency, the number of existing wavenumber solutions decreased for the corrugated plates with low periodicities as compared to that for corrugated plates with higher periodicities. Therefore, the number of bandgaps decreased with the increase in the periodicity.

To verify the bandgaps in corrugated waveguides and determine whether they could be predicted correctly using the proposed generalized Rayleigh–Lamb equations, FEM simulations were performed to determine the dispersion curves and bandgaps for corrugated plates with two different configurations (i.e., those marked in Figs. 8(a) and (b)). The plates with D=d and ε=0.25h and D=2d and ε=0.3h were used to verify the bandgaps obtained from an analytical solution. Figure 6.9 shows the process for determining the dispersion behavior in a corrugated waveguide (D=d and ε=0.25h). As depicted in Figs. 8(a) and (b), two bandgap zones were present in the sheet with D=d and ε=0.25h whereas three bandgap zones were present in the sheet with D=2d and ε=0.3h.

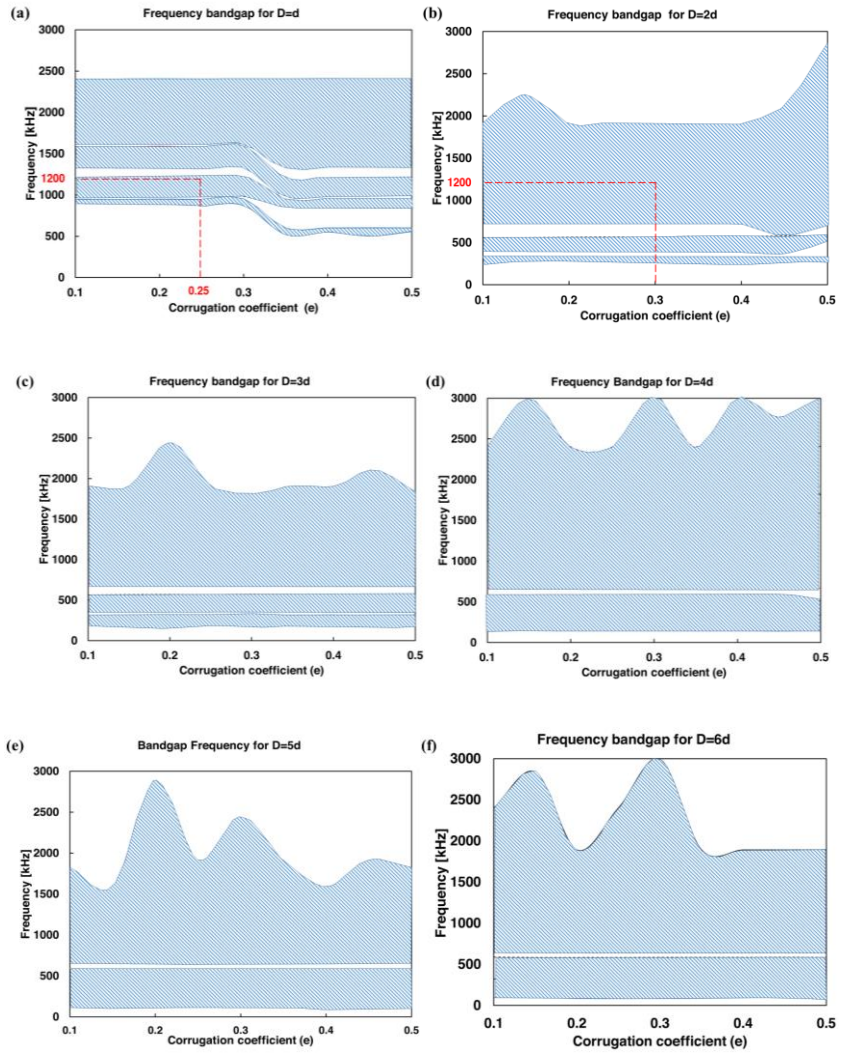

Figure 6.8: Frequency bandgaps for different configurations of corrugated plates.

In this case too, the corrugated waveguide was excited using a chirp signal with frequencies of 100 kHz to 1 MHz. Further, the time step and mesh size used were like those employed for the planar waveguide simulation, whose results are shown in Figure 6.3. The process for determining the dispersion curve was similar to that used for the planar waveguide. The dispersion curve was obtained by using the 2D FFT on the displacement filed in the time-space domain. As can be seen from Figure 6.9, symmetric modes were observed during the simulation.

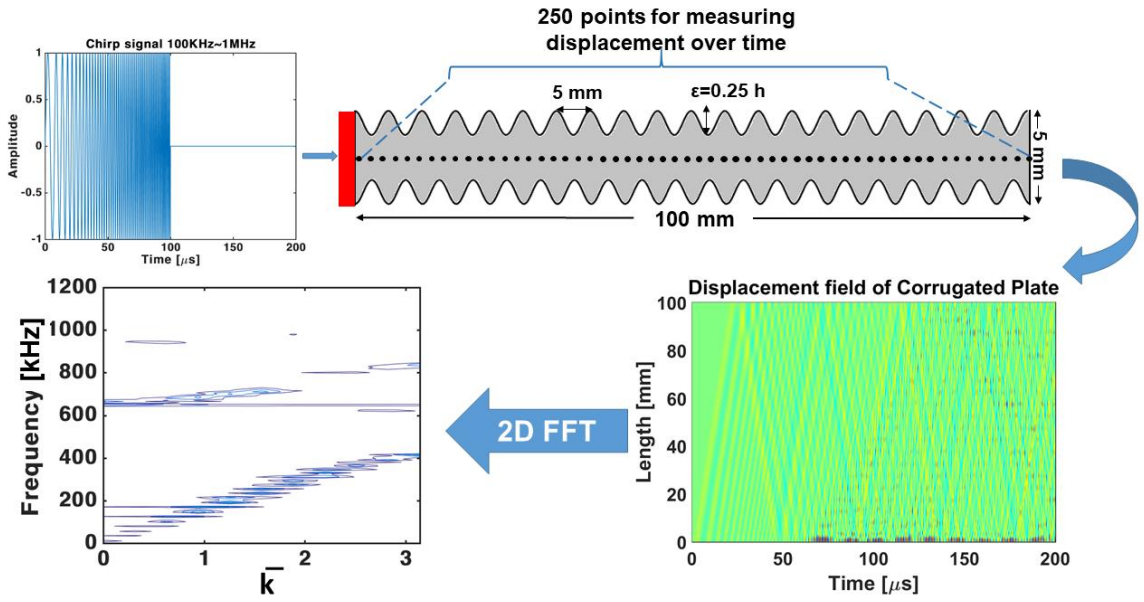

Figure 6.9: Process for determining dispersion curve for corrugated waveguide using finite element method.

Next, the dispersion curve obtained from the analytical solution was compared with that from the FEM simulation. As shown in Figure 6.10, the FEM simulation results confirmed the bandgap zones, which could be superimposed on the bandgaps obtained from the analytical solution.

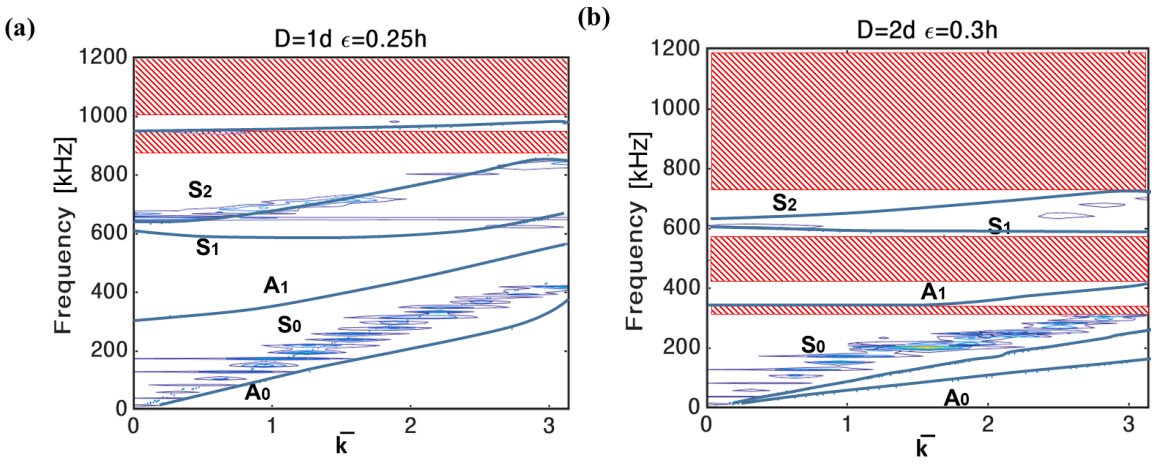

Figure 6.10: Verification of bandgap zones for two configurations of corrugated plates.

6.5 Conclusions

In this study, we developed a generalized expression for Rayleigh–Lamb wave modes in planar and corrugated waveguides. To derive the dispersion relationships, the Bloch theorem was directly applied to the scalar and vector wave potentials in order to obtain the governing equations. By applying the appropriate boundary conditions, we could obtain the dispersion relationships. Next, using a root-finding algorithm, the equations corresponding to the dispersion relationships were solved, and the dispersion curves were obtained for both planar and corrugated waveguides. To investigate the effects of corrugation on the corrugated waveguides, a parametric study was performed. Parameters such as the corrugation depth and length of periodicity were varied, and their effects on the dispersion curves and bandgaps were explored. The obtained results were verified through FEM simulations. The planar and corrugated waveguides were simulated using the multiphysics software COMSOL. A chirp signal was employed to excite the plates, and it was found that, for a fixed $\bar{k}$, the bandgaps may merge with an increase in the periodicity. Further, for a fixed periodicity, changes in the corrugation depth may result in additional modes owing to the resulting changed in the boundary conditions. The generalized expression was validated with satisfactory results.

REFERENCES

[1] P. Balakrishnan, M. J. John, L. Pothen, M. Sreekala, and S. Thomas, "Natural fibre and polymer matrix composites and their applications in aerospace engineering," in *Advanced composite materials for aerospace engineering*: Elsevier, 2016, pp. 365-383.

[2] D. Gay, *Composite materials: design and applications*. CRC press, 2014.

[3] P. Irving and C. Soutis, *Polymer composites in the aerospace industry* (no. 50). Elsevier, 2014.

[4] P. Mangalgiri, "Composite materials for aerospace applications," *Bulletin of Materials Science,* vol. 22, no. 3, pp. 657-664, 1999.

[5] F. M. Al-Oqla and S. Sapuan, "Natural fiber reinforced polymer composites in industrial applications: feasibility of date palm fibers for sustainable automotive industry," *Journal of Cleaner Production,* vol. 66, pp. 347-354, 2014.

[6] V. Roubicek, H. Raclavska, D. Juchelkova, and P. Filip, "Wear and environmental aspects of composite materials for automotive braking industry," *Wear,* vol. 265, no. 1-2, pp. 167-175, 2008.

[7] A. Ashori, "Wood–plastic composites as promising green-composites for automotive industries!," *Bioresource technology,* vol. 99, no. 11, pp. 4661-4667, 2008.

[8] E. Asmatulu, J. Twomey, and M. Overcash, "Recycling of fiber-reinforced composites and direct structural composite recycling concept," *Journal of Composite Materials,* vol. 48, no. 5, pp. 593-608, 2014.

[9] C. Clemons, "Wood-plastic composites in the United States: The interfacing of two industries," *Forest products journal. Vol. 52, no. 6 (June 2002): Pages 10-18,* 2002.

[10] A. Conroy, S. Halliwell, and T. Reynolds, "Composite recycling in the construction industry," *Composites Part A: Applied Science and Manufacturing,* vol. 37, no. 8, pp. 1216-1222, 2006.

[11] A. Quilter, "Composites in aerospace applications," *IHS White Paper*, vol. 444, no. 1, 2001.

[12] (29 September 2015). *IMAST - Technological district on Engineering of polymeric and composite materials and structures*. Available: http://www.match-a4m.eu/index.php/latest/news/129-imast

[13] J. Bell, "Condition based maintenance plus DoD guidebook," *Department of Defense: Washington, DC, USA*, 2008.

[14] A. J. Hall *et al.*, "Damage precursor investigation of fiber-reinforced composite materials under fatigue loads," ARMY RESEARCH LAB ABERDEEN PROVING GROUND MD VEHICLE TECHNOLOGY DIRECTORATE2013.

[15] V. Weiss and A. Ghoshal, "On the search for optimal damage precursors," *Structural Health Monitoring*, vol. 13, no. 6, pp. 601-608, 2014.

[16] E. Rabiei, E. L. Droguett, and M. Modarres, "A prognostics approach based on the evolution of damage precursors using dynamic Bayesian networks," *Advances in Mechanical Engineering*, vol. 8, no. 9, p. 1687814016666747, 2016.

[17] X.-W. Jiang, H. Wang, and S. Guo, "Peridynamic Open-Hole Tensile Strength Prediction of Fiber-Reinforced Composite Laminate Using Energy-Based Failure Criteria," *Advances in Materials Science and Engineering*, vol. 2019, 2019.

[18] X.-W. Jiang and H. Wang, "Ordinary state-based peridynamics for open-hole tensile strength prediction of fiber-reinforced composite laminates," *Journal of Mechanics of Materials and Structures*, vol. 13, no. 1, pp. 53-82, 2018.

[19] E. Dan-Jumbo, R. Keller, W. S. Chan, and S. Selvaraj, "Strength of composite laminate with multiple holes," *Proceedings of the The The Boeing Company*, 2015.

[20] X. Chao, L. Qi, J. Cheng, W. Tian, S. Zhang, and H. Li, "Numerical evaluation of the effect of pores on effective elastic properties of carbon/carbon composites," *Composite Structures*, vol. 196, pp. 108-116, 2018.

[21] M. Saadatzi, F. Mir, M. N. Saadatzi, V. Tavaf, and S. Banerjee, "Modeling of a 3D acoustoelastic metamaterial energy harvester," in *Active and Passive Smart Structures and Integrated Systems XII*, 2018, vol. 10595, p. 105952U: International Society for Optics and Photonics.

[22] F. Mir, M. Saadatzi, R. U. Ahmed, and S. Banerjee, "Acoustoelastic MetaWall noise barriers for industrial application with simultaneous energy harvesting capability," *Applied Acoustics*, vol. 139, pp. 282-292, 2018.

[23] M. Saadatzi, F. Mir, M. N. Saadatzi, and S. Banerjee, "Modeling and Fabrication of a Multi-axial Piezoelectric Energy Harvester based on a Metamaterial-inspired Structure," *IEEE Sensors Journal*, vol. 18, no. 22, pp. 9410-9419, 2018.

[24] M. Saadatzi, M. N. Saadatzi, V. Tavaf, and S. Banerjee, "Development of a PVDF based artificial basilar membrane," in *Bioinspiration, Biomimetics, and Bioreplication VIII*, 2018, vol. 10593, p. 1059318: International Society for Optics and Photonics.

[25] M. Khan, P. Sultana, M. S. Sadatzi, M. Tahiyat, T. Farouk, and S. Banerjee, "Enhancement of piezoelectric properties of nanofibers and nanocomposite membranes through corona treatment," *Bulletin of the American Physical Society*, 2019.

[26] V. Tavaf, M. Saadatzi, S. Shrestha, and S. Banerjee, "Effect of multiscale precursor damage on wave propagation through modulated constitutive properties of composite materials," in *Health Monitoring of Structural and Biological Systems XII*, 2018, vol. 10600, p. 106001N: International Society for Optics and Photonics.

[27] M. Saadatzi, M. N. Saadatzi, V. Tavaf, and S. Banerjee, "AEVE 3D: Acousto Electrodynamic 3-Dimensional Vibration Exciter for Engineering Testing," *IEEE/ASME Transactions on Mechatronics*, 2018.

[28] M. Saadatzi, M. N. Saadatzi, R. Ahmed, and S. Banerjee, "An electro-dynamic 3-dimensional vibration test bed for engineering testing," in *Industrial and Commercial Applications of Smart Structures Technologies 2017*, 2017, vol. 10166, p. 101660D: International Society for Optics and Photonics.

[29] F. Mir, M. S. Saadatzi, R. U. Ahmed, and S. Banerjee, "The possibility of harvesting electrical energy from industrial noise barriers using meta-wall bricks," in *Sensors and Smart Structures Technologies for Civil, Mechanical, and Aerospace Systems 2018*, 2018, vol. 10598, p. 105982S: International Society for Optics and Photonics.

[30] M. Goodarzi, M. N. Bahrami, and V. Tavaf, "Refined plate theory for free vibration analysis of FG nanoplates using the nonlocal continuum plate model," *Journal of Computational Applied Mechanics*, vol. 48, no. 1, pp. 123-136, 2017.

[31] H. Ahmed, R. Ahmed, M. M. Indaleeb, and S. Banerjee, "Multifunction acoustic modulation by a multi-mode acoustic metamaterial architecture," *Journal of Physics Communications*, vol. 2, no. 11, p. 115001, 2018.

[32] M. M. Indaleeb, S. Banerjee, H. Ahmed, M. Saadatzi, and R. Ahmed, "Deaf band based engineered Dirac cone in a periodic acoustic metamaterial: A numerical and experimental study," *Physical Review B*, vol. 99, no. 2, 2019.

[33] S. Patra, H. Ahmed, and S. Banerjee, "Peri-Elastodynamic Simulations of Guided Ultrasonic Waves in Plate-Like Structure with Surface Mounted PZT," *Sensors (Basel)*, vol. 18, no. 1, Jan 18 2018.

[34] M. Indaleeb, H. Ahmed, and S. Banerjee, "Investigation on multi-occurrence of Dirac cone and exceptional ring (Conference Presentation)," in *Health Monitoring of Structural and Biological Systems XII*, 2018, vol. 10600, p. 106001U: International Society for Optics and Photonics.

[35] A. Van Pamel, G. Sha, S. Rokhlin, and M. Lowe, "Finite-element modelling of elastic wave propagation and scattering within heterogeneous media," *Proceedings of the Royal Society A: Mathematical, Physical and Engineering Sciences*, vol. 473, no. 2197, p. 20160738, 2017.

[36] S. Moradi and V. Tavaf, "Crack detection in circular cylindrical shells using differential quadrature method," *International Journal of Pressure Vessels and Piping*, vol. 111, pp. 209-216, 2013.

[37] M. Saadatzi, M. N. Saadatzi, V. Tavaf, and S. Banerjee, "Finite element analysis of smart structural implications of a beam-type artificial basilar membrane inspired sensor," in *Bioinspiration, Biomimetics, and Bioreplication IX*, 2019, vol. 10965, p. 109650S: International Society for Optics and Photonics.

[38] J. L. Rose, "Boundary element modeling for defect characterization potential in a wave guide," *International Journal of Solids and Structures*, vol. 40, no. 11, pp. 2645-2658, 2003.

[39] M. Bouchon and F. J. Sánchez-Sesma, "Boundary integral equations and boundary elements methods in elastodynamics," *Advances in geophysics*, vol. 48, pp. 157-189, 2007.

[40] M. G. Imhof, "Computing the elastic scattering from inclusions using the multiple multipoles method in three dimensions," *Geophysical Journal International*, vol. 156, no. 2, pp. 287-296, 2004.

[41] R. T. Schulte and C. P. Fritzen, "Modelling of Wave-Based SHM Systems Using the Spectral Element Method," *PAMM*, vol. 10, no. 1, pp. 15-18, 2010.

[42] Y. Shen and C. E. Cesnik, "Modeling of nonlinear interactions between guided waves and fatigue cracks using local interaction simulation approach," *Ultrasonics*, vol. 74, pp. 106-123, 2017.

[43] S. Banerjee, S. Das, T. Kundu, and D. Placko, "Controlled Space Radiation concept for mesh-free semi-analytical technique to model wave fields in complex geometries," *Ultrasonics*, vol. 49, no. 8, pp. 615-622, 2009.

[44] E. K. Rahani and T. Kundu, "Gaussian-DPSM (G-DPSM) and Element Source Method (ESM) modifications to DPSM for ultrasonic field modeling," *Ultrasonics*, vol. 51, no. 5, pp. 625-631, 2011.

[45] P. Suquet, "Elements of homogenization for inelastic solid mechanics," *Homogenization techniques for composite media*, vol. 272, pp. 193-278, 1987.

[46] N. Bakhvalov and G. Panasenko, "Homogenisation: averaging processes in periodic media: mathematical problems in the mechanics of composite materials. 1989," ed: Springer.

[47] C. Sun and R. Vaidya, "Prediction of composite properties from a representative volume element," *Composites Science and Technology*, vol. 56, no. 2, pp. 171-179, 1996.

[48] J. Michel, H. Moulinec, and P. Suquet, "Effective properties of composite materials with periodic microstructure: a computational approach," *Computer methods in applied mechanics and engineering*, vol. 172, no. 1, pp. 109-143, 1999.

[49] S. Li, "General unit cells for micromechanical analyses of unidirectional composites," *Composites Part A: applied science and manufacturing*, vol. 32, no. 6, pp. 815-826, 2001.

[50] E. Lenglet, A.-C. Hladky-Hennion, and J.-C. Debus, "Numerical homogenization techniques applied to piezoelectric composites," *The Journal of the Acoustical Society of America,* vol. 113, no. 2, pp. 826-833, 2003.

[51] H. Berger *et al.*, "Finite element and asymptotic homogenization methods applied to smart composite materials," *Computational mechanics,* vol. 33, no. 1, pp. 61-67, 2003.

[52] H. Berger *et al.*, "An analytical and numerical approach for calculating effective material coefficients of piezoelectric fiber composites," *International Journal of Solids and Structures,* vol. 42, no. 21, pp. 5692-5714, 2005.

[53] H. Berger, S. Kari, U. Gabbert, R. Rodríguez-Ramos, J. Bravo-Castillero, and R. Guinovart-Díaz, "A comprehensive numerical homogenisation technique for calculating effective coefficients of uniaxial piezoelectric fiber composites," *Materials Science and Engineering: A,* vol. 412, no. 1, pp. 53-60, 2005.

[54] H. Berger *et al.*, "Unit cell models of piezoelectric fiber composites for numerical and analytical calculation of effective properties," *Smart Materials and Structures,* vol. 15, no. 2, pp. 451-458, 2006.

[55] S. Kari, H. Berger, R. Rodriguez-Ramos, and U. Gabbert, "Computational evaluation of effective material properties of composites reinforced by randomly distributed spherical particles," *Composite Structures,* vol. 77, no. 2, pp. 223-231, 2007.

[56] H. Berger, U. Gabbert, R. Rodriguez-Ramos, J. Bravo-Castillero, and R. Guinovart-Diaz, "A numerical homogenization technique for piezoelectric composites with arbitrary fiber distribution," presented at the 11th Pan-American Congress of Applied Mechanics, Foz do Iguaçu, PR, Brazil, 2010.

[57] M. E. Moreno, V. Tita, and F. D. Marques, "Finite element analysis applied to evaluation of effective material coefficients for piezoelectric fiber composites," in *Brazilian Symposium on Aerospace Eng. & Applications*, S. J. Campos, SP, Brazil, 2009.

[58] M. E. Moreno, V. Tita, and F. D. Marques, "Influence of boundary conditions on the determination of effective material properties for active fiber composites," in

11th Pan-American Congress of Applied Mechanics, January, ed. Foz do lguacu, PR, Brazil, 2010, pp. 04-08.

[59] R. d. Medeiros, M. E. Moreno, F. D. Marques, and V. Tita, "Effective properties evaluation for smart composite materials," *Journal of the Brazilian Society of Mechanical Sciences and Engineering,* vol. 34, no. SPE, pp. 362-370, 2012.

[60] R.-S. Qin, Y. Xiao, and H. Lan, "Numerical simulation of effective properties of 3d piezoelectric composites," *Journal of Engineering,* vol. 2014, 2014.

[61] A. R. Maligno, "Finite element investigations on the microstructure of composite materials," University of Nottingham, 2008.

[62] P. Bhaskar and R. H. Mohamed, "Analytical estimation of elastic properties of polypropylene fiber matrix composite by finite element analysis," *Advances in Materials Physics and Chemistry,* vol. 2, pp. 23-30, 2012.

[63] S. Banerjee and B. V. Sankar, "Mechanical properties of hybrid composites using finite element method based micromechanics," *Composites Part B: Engineering,* vol. 58, pp. 318-327, 2014.

[64] S. B. R. Devireddy and S. Biswas, "Effect of fiber geometry and representative volume element on elastic and thermal properties of unidirectional fiber-reinforced composites," *Journal of Composites,* vol. 2014, pp. 1-12, 2014.

[65] G. Soni, R. Singh, M. Mitra, and B. G. Falzon, "Modelling matrix damage and fibre–matrix interfacial decohesion in composite laminates via a multi-fibre multi-layer representative volume element (M 2 RVE)," *International Journal of Solids and Structures,* vol. 51, no. 2, pp. 449-461, 2014.

[66] G. Catalanotti, "On the generation of RVE-based models of composites reinforced with long fibres or spherical particles," *Composite Structures,* vol. 138, pp. 84-95, 2016.

[67] S. Swaminathan, S. Ghosh, and N. Pagano, "Statistically equivalent representative volume elements for unidirectional composite microstructures: Part I-Without damage," *Journal of Composite Materials,* vol. 40, no. 7, pp. 583-604, 2006.

[68] J. Lambert, A. Chambers, I. Sinclair, and S. Spearing, "3D damage characterisation and the role of voids in the fatigue of wind turbine blade materials," *Composites Science and Technology,* vol. 72, no. 2, pp. 337-343, 2012.

[69] V. Tavaf, M. Saadatzi, and S. Banerjee, "Effect of void sizes on effective material properties of unidirectional composite materials," in *Health Monitoring of Structural and Biological Systems XIII*, 2019, vol. 10972, p. 109722K: International Society for Optics and Photonics.

[70] V. Tavaf, M. Saadatzi, and S. Banerjee, "Quantification of degraded constitutive coefficients of composites in the presence of distributed defects," *Journal of Composite Materials*, p. 0021998319832351, 2019.

[71] V. Tavaf, M. Saadatzi, S. Shrestha, and S. Banerjee, "Quantification of material degradation and its behavior of elastodynamic Green's function for computational wave field modeling in composites," *Materials Today Communications*, vol. 17, pp. 402-412, 2018.

[72] S. F. M. de Almeida and Z. d. S. N. Neto, "Effect of void content on the strength of composite laminates," *Composite structures*, vol. 28, no. 2, pp. 139-148, 1994.

[73] S. Lee, S. Jeng, and J.-M. Yang, "Modeling and simulation of the effect of fiber breakage on creep behavior of fiber-reinforced metal matrix composites," *Mechanics of materials*, vol. 21, no. 4, pp. 303-312, 1995.

[74] G. Anlas, M. H. Santare, and I. W. Hall, "Modeling the effect of fiber breakage on the elastic properties of short-fiber composites," *Composites science and technology*, vol. 54, no. 2, pp. 113-122, 1995.

[75] B. G. Kumar, R. P. Singh, and T. Nakamura, "Degradation of carbon fiber-reinforced epoxy composites by ultraviolet radiation and condensation," *Journal of Composite Materials*, vol. 36, no. 24, pp. 2713-2733, 2002.

[76] S. Swaminathan and S. Ghosh, "Statistically equivalent representative volume elements for unidirectional composite microstructures: Part ii-with interfacial debonding," *Journal of Composite Materials*, vol. 40, no. 7, pp. 605-621, 2006.

[77] B. Li, B. Wang, and S. R. Reid, "Effective elastic properties of randomly distributed void models for porous materials," *International Journal of Mechanical Sciences*, vol. 52, no. 5, pp. 726-732, 2010.

[78] G. Srinivasulu, R. Velmurugan, and S. Jayasankar, "Influence of void microstructure on the effective elastic properties of discontinuous fiber-reinforced composites," *Journal of Composite Materials*, vol. 49, no. 22, pp. 2745-2755, 2015.

[79] C. Dong, "Effects of process-induced voids on the properties of fibre reinforced composites," *Journal of Materials Science & Technology*, vol. 32, no. 7, pp. 597-604, 2016.

[80] E. Patterson, D. Backman, and G. Cloud, *Composite Materials and Joining Technologies for Composites, Volume 7: Proceedings of the 2012 Annual Conference on Experimental and Applied Mechanics*. Springer Science & Business Media, 2012.

[81] J. Matuszewski, "Fastener guidelines for composite materials," *Materials Technology*, vol. 19, no. 4, pp. 203-210, 2004.

[82] S. Dehghanpour, K. H. Safari, F. Barati, and M. Attar, "Stress concentration around of pin-loaded hole in unidirectional multi-layered metallic matrix composite material," *Journal of Mechanical Science and Technology*, pp. 1-8, 2019.

[83] B. R. Sankar and P. Umamaheswarrao, "Investigations on the surface roughness of drilled hole on carbon fiber reinforced plastic composite," *Trends in industrial and mechanical engineering. New Delhi, India: Excellent Publishing House*, pp. 113-119, 2016.

[84] L. Toubal, M. Karama, and B. Lorrain, "Stress concentration in a circular hole in composite plate," *Composite structures*, vol. 68, no. 1, pp. 31-36, 2005.

[85] A. Khechai, A. Tati, and A. Guettala, "Finite element analysis of stress concentrations and failure criteria in composite plates with circular holes," *Frontiers of Mechanical Engineering*, vol. 9, no. 3, pp. 281-294, 2014.

[86] M. Abir, T. Tay, M. Ridha, and H. Lee, "Modelling damage growth in composites subjected to impact and compression after impact," *Composite Structures*, vol. 168, pp. 13-25, 2017.

[87] S. Xin and H. Wen, "A progressive damage model for fiber reinforced plastic composites subjected to impact loading," *International journal of impact engineering*, vol. 75, pp. 40-52, 2015.

[88] R. Seifi, O. Ghadimian, and M. Ranjbaran, "Study on life and path of fatigue cracks in multiple site damage plates," *International Journal of Fatigue*, vol. 80, pp. 449-458, 2015.

[89] R. Galatolo and R. Lazzeri, "Experiments and model predictions for fatigue crack propagation in riveted lap-joints with multiple site damage," *Fatigue & Fracture of Engineering Materials & Structures,* vol. 39, no. 3, pp. 307-319, 2016.

[90] J. M. Whitney and R. Nuismer, "Stress fracture criteria for laminated composites containing stress concentrations," *Journal of composite materials,* vol. 8, no. 3, pp. 253-265, 1974.

[91] I. Eriksson and C.-G. Aronsson, "Strength of tensile loaded graphite/epoxy laminates containing cracks, open and filled holes," *Journal of composite materials,* vol. 24, no. 5, pp. 456-482, 1990.

[92] W. Liu, X. Chang, X. Zhang, and Y. Zhang, "Progressive damage analysis of carbon/epoxy laminates under couple laser and mechanical loading," *Results in physics,* vol. 7, pp. 995-1005, 2017.

[93] S. C. Tan and J. Perez, "Progressive failure of laminated composites with a hole under compressive loading," *Journal of Reinforced Plastics and Composites,* vol. 12, no. 10, pp. 1043-1057, 1993.

[94] D. R. Hufner and M. L. Accorsi, "A progressive failure theory for woven polymer-based composites subjected to dynamic loading," *Composite Structures,* vol. 89, no. 2, pp. 177-185, 2009.

[95] C. Bouvet, B. Castanié, M. Bizeul, and J.-J. Barrau, "Low velocity impact modelling in laminate composite panels with discrete interface elements," *International Journal of Solids and Structures,* vol. 46, no. 14-15, pp. 2809-2821, 2009.

[96] L. Adam, C. Bouvet, B. Castanié, A. Daidié, and E. Bonhomme, "Discrete ply model of circular pull-through test of fasteners in laminates," *Composite Structures,* vol. 94, no. 10, pp. 3082-3091, 2012.

[97] V. Achard, C. Bouvet, B. Castanié, and C. Chirol, "Discrete ply modelling of open hole tensile tests," *Composite Structures,* vol. 113, pp. 369-381, 2014.

[98] M. Ridha, C. Wang, B. Chen, and T. Tay, "Modelling complex progressive failure in notched composite laminates with varying sizes and stacking sequences," *Composites Part A: Applied Science and Manufacturing,* vol. 58, pp. 16-23, 2014.

[99] S. Pinho, L. Iannucci, and P. Robinson, "Physically-based failure models and criteria for laminated fibre-reinforced composites with emphasis on fibre kinking: Part I: Development," *Composites Part A: Applied Science and Manufacturing,* vol. 37, no. 1, pp. 63-73, 2006.

[100] P. Maimí, P. P. Camanho, J. Mayugo, and C. Dávila, "A continuum damage model for composite laminates: Part I–Constitutive model," *Mechanics of Materials,* vol. 39, no. 10, pp. 897-908, 2007.

[101] P. Maimí, P. P. Camanho, J. Mayugo, and C. Dávila, "A continuum damage model for composite laminates: Part II–Computational implementation and validation," *Mechanics of Materials,* vol. 39, no. 10, pp. 909-919, 2007.

[102] T. Belytschko and T. Black, "Elastic crack growth in finite elements with minimal remeshing," *International journal for numerical methods in engineering,* vol. 45, no. 5, pp. 601-620, 1999.

[103] N. Moës, J. Dolbow, and T. Belytschko, "A finite element method for crack growth without remeshing," *International journal for numerical methods in engineering,* vol. 46, no. 1, pp. 131-150, 1999.

[104] R. Higuchi, T. Okabe, and T. Nagashima, "Numerical simulation of progressive damage and failure in composite laminates using XFEM/CZM coupled approach," *Composites Part A: Applied Science and Manufacturing,* vol. 95, pp. 197-207, 2017.

[105] B. van Dongen, A. van Oostrum, and D. Zarouchas, "A blended continuum damage and fracture mechanics method for progressive damage analysis of composite structures using XFEM," *Composite Structures,* vol. 184, pp. 512-522, 2018.

[106] S. A. Silling, "Reformulation of elasticity theory for discontinuities and long-range forces," *Journal of the Mechanics and Physics of Solids,* vol. 48, no. 1, pp. 175-209, 2000.

[107] S. A. Silling, M. Epton, O. Weckner, J. Xu, and E. Askari, "Peridynamic states and constitutive modeling," *Journal of Elasticity,* vol. 88, no. 2, pp. 151-184, 2007.

[108] T. L. Warren, S. A. Silling, A. Askari, O. Weckner, M. A. Epton, and J. Xu, "A non-ordinary state-based peridynamic method to model solid material deformation

and fracture," *International Journal of Solids and Structures,* vol. 46, no. 5, pp. 1186-1195, 2009.

[109] A. Agwai, I. Guven, and E. Madenci, "Predicting crack propagation with peridynamics: a comparative study," *International journal of fracture,* vol. 171, no. 1, p. 65, 2011.

[110] J. Xu, A. Askari, O. Weckner, and S. Silling, "Peridynamic analysis of impact damage in composite laminates," *Journal of Aerospace Engineering,* vol. 21, no. 3, pp. 187-194, 2008.

[111] C. Sun and Z. Huang, "Peridynamic simulation to impacting damage in composite laminate," *Composite Structures,* vol. 138, pp. 335-341, 2016.

[112] W. Hu, Y. D. Ha, and F. Bobaru, "Peridynamic model for dynamic fracture in unidirectional fiber-reinforced composites," *Computer Methods in Applied Mechanics and Engineering,* vol. 217, pp. 247-261, 2012.

[113] P. Roy, S. Deepu, A. Pathrikar, D. Roy, and J. Reddy, "Phase field based peridynamics damage model for delamination of composite structures," *Composite Structures,* vol. 180, pp. 972-993, 2017.

[114] B. Kilic, A. Agwai, and E. Madenci, "Peridynamic theory for progressive damage prediction in center-cracked composite laminates," *Composite Structures,* vol. 90, no. 2, pp. 141-151, 2009.

[115] E. Oterkus, A. Barut, and E. Madenci, "Damage growth prediction from loaded composite fastener holes by using peridynamic theory," in *51st AIAA/ASME/ASCE/AHS/ASC Structures*, 2010, p. 3026.

[116] E. Oterkus and E. Madenci, "Peridynamic analysis of fiber-reinforced composite materials," *Journal of Mechanics of Materials and Structures,* vol. 7, no. 1, pp. 45-84, 2012.

[117] A. Taştan, U. Yolum, M. Güler, M. Zaccariotto, and U. Galvanetto, "A 2D Peridynamic Model for Failure Analysis of Orthotropic Thin Plates Due to Bending," *Procedia Structural Integrity,* vol. 2, pp. 261-268, 2016.

[118] Y. Yu and H. Wang, "Peridynamic analytical method for progressive damage in notched composite laminates," *Composite Structures,* vol. 108, pp. 801-810, 2014.

[119] K. Colavito, A. Barut, E. Madenci, and N. Phan, "Residual strength of composite laminates with a hole by using peridynamic theory," in *54th AIAA/ASME/ASCE/AHS/ASC Structures, Structural Dynamics, and Materials Conference*, 2013, p. 1761.

[120] Y. Hu and E. Madenci, "Bond-based peridynamic modeling of composite laminates with arbitrary fiber orientation and stacking sequence," *Composite structures*, vol. 153, pp. 139-175, 2016.

[121] Y. Hu and E. Madenci, "Peridynamics for fatigue life and residual strength prediction of composite laminates," *Composite Structures*, vol. 160, pp. 169-184, 2017.

[122] Y. Bai and X.-Z. Zhang, "Progressive failure analysis of open-hole composite hoops under radial loading," *Composites Part B: Engineering*, vol. 97, pp. 336-343, 2016.

[123] H. Bao and G. Liu, "Progressive failure analysis on scaled open-hole tensile composite laminates," *Composite Structures*, vol. 150, pp. 173-180, 2016.

[124] A. Khechai, A. Tati, B. Guerira, A. Guettala, and P. Mohite, "Strength degradation and stress analysis of composite plates with circular, square and rectangular notches using digital image correlation," *Composite Structures*, vol. 185, pp. 699-715, 2018.

[125] I. Tsukrov, R. Piat, J. Novak, and E. Schnack, "Micromechanical modeling of porous carbon/carbon composites," *Mechanics of advanced materials and structures*, vol. 12, no. 1, pp. 43-54, 2005.

[126] M. S. Saadatzi, H. Ahmed, M. M. Indaleeb, and S. Banerjee, "RUSH: Realtime ultrasonic scanning using submergible hydraulic robotic arms for mechanical properties testing," in *Smart Structures and NDE for Energy Systems and Industry 4.0*, 2019, vol. 10973, p. 109730X: International Society for Optics and Photonics.

[127] J.-J. Gou, H. Zhang, Y.-J. Dai, S. Li, and W.-Q. Tao, "Numerical prediction of effective thermal conductivities of 3D four-directional braided composites," *Composite Structures*, vol. 125, pp. 499-508, 2015.

[128] Z. Hashin and B. W. Rosen, "The elastic moduli of fiber-reinforced materials," *Journal of applied mechanics*, vol. 31, no. 2, pp. 223-232, 1964.

[129] S. A. Silling and E. Askari, "A meshfree method based on the peridynamic model of solid mechanics," *Computers & structures,* vol. 83, no. 17-18, pp. 1526-1535, 2005.

[130] A. K. Singh, M.-S. Saadatzi, and C. Venkataseshaiah, "Design of Peripheral Circuits for the Implementation of Memory Array Using Data-Aware (DA) SRAM Cell in 65 nm CMOS Technology for Low Power Consumption," *Journal of Low Power Electronics,* vol. 12, no. 1, pp. 9-20, 2016.

[131] A. K. Singh, M. Saadatzi, and C. Venkataseshaiah, "Design of a single-ended energy efficient data-dependent-write-assist dynamic (DDWAD) SRAM cell for improved stability and reliability," *Analog Integrated Circuits and Signal Processing,* vol. 90, no. 2, pp. 411-426, 2017.

[132] A. K. Singh, M. Saadatzi, and C. Venkataseshaiah, "Monte–Carlo simulation for 9T SRAM cell in 45 nm CMOS," *Int. J. Adv. Res. Sci. Eng.,* vol. 4, no. 1, 2015.

[133] M. N. Saadatzi, J. Poshtan, M. S. Saadatzi, and F. Tafazzoli, "Novel system identification method and multi-objective-optimal multivariable disturbance observer for electric wheelchair," *ISA transactions,* vol. 52, no. 1, pp. 129-139, 2013.

[134] C. S. Sahler and B. D. Greenwald, "Traumatic brain injury in sports: a review," *Rehabilitation research and practice,* vol. 2012, 2012.

[135] M. Dawson, "Composite plates with a layer of fluid-filled, reticulated foam for blast protection of infrastructure," *International Journal of Impact Engineering,* vol. 36, no. 10-11, pp. 1288-1295, 2009.

[136] B. Schimizze, S. F. Son, R. Goel, A. P. Vechart, and L. Young, "An experimental and numerical study of blast induced shock wave mitigation in sandwich structures," *Applied Acoustics,* vol. 74, no. 1, pp. 1-9, 2013.

[137] G. A. Christou, L. R. Young, R. Goel, A. P. Vechart, and A. Jérusalem, "Shock attenuation of PMMA sandwich panels filled with soda-lime glass beads: A fluid-structure interaction continuum model simulation," *International Journal of Impact Engineering,* vol. 47, pp. 48-59, 2012.

[138] H. Chen, X. Li, Y. Chen, and G. Huang, "Wave propagation and absorption of sandwich beams containing interior dissipative multi-resonators," *Ultrasonics,* vol. 76, pp. 99-108, 2017.

[139] K. T. Tan, H. Huang, and C. Sun, "Blast-wave impact mitigation using negative effective mass density concept of elastic metamaterials," *International Journal of Impact Engineering,* vol. 64, pp. 20-29, 2014.

[140] E. Kim, Y. H. N. Kim, and J. Yang, "Nonlinear stress wave propagation in 3D woodpile elastic metamaterials," *International Journal of Solids and Structures,* vol. 58, pp. 128-135, 2015.

[141] E. Kim, J. Yang, H. Hwang, and C. W. Shul, "Impact and blast mitigation using locally resonant woodpile metamaterials," *International journal of impact engineering,* vol. 101, pp. 24-31, 2017.

[142] M. Li, Z. Deng, R. Liu, and H. Guo, "Crashworthiness design optimisation of metal honeycomb energy absorber used in lunar lander," *International Journal of Crashworthiness,* vol. 16, no. 4, pp. 411-419, 2011.

[143] J. Reglero, E. Solórzano, M. Rodriguez-Perez, J. de Saja, and E. Porras, "Design and testing of an energy absorber prototype based on aluminum foams," *Materials & Design,* vol. 31, no. 7, pp. 3568-3573, 2010.

[144] A. Alghamdi, "Collapsible impact energy absorbers: an overview," *Thin-walled structures,* vol. 39, no. 2, pp. 189-213, 2001.

[145] T. A. Schaedler *et al.*, "Designing metallic microlattices for energy absorber applications," *Advanced Engineering Materials,* vol. 16, no. 3, pp. 276-283, 2014.

[146] Z. Whitman and V. La Saponara, "Bistable structures for energy absorption, i: metallic structures," *Journal of Mechanics of Materials and Structures,* vol. 2, no. 2, pp. 347-358, 2007.

[147] Z. Whitman and V. La Saponara, "Bistable structures for energy absorption, II: Composite structures under tension," *Journal of Mechanics of Materials and Structures,* vol. 2, no. 2, pp. 359-375, 2007.

[148] C. Winkelmann, S. S. Kim, and V. La Saponara, "Design and development of hybrid composite bistable structures for energy absorption under quasi-static tensile loading," *Composite Structures,* vol. 93, no. 1, pp. 171-178, 2010.

[149] L. Gibson, "Woodpecker pecking: how woodpeckers avoid brain injury," *Journal of Zoology*, vol. 270, no. 3, pp. 462-465, 2006.

[150] S.-H. Yoon and S. Park, "A mechanical analysis of woodpecker drumming and its application to shock-absorbing systems," *Bioinspiration & Biomimetics*, vol. 6, no. 1, p. 016003, 2011.

[151] L. Wang, H. Zhang, and Y. Fan, "Comparative study of the mechanical properties, micro-structure, and composition of the cranial and beak bones of the great spotted woodpecker and the lark bird," *Science China Life Sciences*, vol. 54, no. 11, pp. 1036-1041, 2011.

[152] J. Oda, J. Sakamoto, and K. Sakano, "Mechanical evaluation of the skeletal structure and tissue of the woodpecker and its shock absorbing system," *JSME International Journal Series A Solid Mechanics and Material Engineering*, vol. 49, no. 3, pp. 390-396, 2006.

[153] N. San Ha, G. Lu, and X. Xiang, "Energy absorption of a bio-inspired honeycomb sandwich panel," *Journal of materials science*, vol. 54, no. 8, pp. 6286-6300, 2019.

[154] A. Bostrom, "Passbands and stopbands for an electromagnetic waveguide with a periodically varying cross section," *IEEE transactions on microwave theory and techniques*, vol. 31, no. 9, pp. 752-756, 1983.

[155] A. Boström, "Propagating, damped, and leaky surface waves on the corrugated traction-free boundary of an elastic half-space," *The Journal of the Acoustical Society of America*, vol. 85, no. 4, pp. 1549-1555, 1989.

[156] S. E. Sandström, "Stopbands in a corrugated parallel plate waveguide," *The Journal of the Acoustical Society of America*, vol. 79, no. 5, pp. 1293-1298, 1986.

[157] A. El-Bahrawy, "Stopbands and passbands for symmetric Rayleigh-Lamb modes in a plate with corrugated surfaces," *Journal of sound and vibration*, vol. 170, no. 2, pp. 145-160, 1994.

[158] A. El-Bahrawy, "Point force excitation of surface waves along the doubly corrugated traction-free boundary of an elastic half-space," *The Journal of the Acoustical Society of America*, vol. 96, no. 5, pp. 3167-3176, 1994.

[159] N. F. Declercq, J. Degrieck, R. Briers, and O. Leroy, "Diffraction of homogeneous and inhomogeneous plane waves on a doubly corrugated liquid/solid interface," *Ultrasonics,* vol. 43, no. 8, pp. 605-618, 2005.

[160] S. Banerjee and T. Kundu, "Symmetric and anti-symmetric Rayleigh–Lamb modes in sinusoidally corrugated waveguides: An analytical approach," *International Journal of Solids and Structures,* vol. 43, no. 21, pp. 6551-6567, 2006.

[161] T. Kundu, S. Banerjee, and K. V. Jata, "An experimental investigation of guided wave propagation in corrugated plates showing stop bands and pass bands," *The Journal of the Acoustical Society of America,* vol. 120, no. 3, pp. 1217-1226, 2006.

[162] S. Das, C. M. Dao, S. Banerjee, and T. Kundu, "DPSM modeling for studying interaction between bounded ultrasonic beams and corrugated plates with experimental verification," *ieee transactions on ultrasonics, ferroelectrics, and frequency control,* vol. 54, no. 9, pp. 1860-1872, 2007.

[163] M. A. Hawwa, "Shear waves in an initially stressed elastic plate with periodic corrugations," *Arabian Journal for Science and Engineering,* vol. 42, no. 5, pp. 1831-1840, 2017.

[164] M. Kushwaha and P. Halevi, "Band-gap engineering in periodic elastic composites," *Applied Physics Letters,* vol. 64, no. 9, pp. 1085-1087, 1994.

[165] Y. Huang, C. Zhang, and W. Chen, "Elastic wave band structures and defect states in a periodically corrugated piezoelectric plate," *Journal of Applied Mechanics,* vol. 81, no. 8, p. 081005, 2014.

[166] M. Collet, M. Ouisse, M. Ruzzene, and M. Ichchou, "Floquet–Bloch decomposition for the computation of dispersion of two-dimensional periodic, damped mechanical systems," *International Journal of Solids and Structures,* vol. 48, no. 20, pp. 2837-2848, 2011.

[167] M. M. Indaleeb, S. Banerjee, H. Ahmed, M. Saadatzi, and R. Ahmed, "Deaf band based engineered Dirac cone in a periodic acoustic metamaterial: A numerical and experimental study," *Physical Review B,* vol. 99, no. 2, p. 024311, 2019.

[168] T. Kundu, *Ultrasonic nondestructive evaluation: engineering and biological material characterization*. CRC press, 2003.

[169] M. Saadatzi, H. Ahmed, S. Patra, and S. Banerjee, "Utilization of Scanning Acoustic Microscope (SAM) to prove the existence of stress relaxation in woven composite," in *Smart Structures and NDE for Energy Systems and Industry 4.0*, 2019, vol. 10973, p. 109730C: International Society for Optics and Photonics.

[170] S. Patra, M. S. Saadatzi, S. Banerjee, and H. Ahmed, "Evidence of reduced order nonlinear state of Lamb wave due to stress-relaxation in composites (Conference Presentation)," in *Health Monitoring of Structural and Biological Systems XIII*, 2019, vol. 10972, p. 109721L: International Society for Optics and Photonics.

[171] S. Patra, H. Ahmed, M. Saadatzi, S. Banerjee, A. Kumar, and R. Kumar, "EFFECT OF TIME DEPENDENT STRENGTH RECOVERY OF COMPOSITE MATERIALS: QUANTIFICATION THROUGH HIGHER ORDER ULTRASONIC NON-LINEARITY USING LAMB WAVES," *Journal of Nondestructive Evaluation, Diagnostics and Prognostics of Engineering Systems*, pp. 1-10, 2019.

[172] S. Patra, H. Ahmed, M. Saadatzi, and S. Banerjee, "Experimental verification and validation of nonlocal peridynamic approach for simulating guided Lamb wave propagation and damage interaction," *Structural Health Monitoring*, p. 1475921719833754, 2019.

[173] S. Patra, H. Ahmed, M. Saadatzi, and S. Banerjee, "Evidence of dissipative and growing nonlinearity in Lamb waves due to stress-relaxation and material degradation in composites," *Ultrasonics*, vol. 96, pp. 224-231, 2019.

[174] C. A. Leckey, M. D. Rogge, and F. R. Parker, "Guided waves in anisotropic and quasi-isotropic aerospace composites: Three-dimensional simulation and experiment," *Ultrasonics*, vol. 54, no. 1, pp. 385-394, 2014.

[175] K. F. Graff, *Wave motion in elastic solids*. New York: Dover Publications Inc, 2012.

[176] M. M. Indaleeb, H. Ahmed, M. Saadatzi, and S. Banerjee, "Dirac-like cone modulation for phononic crystals using deaf band," in *Health Monitoring of Structural and Biological Systems XIII*, 2019, vol. 10972, p. 109721Z: International Society for Optics and Photonics.

[177] H. Ahmed, M. M. Indaleeb, M. Saadatzi, T. Sain, S. Ghosh, and S. Banerjee, "Investigation of wave trapping and attenuation phenomenon for a high symmetry interlocking micro-structure composite metamaterial," in *Smart Structures and NDE for Energy Systems and Industry 4.0*, 2019, vol. 10973, p. 109730W: International Society for Optics and Photonics.

[178] P. A. Deymier, *Acoustic metamaterials and phononic crystals*. Springer Science & Business Media, 2013.